# Condition monitoring of train wheels using a const-effective smart rail pad

## Marcho Heinrich van Schalkwyk

**A dissertation submitted in partial fulfilment of the requirements for the degree of**

**MASTER OF ENGINEERING (TRANSPORTATION ENGINEERING)**

**In the**

**FACULTY OF ENGINEERING, BUILT ENVIRONMENT AND INFORMATION TECHNOLOGY**

**UNIVERSITY OF PRETORIA**

**January 2022**

# SUMMARY

## Condition Monitoring of Train Wheels Using a Cost-Effective Smart Rail Pad

_____

## Marco Heinrich van Schalkwyk

| | |
|---|---|
| Supervisor: | Grabe, Petrus Johannes |
| Department: | Civil Engineering |
| University: | University of Pretoria |
| Degree: | Master of Engineering (Transportation Engineering) |

Sensing instrumentation plays an important role in measuring both the performance and the condition of the railway track. Data on how the various components of a railway track respond to a passing train in terms of acceleration, displacement, and loading are necessary for condition monitoring of the railway track. Measuring these parameters from within a rail pad can enable a new condition monitoring system for wheel defects and provide information about the wheel load distribution on the track structure.

In this study, a smart rail pad was fabricated utilising 3D printing technology and instrumented with low-cost sensing instrumentation. Initial material testing was conducted to determine the best suited 3D printing material, considering Polylactic Acid (PLA), Polyethylene Terephthalate modified with Glycol (PETG) and Thermoplastic Polyurethane (TPU), to protect the instrumentation and to withstand the typical forces of a real rail pad. The material testing results showed that the best suited material was PETG, and it was subsequently used for the final design. Various laboratory tests were done using a hydraulic actuator on two different prototypes to determine the response within a 3D printed rail pad. Similar laboratory tests were done on the final designed smart rail pad before it was tested in the field on a railway line to determine its performance in operational conditions.

The developed smart pad system was able to automatically detect an oncoming train and turn the Razor microcontroller on to start logging the data from the smart rail pad. The smart rail pad was able to identify more than 60 % of the wheel defects on average. This was not as accurate as expected because of the major limiting factor being the low sampling rate of the system when all three instruments are logging data. The strain gauge could also be used to detect wheel

defects as do the accelerometers. The smart rail pad showed excellent signal response to the variations in the loading magnitude of the tested trains. The measured wheel loads were in good agreement with the control wheel load measurements. The smart rail pad can therefore be used for wheel load sensing measurements and act as an axle counter.

# ACKNOWLEDGEMENTS

I wish to express my appreciation to the following persons who made this dissertation possible:

a) The University of Pretoria for the use of facilities and equipment during the study.

b) My supervisor, Professor PJ (Hannes) Gräbe, for his guidance and support throughout the study. His extensive knowledge of Railway Engineering and him always willing to lend a hand helped me conquer any hurdle during the study.

c) The following persons are gratefully acknowledged for their assistance and advice during the study:

   i) Mr J. Scholtz (University of Pretoria – Civil Engineering Staff)

   ii) Mr A. Broekman (University of Pretoria – Railway Engineering)

   iii) Mr C. Hawley (University of Pretoria – Railway Engineering)

d) Ms N. Ludik for proof reading of the dissertation.

e) My friends and family for their encouragement and support during the study.

# DECLARATION

I, the undersigned hereby declare that:

- I understand what plagiarism is and I am aware of the University's policy in this regard;
- The work contained in this thesis is my own original work;
- I did not refer to work of current or previous students, lecture notes, handbooks or any other study material without proper referencing;
- Where other people's work has been used this has been properly acknowledged and referenced;
- I have not allowed anyone to copy any part of my thesis;
- I have not previously in its entirety or in part submitted this thesis at any university for a degree.

DISCLAIMER:

The work presented in this report is that of the student alone. Students were encouraged to take ownership of their projects and to develop and execute their experiments with limited guidance and assistance. The content of the research does not necessarily represent the views of the supervisor or any staff member of the University of Pretoria, Department of Civil Engineering. The supervisor did not read or edit the final report and is not responsible for any technical inaccuracies, statements or errors. The conclusions and recommendations given in the report are also not necessarily that of the supervisor, sponsors or companies involved in the research.

**Signature of student:**   _Schalkwyk_

**Name of student:**   **MH van Schalkwyk_____**

**Student number:**   **16018975_____**

**Date:**   **11 February 2022_____**

**Number of words in report:**   **20282_____**words

# TABLE OF CONTENTS

APPENDIX A  NOTES ON APPENDICES

APPENDIX B  EVALUATION FORMS

# LIST OF TABLES

# LIST OF FIGURES

# LIST OF ABBREVIATIONS

| | |
|---|---|
| ABS | Acrylonitrile Butadiene Styrene |
| ADC | Analog-to-Digital Converter |
| ASTM | American Society for Testing and Materials |
| BOEF | Beam on elastic foundation |
| DIF | Dynamic Impact Factor |
| DLP | Digital Light Projection |
| DoF | Degree of Freedom |
| EPDM | Ethylene Propylene Diene Monomer |
| EVA | Ethylene-Vinyl Acetate |
| FBG | Fibre Bragg Grating |
| FDM | Fused Deposition Modelling |
| FFF | Fused Filament Fabrication |
| FFT | Fast Fourier Transform |
| FORPS | Fibre Optic Rail Pad Sensor |
| HDPE | High Density Polyethylene |
| $I^2C$ | Inter-Integrated Circuit |
| IDE | Integrated Development Environment |
| IMU | Inertial Measurement Unit |
| LVDT | Linear Variable Differential Transducer |
| MEAM | Material Extrusion Additive Manufacturing |
| MEMS | Micro-Electro-Mechanical System |
| MTS | Materials Testing System |
| PETG | Polyethylene Terephthalate modified with Glycol |
| PLA | Polylactic Acid |
| PVDF | Polyvinylidene Fluoride |
| RASP | Rail-strain-pad |
| SBR | Styrene-Butadiene |
| SLA | Stereolithography |
| SHM | Structural Health Monitoring |
| SRAM | Static Random-Access Memory |
| STL | Surface Tessellation Language |
| TPE | Thermoplastic Elastomer |
| TPU | Thermoplastic Polyurethane |
| UCL | Upper confidence limit |
| UV | Ultraviolet |

# LIST OF SYMBOLS

| | |
|---|---|
| s | Standard deviation (Eisenmann) |
| $\bar{x}$ | Mean Rail Stress (Eisenmann) |
| $\delta$ | Track Condition (Eisenmann) |
| $\eta$ | Vehicle Speed Factor (Eisenmann) |
| $V$ | Vehicle Speed (km/h) |
| $X$ | Maximum Rail Stress |
| $\varphi$ | Dynamic Impact Factor |
| g | Gravitational Force Equivalent or G-force |
| Hz | Hertz (1/seconds) |
| Pa | Pascals |
| °C | Celsius |
| R | Electrical Resistance |
| $\varepsilon$ | Strain/Axial Strain |
| $v$ | Poisson's Ratio |
| $Q$ | Resistivity |
| $V_o$ | Bridge Output Voltage |
| $V_s$ | Supply Voltage |
| k | k-factor of strain gauge |
| $\Delta n$ | Refractive Index (FBG) |
| $\lambda_B$ | Bragg Wavelength (FBG) |
| $n_{eff}$ | Effective Refractive Index (FBG) |
| $\Lambda$ | Grating Period (FBG) |
| N | Newton (FBG) |
| $P_{static}$ | Static Wheel Load |
| $P_{dyn}$ | Dynamic Wheel Load |
| $q_r$ | Maximum Rail Seat Load |
| $f$ | Frequency (Hz) |
| $\lambda$ | Wavelength (Frequency) |
| v | Vehicle Speed (m/s) |
| $k_{dynamic/static}$ | Dynamic Stiffness/Static Stiffness |
| $F_{max/min}$ | Average maximum and minimum applied force |
| $D_{max/min}$ | Average maximum and minimum measured deflection |
| $F_{initial/final}$ | Initial and final applied force in the static test |
| $D_{initial/final}$ | Initial and final measured deflection associated with the applied force |

# 1 INTRODUCTION

## 1.1 BACKGROUND

The ballasted track is the most common track structure used worldwide due to its proven technology and ease of maintenance. With the introduction of concrete sleepers, the track structure became stiffer compared to track structures with timber sleepers. To combat the stiffer structure, elastic rail pads are placed between the rail seat and the sleeper. The function of the rail pad is to provide resiliency for the track structure and damping of wheel-induced vibrations and noise (Esveld, 2001).

The vertical stiffness of the rail pad is important for track performance and durability. Rail pads are made of various rubber and plastic materials to create rail pads with different characteristics and mechanical behaviour. The most used materials for rail pads are HDPE (High-density Polyethylene), EVA (Ethylene-Vinyl Acetate), TPE (Thermopolymer Polyester Elastomer) and EPDM (Ethylene Propylene Diene Monomer). The various 3D printing plastics range from flexible to hard and brittle plastics. With the onset of 3D printing technology, a new and interesting method of creating rail pads can be introduced.

Sensing instrumentation plays an important role in measuring both the performance and the condition of the railway track. Data on how the various components of a railway track respond to a passing train in terms of acceleration, vibration, displacement and loading are necessary for condition monitoring of the railway track. Various trackside monitoring instrumentation has been shown to provide these measurements, however, they are primarily research equipment that are costly and practical deployments are narrow in scope (Milne et al., 2016). To thoroughly evaluate the structural condition of the railway track, new cost-effective approaches to condition monitoring are required.

Smart rail pads are a new concept that has only been researched and developed to a limited extent. Measurements from inside the rail pad can be obtained by the installation of instruments such as accelerometers, piezoelectric sensors, force sensors and fibre optics. Operational aspects such as accelerations, vibrations, axle load, frequency and temperature can be measured using sensing instrumentation installed inside a rail pad. These measurements could enable condition monitoring of the track structure.

Fabricating a rail pad from 3D printing filament is unexplored and can provide an exciting avenue for new possibilities. Creating a rail pad from 3D printing material can simplify the process of embedding instrumentation inside a rail pad to protect said instrumentation.

Accelerometers inside the rail pad can provide monitoring of wheel defects when wheel flats (high impact forces) occur. The magnitude and type of forces exerted onto a rail pad can also be measured. Load sensing capabilities using strain gauges can provide the wheel load at the rail seat area which provides insight into the wheel load distribution from the rail to the sleepers. To measure these parameters, the fabrication of a low-cost remote monitoring system that automatically detects an oncoming train and captures data from instrumentation inside a smart rail pad is investigated.

## 1.2    OBJECTIVES OF THE STUDY

The objective of this study is to investigate the effectiveness of smart sensing technology, fitted inside a 3D printed rail pad, to monitor the condition of train wheels. The following sub-objectives were required to design and test the smart rail pad:

- To investigate the effectiveness of 3D printing technology for generating a rail pad.

- To develop a smart rail pad using sensing technology, embedded inside in a 3D printed rail pad, for creating a condition monitoring system.

- Quantifying the dynamic response of a smart rail pad using, embedded sensing technology, in both laboratory and field environments

## 1.3    SCOPE OF THE STUDY

The scope of the study entails investigating the effects of a moving train on a rail pad employing smart sensing instrumentation and determining what transpires with the loading from the rail through the rail pad to the sleeper. The smart rail pads were fabricated using various 3D printed filament including PLA, PETG and TPU. The instrumentation was fitted during the fabrication process by stopping the printing process and installing the instrumentation. The instrumentation included MEMS accelerometers and strain gauges. Testing of the instrumented rail pad was done in the laboratory using a hydraulic actuator. The experiment focused on wheel flat/defect identification and the loading exerted onto the rail pad. Additional field tests were conducted on an existing railway track after successful laboratory testing. This was done to measure the response of the rail pad in field conditions and to determine any wheel defects.

## 1.4    METHODOLOGY

The methodology was as follows:

- A literature review was conducted on various sensors and instrumentation that can be installed into the rail pad, 3D printing and condition monitoring;

- The materials and components needed for the testing were obtained from suppliers and the rail pad was fabricated using different filaments;
- MEMS accelerometers and strain gauges were fitted inside the 3D printed rail pad;
- Testing was conducted using a rail-sleeper system with the instrumented rail pad and an MTS machine, through the application of cyclic loading. Field tests was conducted for comparison with the laboratory results and in-practice applications;
- Various aspects such as strain, acceleration, displacement and loading amongst others, was measured with the instrumented rail pad and compared with control measurements; and
- The data was analysed, results will be discussed, and conclusions were drawn.

## 1.5    ORGANISATION OF THE DISSERTATION

The report consists of the following chapters:

- Chapter 1 serves as an introduction to the dissertation, outlining the objectives, problem statement, scope, methodology and organisation of the dissertation.

- Chapter 2 contains the literature study which will serve as a technical introduction and review of past research conducted as guidance for the thesis.

- Chapter 3 describes the test materials, equipment used in the experiment and the laboratory and field-testing procedure.

- Chapter 4 presents and discuss the results obtained during the study.

- Chapter 5 includes the conclusions that were drawn from the study and provide recommendations for future studies.

# 2 LITERATURE REVIEW

This chapter provides an overview of the railway track structure and track loading with a focus on rail pads. A discussion on the background of 3D printing technology and the application thereof, for the fabrication of a rail pad, is given. Thereafter a comprehensive discussion on the literature of smart sensing instrumentation utilising MEMS technology, strain gauges and fibre optics is provided. A review of previous literature is discussed, focusing on the implementation of sensing instrumentation in track components, especially in rail pads. This chapter concludes with a discussion of the combination of 3D printing technology and sensing instrumentation for the fabrication of a smart rail pad.

## 2.1 RAILWAY TRACK STRUCTURE

The ballasted track is the most common track structure used worldwide. This is due to its proven technology and ease of maintenance. The track structure is divided into two sections: the superstructure and the substructure. The superstructure comprises the main load-supporting components of the track structure which transfers the load to the supporting substructure. The load-supporting components include the rail, sleeper, elastic rail pad and fastening system. The superstructure supports the train loading. This is achieved by reducing the extremely high forces at the wheel-rail interface to a level that will be tolerable for the substructure. This is necessary so that the superstructure can resist the lateral, vertical and longitudinal forces with minimum elastic and permanent deformation (Li et al., 2015). The substructure consists of the formation layers that support the superstructure. These formation layers comprise the ballast, subballast and subgrade. The two structures are separated by the sleeper-ballast interface (Selig & Waters, 1994).

As stated by Li et al. (2015), the rails are longitudinal high-strength steel members which are the most visible component of the superstructure and directly support passing trains. The purpose of the rails is to guide the train wheels uniformly and to serve as beams that transfer wheel forces to the underlying sleepers without excessive deformation.

The rails rest on the sleepers with the assistance of an elastic rail pad. Concrete sleepers have the advantage that climatic variables have little effect on their durability. Concrete sleepers have an expected service life that is significantly higher than timber sleepers, however, only under specific conditions (Selig & Waters, 1994).

The general functions of sleepers are to (Esveld, 2001):

- Serve as the support and fixing component for the fastening system and rail foot;
- Support rail forces and uniformly transfer it to the ballast;
- Preserve the correct track gauge;
- Provide electrical insulation between the two rails; and
- Be resistant to mechanical and weathering influences.

The fastening system which includes the fasteners and the rail pad maintains the rail against the sleepers and withstands the lateral, longitudinal, vertical and overturning moments of the rail (Selig & Waters, 1994). Figure 2.1 illustrates the components of a typical ballasted track structure.
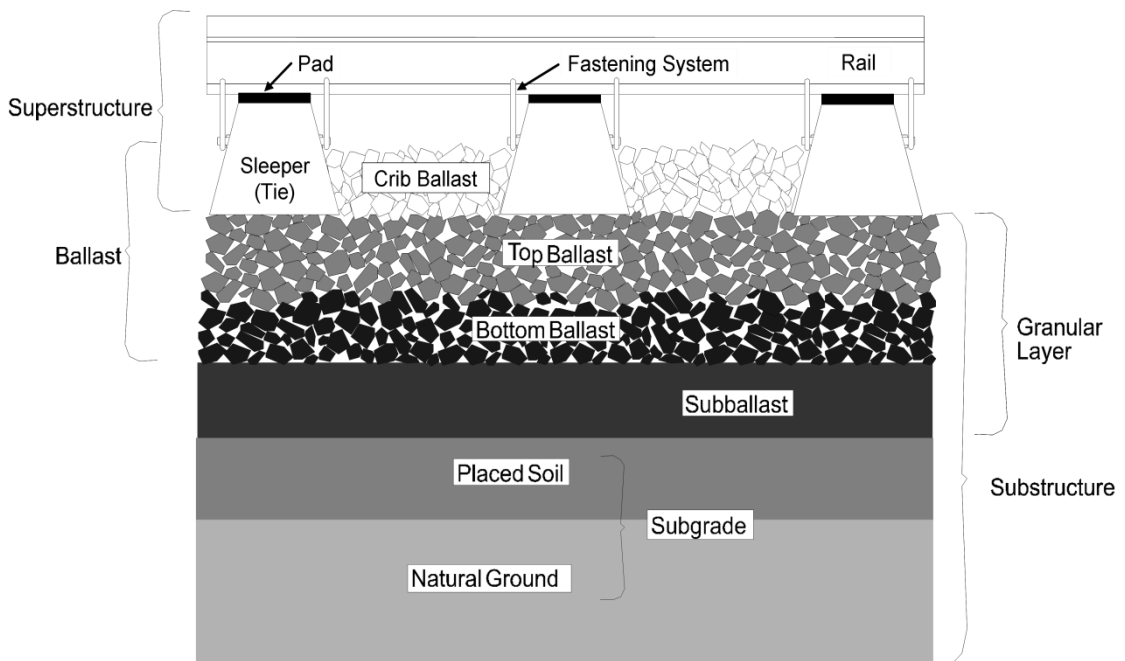


**Figure 2.1: Typical ballasted track structure (adapted from Selig & Waters, 1994)**

Ballast is the granular top layer of the substructure in which the sleepers are placed. Good ballast is classified as angular, hard, and uniformly graded rock. The most important ballast functions are the following (Selig & Waters, 1994):

- Resist the vertical, lateral and longitudinal forces applied to the sleepers to retain the required track geometry;
- Provide some resiliency to the track;
- Provide large voids for fouling material storage;

⊥ Provide immediate drainage of any water on the track; and

⊥ Facilitate maintenance actions by allowing rearranging of the ballast with tamping.

Subballast is the layer between the ballast and subgrade. It has the following functions that are important for satisfactory track performance (Selig & Waters, 1994; Li et al., 2015):

⊥ Reduce traffic-induced stresses from the ballast to an acceptable level for the subgrade;

⊥ Prevent interpenetration of the subgrade and ballast;

⊥ Prevent upward movement of fine material from the subgrade as well as upward flowing water from the subgrade; and

⊥ Intercepting water from the ballast and leading it away from the subgrade.

Selig & Waters (1994) stated that the subgrade is the stable foundation upon which the track structure is positioned. The main function is to provide a stable platform for the subballast and ballast layers. The traffic-induced stresses can extend up to five metres into the formation which influences the subgrade. The subgrade should be designed to allow surface water and ground water to drain away from the track (Li et al., 2015). Therefore, the subgrade is an important substructure layer for track performance and maintenance.

## 2.2 RAILWAY TRACK LOADING

### 2.2.1 Dynamic loading

Li et al. (2015) stated that the forces at the wheel-rail interface may be divided into three components: the *static* component, which is the weight of the train, the *dynamic* component, which is due to movement of the train, and the *cyclic* component, which is the number of load applications. The dynamic component would be negligible if both the wheel and rail surfaces were perfectly smooth. However, there exist imperfections in both the wheel and rail running surfaces. The magnitude of the dynamic component is influenced by the size and shape of these imperfections, the condition of the vehicle and the track, as well as the speed of the train. The train speed affects the dynamic component in three ways:

⊥ The magnitude of the force increases with the train speed;

⊥ Particular speeds rouse resonances of the track or train at imperfections of a particular size and shape; and

⊥ Large impact forces are generated when the wheel regains contact after losing contact with the rail at an imperfection.

The dynamic load component can occur in the form of short or long-duration forces. The short duration forces are high-frequency impact loads associated with wheel defects (e.g., wheel flats)

2-4

or rail irregularities (such as dipped joints and rail corrugations). Long duration forces occur as a result of track geometry unevenness, probably due to stiffness variations in the track structure (Jideani, 2018). The dynamic load component is generally estimated by multiplying the static wheel load with a dynamic impact factor (DIF) (Esveld, 2001).

The dynamic wheel load can be calculated with various empirical formulae. Transnet Freight Rail, in South Africa, incorporates the statistical approach of Eisenmann to determine the dynamic impact factor. Eisenmann (1972) proposed that the rail bending stress and rail deflection are normally distributed and that the mean value can be calculated from the Beam-on-elastic-foundation (BOEF) model. The normal distribution for both rail stress and deflection are displayed in Figure 2.2.
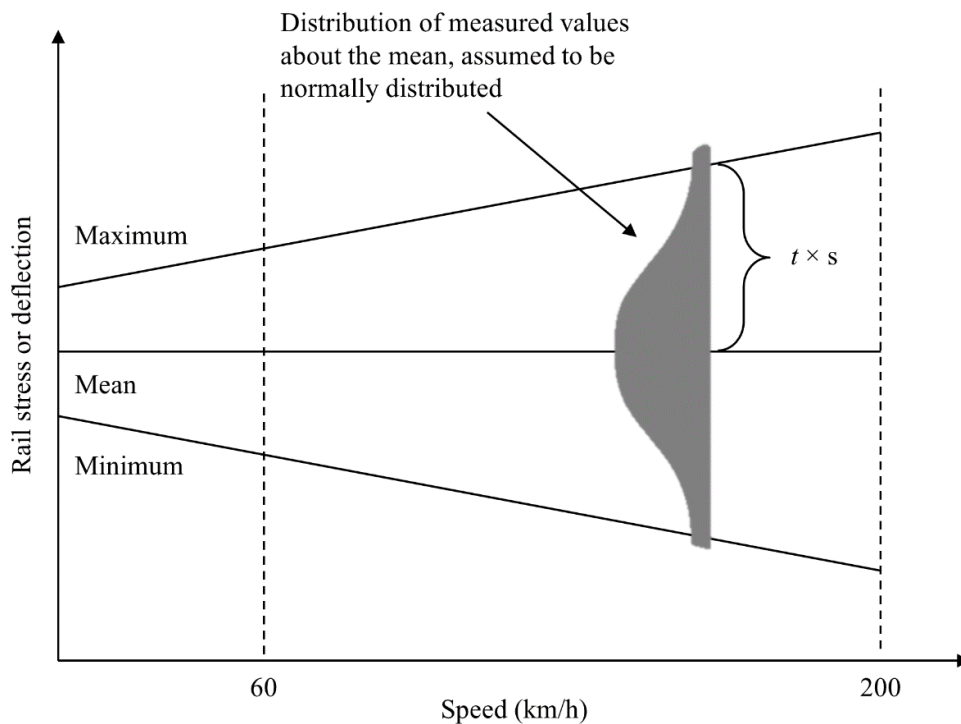


**Figure 2.2: Statistical distribution of measured rail stress or deflection values with speed effect (adapted from Eisenmann, 1972)**

The mean rail stress ($\bar{x}$) and the corresponding standard deviation ($s$) can be expressed by:

$$s = \bar{x}\, \delta\, \eta \qquad \text{(Equation 2.1)}$$

where $\delta$ = track condition factor and $\eta$ = vehicle speed factor.

The value of $\delta$ is defined by the quality of the track and the following values are suggested: 0.1, 0.2 and 0.3 for track in very good, good, and poor condition, respectively. The value of $\eta$ is determined from the vehicle speed, $V$ (km/h), with a proposed value of $\eta = 1$ for speeds below 60 km/h. For vehicle speeds between 60 – 200 km/h, the following formula is used:

$$\eta = 1 + \frac{V - 60}{140} \qquad \text{(Equation 2.2)}$$

The product of $\delta \cdot \eta$ is referred to as the coefficient of variation. The corresponding maximum rail stress (or rail deflection) is given by:

$$X = \bar{x} + s\,t \qquad \text{(Equation 2.3)}$$

where $t$ = chosen upper confidence limits (UCL) defining the probability that the maximum rail stress (or rail deflection) will not be exceeded. The maximum rail stress ($X$) can be defined by the following relationship:

$$X = \varphi\,\bar{x} \qquad \text{(Equation 2.4)}$$

where $\varphi$ = dynamic impact factor. Combining Equations 2.1 and 2.3 and equating it to Equation 2.4, the expression for the dynamic impact factor is:

$$\varphi = 1 + \delta\,\eta\,t \qquad \text{(Equation 2.5)}$$

where values of $t$ can be chosen from the following:

$t = 0$, UCL = 50 %;

$t = 1$, UCL = 84.1 %;

$t = 2$, UCL = 97.7 %; and

$t = 3$, UCL = 99.9 %.

### 2.2.2 Wheel Flats

The large forces, generated from wheel and rail defects, cause major degradation and failure in both the train vehicles and the track structure. The most apparent wheel defect is wheel flats. Wheel flats are caused by the following two circumstances: (1) the wheels of a train vehicle being locked while braking and sliding along the rail and (2) the reduction of wheel-rail adhesion that causes the wheel to slide on the rail (Newton & Clark, 1979; Zhou et al., 2020b). The friction creates a flat spot on the wheel, which in turn, generates high impact forces and stresses in the track every time the irregularity hits the rail (Newton & Clark, 1979). Kumagai et al. (1991) classified wheel flats into three modes – a single flat, spot flat and continuous flat.

A single oval-shaped flat is an area of abrasion caused by the locking of the axle which often occurs in trailer axles. A spot flat is a collection of little single flats. A continuous flat, which is thin and elongated, is caused by wheel skids on the rail without the wheel locking. This flat commonly occurs with locomotive axles. Wheel flats generate noise and vibrations and bring discomfort to passengers and can cause derailments in extreme cases (Filograno et al., 2013). Train wheels must be reprofiled regularly as part of the normal maintenance schedule. However, excessive reprofiling does occur. The latter causes an increase in maintenance cost and shortens the service life of the wheels since all the wheels are grinded in the process. The damage that wheel flats create has become more noticeable with the increase in speed and axle loading on railway lines. Therefore, it is of great interest to monitor the origin and growth of wheel defects to improve the safety and reliability of railway operations (Zhou et al., 2020). With the implementation of the right condition monitoring system, early detection of track and rolling stock irregularities can improve the overall safety of railways.

### 2.2.3 Wheel load distribution

Russel et al. (2020) found that, when considering a wheel load over five sleepers, an average of 45 % of the wheel load is carried by the sleeper directly below the wheel load. Approximately 22.5 % of the wheel load is carried by the adjacent sleepers and 5 % by each of the outlying sleepers. These wheel load distributions are displayed in Figure 2.3.
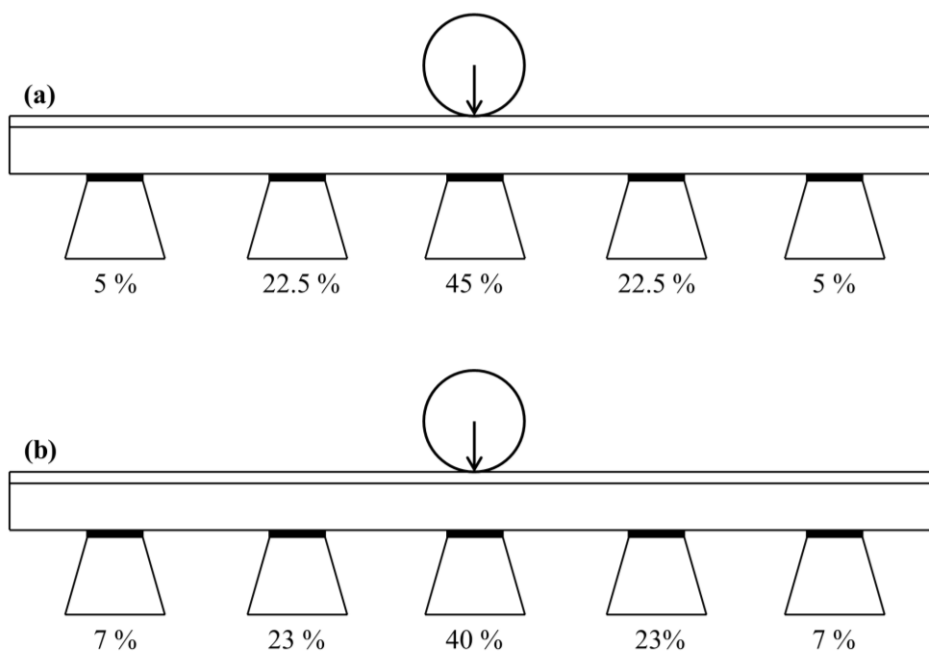


**Figure 2.3: Wheel load distribution: (a) Russel et al. (2020) and (b) Profillidis (2000)**

Profillidis (2000) performed a finite-element analysis showing load distribution to be 40 % of the total load to the sleeper below the wheel, 23 % to the adjacent sleepers and 7 % to the outer sleepers. The percentage of the load distributed to the sleepers depends on the sleeper spacing as well as the magnitude of the load. When the sleeper spacing is greater, the centre sleeper carries more of the vertical load because the two adjacent sleepers are further apart.

### 2.2.4 Wheel condition monitoring

The first aspect of any maintenance action is the knowledge of the current condition of assets. The knowledge of the current condition of rail infrastructure can reduce maintenance costs by reducing the time needed for maintenance actions and allowing for predictive maintenance. Condition monitoring of the train wheels can contribute towards predictive maintenance which will reduce wheel-rail impact forces and the wear on both the rail and the wheel. Esveld (2001) appropriately stated that condition monitoring is of great importance for maintenance actions and the reliability and safety of railway traffic.

Bi et al. (2019) noted the various wayside methods used to measure high-frequency wheel-rail impact forces. The current methods include the shear stress, acceleration and deflection methods. Ohtani (1995) and Alemi et al. (2017) stated that the use of accelerometers over strain gauge-based monitoring has the advantage that the magnitude of the response depends, to a certain extent, on the wheel-rail interface forces that are linked to the unsprung mass. Hence, the acceleration response is independent of the train speed and mass within the operational condition. While high-frequency responses can be measured by an accelerometer under the acceleration method, any change in rail support status will change the inherent characteristics of the rail vibration modes, resulting in a challenging mode calibration and making it difficult to accurately correlate the test results with the actual impact force.

A continuous condition monitoring system that measures at regular intervals can provide insight into the behaviour of the track structure over time (Esveld, 2001). With this knowledge, condition forecasting and maintenance planning can occur, reducing the overall maintenance costs required.

## 2.3 RAIL PADS

### 2.3.1 Background

With the introduction of concrete sleepers, the track structure became stiffer compared to track structures made with timber sleepers. To combat the stiffer structure, rail pads are placed

between the rail seat and the sleeper to provide a compatible surface. Rhodes et al. (1989) reported that the first rail pads were made of synthetic rubbers such as Styrene-Butadiene (SBR) and Neoprene. These rail pads were not very durable or resilient and had to be replaced frequently. With the introduction of plastic materials in the 1970s, such as High-Density Polyethylene (HDPE), pads have a much longer service life and durability than rubber pads (Rhodes et al., 1989). Today, rail pads are made of various rubbers and plastics to create pads with different characteristics and mechanical behaviour. The material properties of these rail pads can be controlled to be more resistant to cold temperatures by adding polyvinyl acetate to HDPE to form Ethylene-Vinyl Acetate (EVA). The most used materials for rail pads are HDPE, EVA, TPE (Thermopolymer Polyester Elastomer) and EPDM (Ethylene Propylene Diene Monomer). Figure 2.4 illustrates the different rail pads that are available.



**Figure 2.4: Different designs and types of rail pads: HDPE pad (left), Hytrel studded pad (middle) and a common EVA pad (right)**

Rhodes et al. (1989) and Selig & Waters (1994) stated that the predominant function of the rail pad is to transfer the rail load to the sleeper while providing resiliency for the track structure as well as reducing wheel vibrations and noise. The rail pad protects the concrete surface from being worn away by the rail seat. Longer service life is easier to achieve with a non-resilient pad than with a resilient pad, but the more resilient pad may extend the sleeper service life (Rhodes et al., 1989). The rail pad is of more significance in ballastless track structures, such as slab track or bridge structures, to provide resiliency and damping.

Rhodes et al. (1989) suggested that apart from the resiliency of the rail pad, the durability of the pad should also be considered. High abrasion resistance is typically related to high hardness and stiffness. High abrasion resistance is a conflicting requirement when the resiliency of the rail pad is considered. A studded or grooved surface allows a pad with lower inherent abrasion

resistance to provide a longer service life. This is due to the pad being resilient in the shearing and vertical aspect and to reduce the possibility of slip between the pad and sleeper surface, or rail and pad.

Rail pads are extremely important for the resiliency of the track structure and to absorb the high impact forces from the moving train on the rail. Without the rail pad to provide resiliency, especially with concrete sleepers, the ballast and underlying formation layers experience high impact forces that create ballast breakdown under and around the sleeper. Figure 2.5 displays the consequence of a missing pad on the ballast. From Figure 2.5, it can be seen how the high-impact force breaks down the ballast. The damaged ballast has rounded edges and a smooth surface which is not the properties that ballast should have. The high impact moved the sleeper, on the left-hand side, over to the right. The irregular sleeper spacing, missing rail pad and ballast breakdown produces an increase in vibrations and therefore, track deterioration. Ballast breakdown can create fouling material that decreases the drainage and performance of the ballast and substructure below.



**Figure 2.5: Ballast breakdown due to missing rail pad**

### 2.3.2 Vertical stiffness of a rail pad

The vertical track stiffness, in ballasted track, is dependent on the stiffness of the rail pads, and, to a lesser extent, on the stiffness of the ballast layer (Sañudo et al., 2017; Sainz-Aja et al.,

2020). With the current gravitation towards slab track design, mainly for high-speed lines, the rail pad exclusively produces adequate stiffness for the track (Chen & Zhou, 2020).

Sainz-Aja et al. (2020) conducted a study to investigate the influence of the operational conditions on the static and dynamic stiffness of rail pads. The loading magnitude and frequency (i.e., rate of loading) of the rail pads are dependent on train speed and axle load when operated under service conditions. The compressive force exerted onto the rail pad is a combination of the weight of the train and the toe load. The toe load is the compressive force that the fastening system applies to hold the rail in position with its standard value of 18 kN. It was noted that the vertical stiffness of a rail pad is greatly affected by temperature. The authors concluded that the increase in axle load, toe load and frequency, increased the static and dynamic stiffness of a rail pad. The vertical stiffness of the rail pad is important for track performance, durability and maintenance.

Woschitz (2011) stated that the fast deterioration rate in rail pads is due to the horizontal and vertical forces exerted from the rail as well as the temperature changes experienced. Better material performance is needed to achieve a longer service life. A smart rail pad can provide information about the track structure below and above the rail pad itself. Rail irregularities and poor track foundation can cause high frequencies, high accelerations and high deflections that can be measured by a smart rail pad. Thompson (2009) stated that the stiffness of a rail pad can affect the damping of the rail and the connection between the sleepers and the rail, as illustrated in Figure 2.6.
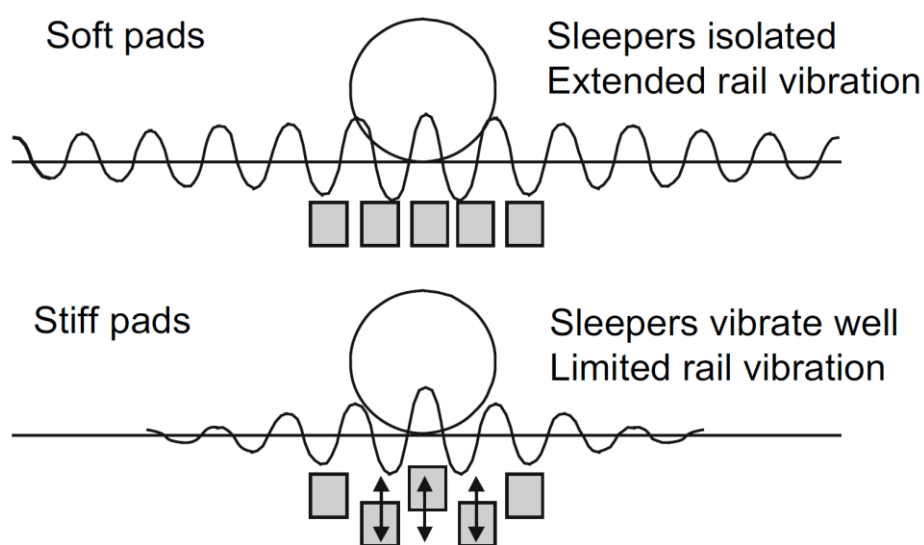


**Figure 2.6: Effect of rail pad stiffness on the damping of waves in the rail and the connection between the sleeper and the rail (Thompson, 2009)**

Soft rail pads maintain the sleepers to be fully isolated from the rail vibration, however, the vibration can travel freely along the rail. In comparison, the rail vibration, for stiff rail pads, is limited to the connection to the sleepers and damping of the pad, however, the sleeper vibration is greater

## 2.4 ADDITIVE MANUFACTURING

This section discusses the background, properties and uses of additive manufacturing or 3D printing and the possibility of fabricating a rail pad from 3D printing material for creating a smart rail pad.

### 2.4.1 Background

Horvath (2014) presents a comprehensive overview of the origin and history of 3D printing. The first 3D printers were stereolithography (SLA) systems which many large commercial printers still use today. SLA utilises ultraviolet (UV) light to coagulate a resin or liquid with the use of a laser, or at times digital light projection (DLP) imager, to harden the liquid one layer at a time. Fused Deposition Modelling (FDM) or Fused Filament Fabrication (FFF) was patented by Steven and Lisa Crump in 1989. The basis of this technology is that the printer provides plastic through a heated extruder, which then precisely places the plastic layer by layer (Horvath, 2014). As the extruded layer of plastic is placed one upon another, the layers merge together, when cooled, to form a solid plastic element (Evans, 2012). The rate of development of 3D printing is very rapid with the most noticeable being the significant reduction in cost and availability of 3D printers.

Most personal 3D printers have many similarities although there are some different approaches. Essential for a 3D printer is movement in the Cartesian coordinates (x-, y- and z-axes) using a stepper motor to translate millimetres precisely and accurately in any direction (Evans, 2012). 3D printers typically use timing belts and pulleys to position along the x- and y-axes while using a threaded rod to position in the z-axis (Evans, 2012).

The extruder combines two important elements: the filament drive and the thermal hot end (Evans, 2012). The filament drive gathers the plastic from the spool using a drive mechanism. The filament is fed into the stainless-steel tube called the heat break which is situated in the heat sink. The purpose of the heat sink is to cool down the heat break with aid of a cooling fan. When the plastic filament reaches the hot end, it is heated to 170 °C – 220 °C, depending on the given plastic. The plastic is forced, in its semi-liquid state, through the nozzle of the hot end – with an opening of 0.35 mm - 0.5 mm – before laying down the thin extruded plastic onto the heated

print bed. The purpose of the heated print bed is to prevent cracking or warping of the print as well as to create greater adhesion between the layers as it cools down. Figure 2.7 illustrates the various components of a typical Cartesian 3D printer.
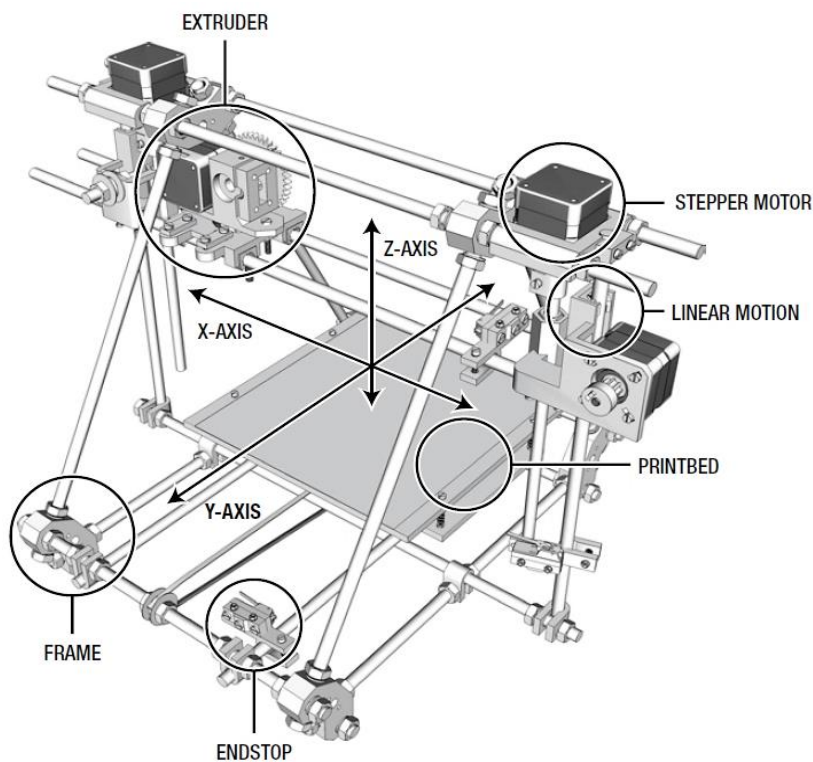


**Figure 2.7: 3D printer anatomy (Hodgson & Průša, 2011)**

### 2.4.2   Fused Deposition Modelling (FDM) process

The important first step in the printing process is finding or creating a 3D model. 3D models can be designed in various programs such as Adobe Fusion360, AutoCAD, or TinkerCAD. 3D scanners can scan any object for 3D printing, eliminating the design process. Once the model is designed or scanned, it must be exported as an STL file. STL stands for STereoLithography or Surface Tessellation Language. After the STL file is created the next step is to slice the file into layers that the printer can understand and execute. The slicing program considers the physical dimensions of the printer as well as the geometry of the model being printed. In the slicing program, the user must configure various settings to create the best print possible. The various settings include the temperature of the extruder nozzle and print bed, print speed, infill percentage and pattern, amongst others. The filament is the reason for the choice of the temperature of the nozzle and print bed as well as print speed. A printer places down filament

at a particular flow rate which is controlled by how fast the extruder is moving while printing (Horvath, 2014). Slicing programs such as CURA or Slic3r allow the users to set various print speeds depending on the printing parameters, infill percentage and patterns. Once the input settings are done, the slicing program creates a G-code file (commands that drive the printer movement). The software on the printer interprets the G-code, one command at a time, and sends it to the printer to execute (Horvath, 2014).

Creating solid objects is not feasible because it uses a lot of filament, however, the objects cannot be hollow either. The slicing program automatically creates internal support called infill. The purpose of infill is to control shrinkage and to minimise filament use resulting in faster printing. The infill pattern is thin enough to stretch axially as it shrinks radially therefore it does not pull the perimeters inward as it cools and harden. Infill can have various patterns to create numerous types of internal support. Infill is typically quantified as a percentage fill. An infill percentage of 20 % means that 20 % of the interior volume is filled while 80% is left open. The pattern of the infill is also specified, and this is illustrated in Figure 2.8. The choice of infill and pattern depends on how strong the printed object should be. The size of the object also affects the infill as a small model can have a high percentage compared to a larger object where the amount of filament starts to play a role. The final step before printing the 3D model is the material consideration. Filament selection is based on the decision of material availability, the purpose of the object, strength and cost (Horvath, 2014).
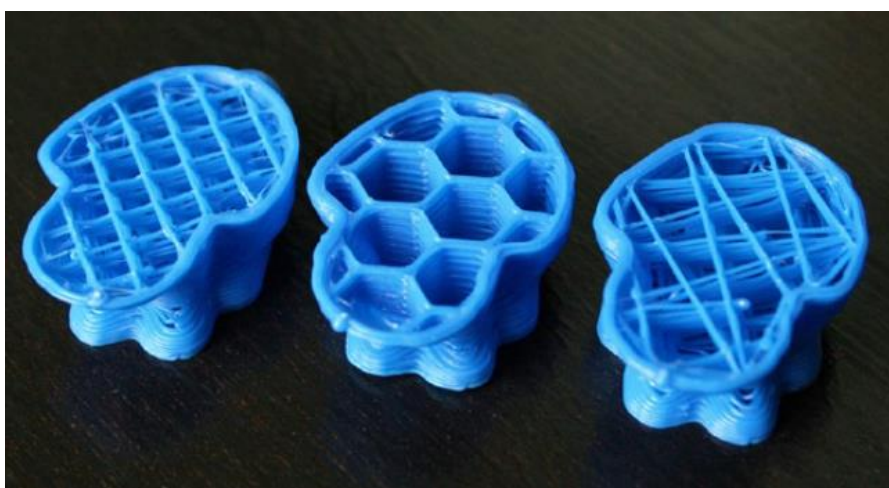


**Figure 2.8: Examples of typical infill patterns (Evans, 2012)**

### 2.4.3   Type of filaments

The different filament materials can introduce a new promising method of creating rail pads. Filament comes in a variety of materials such as plastic, nylon and elastomers that range from flexible to hard and brittle material. The most common 3D printing filaments are ABS (Acrylonitrile Butadiene Styrene), PLA (Polylactic Acid) and PETG (Polyethylene Terephthalate modified with Glycol). It is recommended not to use PLA for prints that might get warm because PLA becomes soft at temperatures above 60 °C, which is the glass transition temperature. The glass transition temperature is the temperature of polymers at which increased molecular movement results in significant changes in the thermal properties (Campo, 2008). The glass transition temperature for PLA, PETG and TPU are 55 °C - 60 °C, 80 °C - 85 °C and 55 °C - 60 °C, respectively (Iannace et al., 2014; Mărieş et al., 2008). ABS is a very durable thermoplastic that is impact resistant and has relatively high heat resistance.

TPE (Thermoplastic Elastomer) and TPU (Thermoplastic Polyurethane) are flexible and abrasion-resistant thermoplastics that can withstand impacts (3Dnatives, 2021). TPU has a linear polymer structure with flexible and rigid chains connected through covalent bonding. Therefore, it demonstrates high flexibility and elasticity as well as impact resistance (Lee et al., 2019). PETG is less elastic, however, it could provide better structural support for embedded instrumentation.

### 2.4.4   Mechanical properties

The American Society for Testing and Materials (ASTM) standards specify tensile and compressive strength tests to determine the Young's Modulus, Poisson's ratio, tensile and compressive strength of thermoplastics. ASTM D412 and D638 are the tensile strength test standards for thermoplastic elastomers and plastics, respectively (ASTM, 2021; ASTM, 2014). The ASTM D638 (ASTM, 2014) standard can be used for PLA, PETG and TPU even though ASTM D412 is for thermoplastics such as TPU. The D638 standard (rigid plastics) specifies dimensions for a specimen of non-rigid plastics according to the D412 standard. ASTM D695 is the compressive strength test of rigid plastics that can be used for PLA and PETG (ASTM, 2015). No compressive standard for testing non-rigid plastics is available.

Wang et al. (2020) and Lee et al. (2019) have studied the mechanical properties of TPU and found that the tensile strength ranges from 21 – 36 MPa. Farah et al. (2016) stated that for commercial PLA the tensile strength and elastic modulus are 59 MPa and 3.5 GPa, respectively. Johnson & French (2018) found that the tensile strength of PLA at 100 % infill percentage tested with the ASTM D638 standard was 32.9 MPa. Srinivasan et al. (2020) found that the tensile strength of PETG at 80 % infill percentage, tested with the ASTM D638 standard, was between

24 and 28 MPa. Kumar et al. (2020) investigated the effect of infill percentage on mechanical properties including hardness, tensile and flexural strength. The main conclusion from the study was that the increase in infill percentage significantly improved the strength and mechanical properties of the printed specimens.

## 2.5    SENSING INSTRUMENTATION

Sensing instrumentation plays an important role in measuring both the performance and the condition of the railway track. Data on how the various components of a railway track respond to a passing train in terms of acceleration, vibration, displacement and loading are necessary for condition monitoring of the railway track. Different sensing instrumentation is available to obtain the above-mentioned information about the track. Various trackside monitoring instrumentation has been shown to provide these measurements, however, they are primarily research equipment that is costly and practical deployments are narrow in scope (Milne et al., 2016). To thoroughly evaluate the structural condition of the railway track, new cost-effective approaches to condition monitoring are required.

Structural Health Monitoring (SHM) is the process of detecting damages to any engineering structures such as buildings, bridges and railway track (Imdad, 2015). With continuous monitoring of the structure through instrumentation, the current condition can be determined. The knowledge of the current condition of railway structures can decrease the cost of maintenance by providing warning signs before any major accidents or faults occur. Current methods of manually inspecting and monitoring the railway are costly, time consuming and prone to human error. Employing small and cost-effective sensing instrumentation for SHM can provide new and promising technologies.

A brief overview of various sensing instrumentation that can be installed inside a rail pad, to monitor track condition and loading, is given in this section of the literature review.

### 2.5.1    MEMS technology

Micro-Electro-Mechanical System (MEMS) is the fabrication of micro-electrical sensors and mechanical parts with integrated signal circuits on a single piece of silicon. Nathanson & Wickstrom (1965) invented and patented the first idea of a MEMS-based device for frequency selection. The working principle of the device is a vibratory member, such as a cantilever, used to control a responsive element, such as a surface potential transistor, to create a "resonant gate transistor."

Only in recent years have MEMS technology been adopted and implemented in instrumentation. Applications that demand low-cost sensors for acceleration and angular motion measurements have demanded the development of MEMS sensors. MEMS-based sensors are implemented in applications where cost, size and power consumption are the driving forces (Titterton & Weston, 2004). There are two types of MEMS technology: capacitive and ohmic. Capacitive-based MEMS sensors measure acceleration based on a change in capacitance due to a moving component or sensing element (Beliveau et al., 1999). Ohmic-based sensors are structured with electrostatically controlled cantilevers (Iannacci, 2017). MEMS-based sensors operate similarly to strain gauges, Linear Variable Differential Transducers (LVDT) and piezoelectric transducers (Nathanson & Wickstrom, 1965). Modern sensing instrumentation utilising this technology includes oscillators, accelerometers, gyroscopes and pressure sensors.

## 2.5.2   MEMS accelerometers

As stated by Lemkin & Boser (1999), the capacitive-based accelerometer measures the displacement of a suspended proof mass in response to an input acceleration. In a typical capacitive accelerometer, the spring-suspended proof mass displaces in the opposite direction of the acceleration and creates an imbalance in the capacitive half-bridge. Two equally sized capacitors are formed between the electrically conductive proof mass and fixed electrodes shown in Figure 2.9. Force balancing is applied to the proof mass through a negative feedback loop. The loop measures the displacement of the proof mass from the original position and applies a force to retain the proof mass centred. The accelerometer output is the force needed to zero the proof mass position.
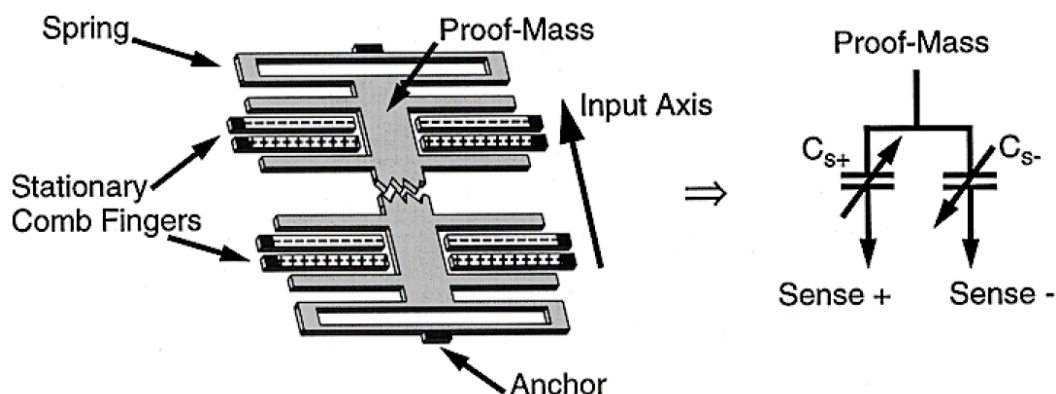


**Figure 2.9: Schematic of sensing element and equivalent electrical model (Lemkin & Boser, 1999)**

Various MEMS and acceleration sensors available today were developed based on this technology, which was first applied in the MEMS-based 50 G accelerometer used in airbag ignition devices (Analog Devices, 1993; Kempe, 2011).

Titterton & Weston (2004) and Castillo-Mingorance et al. (2020) underline the advantages that MEMS accelerometers provide:

- Small size;
- Low maintenance;
- Rugged construction (can withstand shock);
- Low power consumption;
- Good frequency response with little signal noise;
- High volume production results in low-cost units; and
- High reliability and operational in hostile environments.

The evolution of MEMS technology has created devices that range from micrometres to millimetres, in size. MEMS devices can sense and actuate on a micro-scale. Accelerometers, commercially available, are low-power and high-performance three-axis accelerometers. Accelerations ranging from 1 *G* (gravity acceleration in the vertical direction) up to 400 *G* are measurable. The cost of these accelerometers has decreased due to the growth of smartphones, gaming devices and personal cameras utilising this technology.

The LIS331HH is a MEMS digital output 3-axis accelerometer, displayed in Figure 2.10. It has a user-selectable full-scale measurement range of ±6 g/±12 g/±24 g. It is capable of measuring accelerations with an output data rate of up to 1 kHz. The standard output is with a digital I$^2$C/SPI serial interface.
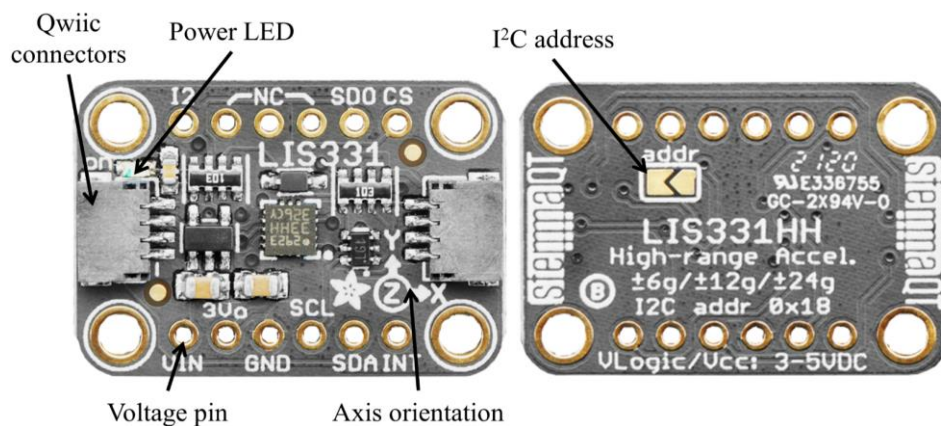


**Figure 2.10: The LIS331 accelerometer (adapted from Adafruit, 2020)**

The Inter-Integrated Circuit ($I^2C$) interface allows the connection of two LIS331HH accelerometers on a single cable. Each accelerometer has a digital address (0x18) and can be changed so that the interface can differentiate between the two accelerometers. The LIS331HH accelerometer is a small, low-power and robust sensor that can be implemented in track components.

Milne et al. (2016) conducted a study to prove the effectiveness of MEMS technologies for smarter railway infrastructure. An inexpensive commercially available MEMS accelerometer was compared to a geophone for determining acceleration and displacements in laboratory and field experiments. The authors noted that in the past, MEMS sensors have had the weakness of accuracy and reliability. Commonly, piezoelectric accelerometers are used for research purposes due to their high precision, however, these are costly compared to MEMS accelerometers. The authors stated that accurate and comparable data from MEMS accelerometers could enable a low-cost and environmentally robust small deployment package for providing data to assess track behaviour. The data captured from the MEMS accelerometer and the geophone, in the performed experiments, was in close agreement. The authors concluded that the results proved that MEMS accelerometers are capable of presenting data of acceptable quality that are comparable to existing trackside monitoring methods. The low cost, robustness and increasing assurance in the quality of measured data, in turn, prove that long-term deployments are attainable. The authors showed the potential of long-term deployment by measuring sleeper displacements over six weeks. The results showed clear changes in the track performance over time as well as the potential of continuous condition monitoring to evaluate the track performance. The study by Milne et al. (2016) demonstrated the robustness and feasibility of MEMS accelerometers for railway condition monitoring. It further proves the concept of creating smart track components for condition monitoring.

Stenström et al. (2019) conducted a condition monitoring study using MEMS accelerometers. The authors designed a prototype accelerometer system that utilises a secondary accelerometer as a wake-up unit that turns the system on with train vibrations. This approach utilises a secondary accelerometer for automatic triggering which can allow remote monitoring of track conditions. The accelerometer is connected to an Arduino MEGA 2560 with an analog-to-digital converter (ADC) connection. The results from the study were in line with those from Milne et al. (2016).

### 2.5.3 Strain Gauges

The term "strain" is used to describe the contraction or elongation of a material due to an applied force or temperature effect. In turn, the two cases of strain that can occur are called mechanical

or thermal strain. Strain gauges are utilised to measure the absolute change in the length of a section. There are various types of strain gauges including metal, semiconductor, vapor-deposited (thin-film), capacitive, piezoelectric, photoelastic and mechanical strain gauges (Hoffmann, 1989).

The working principle of electrically resistive metal strain gauges is that the strain transferred to the strain gauge from the measurement section causes a change in the electrical resistance of the strain gauge (Hoffmann, 1989). This principle is based on the strain/resistance relationship of electrical conductors which was discovered by Wheatstone and Thomson (Wheatstone, 1843; Hoffmann, 1989). The resistance of any electrical conductor is changed with mechanical stress through compression or tension forces. According to Hoffmann (1989), the resistance change is partially due to two aspects: the conductor's deformation and the change in the resistivity $Q$ of the conductor material. The strain gauge is connected to a Wheatstone bridge to accurately measure the small changes in electrical resistance and to mitigate any resistance changes due to temperature variation. The relationship is represented by the following equation (Hoffmann, 1989):

$$\Delta R/R_0 = \underbrace{\epsilon \, (1 + 2v)}_{\substack{\text{geometrical} \\ \text{portion}}} + \underbrace{\Delta Q/Q}_{\substack{\text{Micro-} \\ \text{structural} \\ \text{portion}}} \qquad \text{(Equation 2.6)}$$

where $R$ = electrical resistance, $\varepsilon$ = strain, $v$ = Poisson's ratio and $Q$ = resistivity. It is assumed that the strain from the object is transferred to the strain gauge without any loss in strain. This assumption requires a very close bond between the object and the strain gauge.

The supply voltage ($V_s$) applied to the circuit is divided into the two halves of the bridge $R_1$, $R_2$ and $R_4$, $R_3$ as a ratio of the relating bridge resistances. Each half of the bridge forms a voltage divider. The simplified ratio in the circuit is given by:

$$\frac{V_o}{V_s} = \frac{k}{4}\left(\varepsilon_1 - \varepsilon_2 + \varepsilon_3 - \varepsilon_4\right) \qquad \text{(Equation 2.7)}$$

where $V_0$ = bridge output voltage, $k$ = k-factor of the strain gauge and $\varepsilon$ = strain associated with each resistance. When strain measurements are taken with a measuring instrument, the following effects occur (Hoffmann, 1989):

- Positive indication if $\varepsilon_1 > \varepsilon_2$ and/or $\varepsilon_3 > \varepsilon_4$; and
- Negative indication if $\varepsilon_1 < \varepsilon_2$ and/or $\varepsilon_3 < \varepsilon_4$.

It is noted by Hoffman (1989) that the inequality symbols "<" and ">" apply in the algebraic sense and not in the magnitudes. An ADC is needed to measure the output voltage from the strain gauge using the Razor. Figure 2.11 displays various configurations of the XY (T Rosette) strain gauges from HBM (2021).
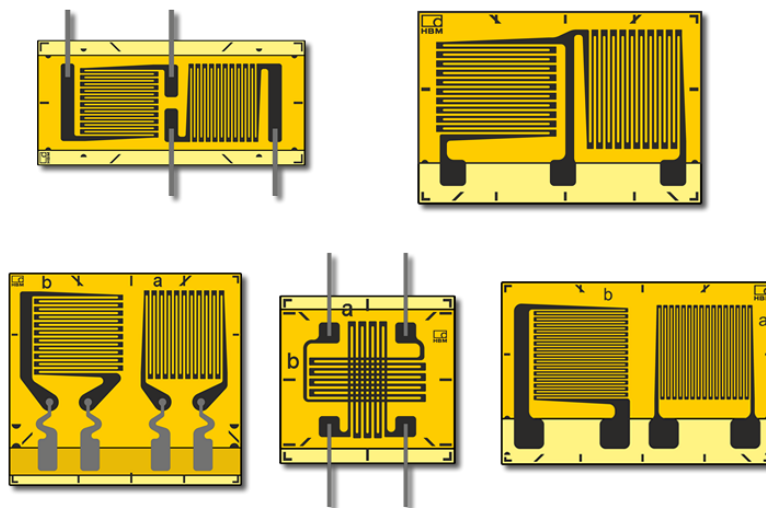


**Figure 2.11: XY (T Rosette) strain gauges with 2 measuring grids for analysing Biaxial Stress States (HBM, 2021)**

As mentioned by Hoffmann (1989), a Wheatstone bridge circuit is used to determine the relative changes in electrical resistance in strain gauge measuring techniques. The output from an electrically resistive strain gauge is usually measured with a Wheatstone bridge circuit. The amount and the position of the strain gauges in the Wheatstone bridge circuit determine the sensitivity of the circuit. The flexibility of the circuit allows it to be used in a wide range of applications. Figure 2.12 provides a schematic layout of the main types of circuits. The resistors with a diagonal line represent the active strain gauges while the rest act as the completion resistors of the same resistance.
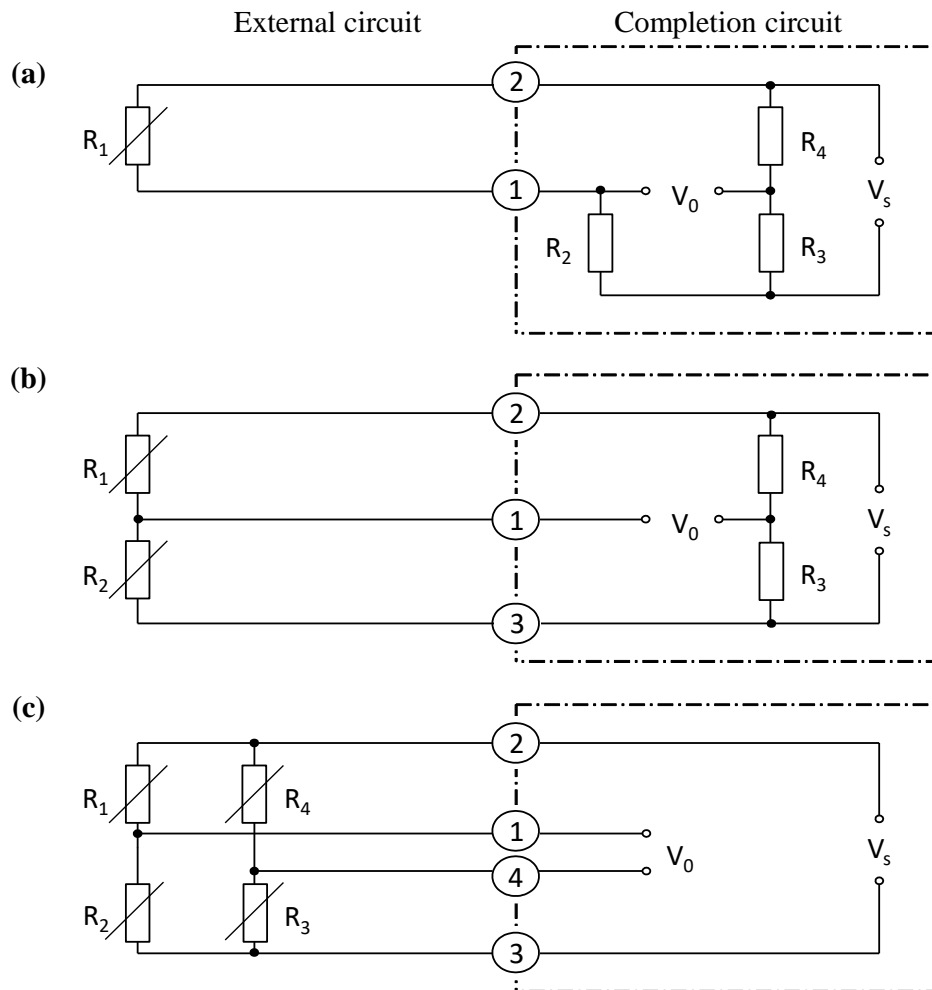
**Figure 2.12: Wheatstone bridge configurations for strain gauge techniques: a) Quarter bridge, b) Half-bridge and c) Full bridge (adapted from Hoffmann, 1989)**

### 2.5.4   Fibre Bragg Grating (FBG)

Hill et al. (1978) discovered the photosensitivity of optical fibre and the permanent formation of gratings. It was observed that light sent through the fibre was being reflected as a function of time. This was due to light-induced refractive index changes in the core of the optical fibre.

In 1997, Hill & Meltz created a fundamental overview of Fibre Bragg grating (FBG) technology. In an FBG sensor, a periodic change of the refractive index occurs when the fibre core is exposed to a severe optical intrusion pattern. The first fabrication method for Bragg gratings was internal writing (Hill et al., 1978) and the holographic technique (Meltz et al., 1989). The phase mask technique is the current widely used method of fabricating Bragg gratings in the optical fibre core. The core region has a greater refractive index than the silica cladding surrounding the core. Light is trapped inside the core because of total internal reflection at the core-cladding boundary

(Kashyap, 1999). The value of the refractive index ($\Delta n$) depends on factors such as intensity, wavelength, amount of exposed light and the composition of the glass fibre core (Hill & Meltz, 1997). The periodic structure formed in the core allows an opposite propagating wave, producing a reflected light to couple the incident signal illustrated in Figure 2.13.
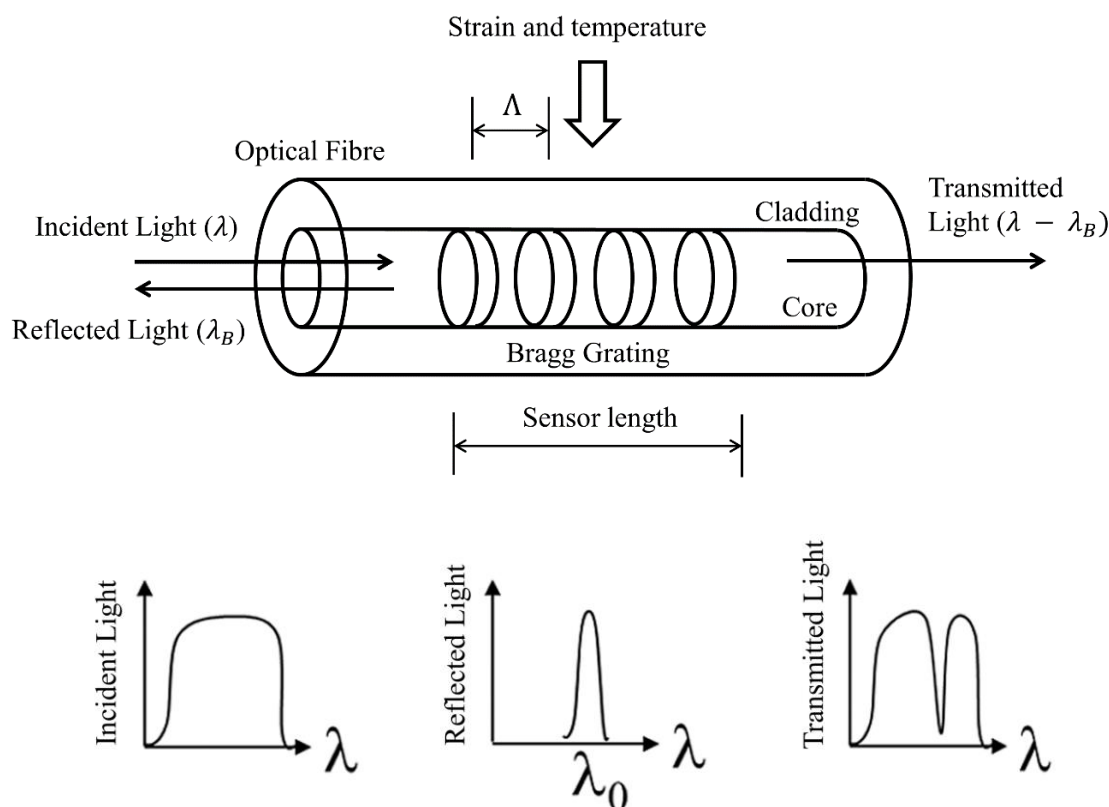


**Figure 2.13: Schematic of the principle of an FBG sensor (redrawn from Hill & Meltz, 1997; Ramakrishnan, 2016)**

Hill et al. (1978) provided the resonance equation where the reflected light from the grating occurs at the Bragg wavelength ($\lambda_B$) given by:

$$\lambda_B = 2n_{eff}\Lambda \hspace{6cm} \text{(Equation 2.8)}$$

where $n_{eff}$ is the effective refractive index and $\Lambda$ is the grating period or spacing. Both these terms are dependent on strain and temperature (Kersey et al., 1997). In practical applications, any wavelength shift is due to a combined effect of strain and temperature perturbations (Qi, 2011). When the FBG is used as a direct sensing element for strain and temperature, the combined effect of these two aspects provides a variation in the grating period and refractive

index (Du et al., 2020). Thus, provision should be made to compensate for the cross-sensitivity between strain and temperature when the FBG is used as a strain sensor. Two FBGs with the same central wavelength can be used where one is for the strain measurement and the other for temperature (Chiang et al., 2001). Temperature can be compensated for by placing two FBGs close to each other to make the wavelengths shift by the same amount in response to temperature (Dong & Tam, 2008).

López-Higuera (2002) stated that fibre optics have two disadvantages namely: (1) the cross-sensitivity between temperature and strain of Bragg gratings and (2) the cost of optical sensors (which has declined in the last two decades). The disadvantage that López-Higuera (2002) did not mention is the interrogation methods required to measure the reflected wavelength. Interrogation of the FBG utilises an expensive and bulky optical spectrum analyser (OSA) (Sahota et al., 2020).

Hong et al. (2019) designed and tested a 3D printed FBG pressure sensor. The pressure sensor was fabricated from PLA filament utilising the material extrusion additive manufacturing (MEAM) process. No glue or epoxy was used as adhesive to adhere to the FBG inside the pressure sensor. The authors concluded that an FBG sensor can be successfully embedded inside fused PLA material. This study forms a good proof of concept for a 3D printed rail pad with the PLA structure carrying 2000 kPa.

FBG sensors can be placed inside a 3D printed rail pad to measure strain and or wheel load. The main disadvantage of FBG sensors is the expensive interrogator that must be used whenever a measurement is taken. It is therefore not suitable for a low-cost remote monitoring solution.

### 2.5.5 Microcontroller/Microcomputer

Microcontrollers are typically used in control applications where a single task or a single group of tasks needs to be performed. A microcontroller is a microcomputer that has its memory and input/output (I/O) interface integrated on a single chip. A microcomputer is a computer built with a microprocessor (CPU) and other external components for the memory and the I/O interface. Microcomputers can also contain microcontrollers such as those used on the Raspberry Pi. Microcontrollers and microcomputers are built for different purposes. Microcontrollers perform more basic tasks and require fewer components whereas microcomputers perform difficult computations and require more power to do so (Cady, 2009).

The Arduino microcontroller is based on the Atmel 8-bit microcontroller family. It was developed in 2005 as a project for students at the Design Institute of Ivrea in Italy. The goal was to develop an easy-to-use open-source hardware and software platform. Arduino IDE is the

software program, paired with the hardware, which is written in Java and based on the programming language C. The microcontroller has analog inputs and digital I/O pins for connecting instrumentation and modules. It features onboard memory, time, various ports and processor systems as well as a 10-bit ADC (Barrett, 2013; Abdukarimov, 2019). Figure 2.14 displays the Arduino MEGA microcontroller with the various inputs and systems built in.
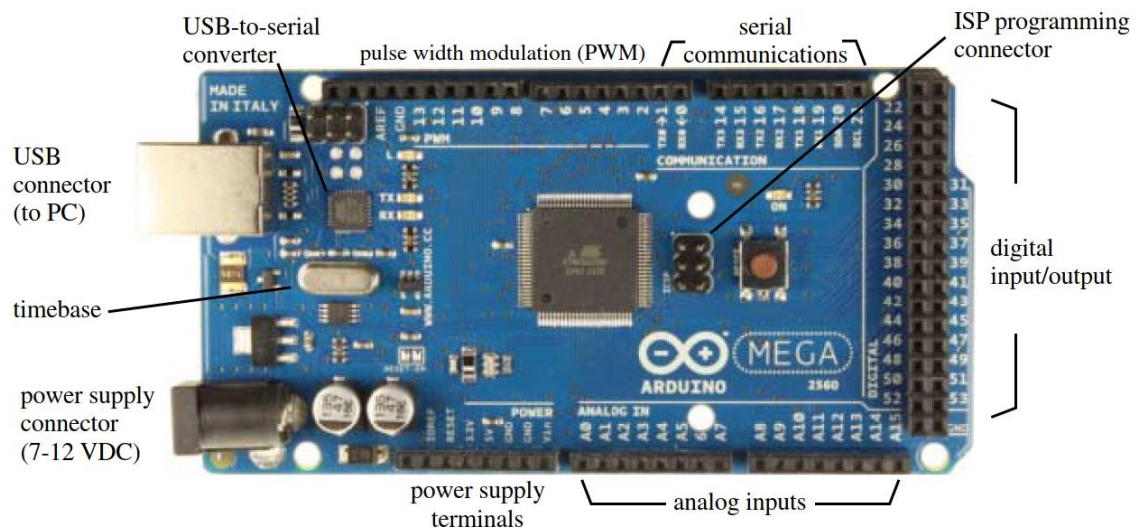


**Figure 2.14: Arduino MEGA 2560 with inputs and built-in systems (Barrett, 2013)**

The advantage of the Arduino microcontroller is code efficiency and simplicity. The open-source aspect of the Arduino allows anyone to publish and create code for any application. Important factors to consider about microcontrollers include power consumption, flash memory, clock speed, analog or digital input/outputs, reference voltage, SRAM (Static random-access memory) and EEPROM (electrically erasable programmable read-only memory). SRAM is where the coded sketch creates and manipulates variables as it runs the code.

The 9DoF Razor IMU combines an SAMD21 microprocessor with an MPU-9250 (9 degrees of freedom) sensor to create a 3 mm x 3 mm x 1 mm (width × length × thickness) sized inertia measurement unit (IMU), shown in Figure 2.15. The MPU-9250 features three 3-axis sensors namely an accelerometer, gyroscope and magnetometer. This gives it the ability to measure linear acceleration and angular rotation velocity. The onboard microprocessor, Atmel's SAMD21, is an Arduino compatible, 32-bit ARM Cortex M0+ microcontroller.
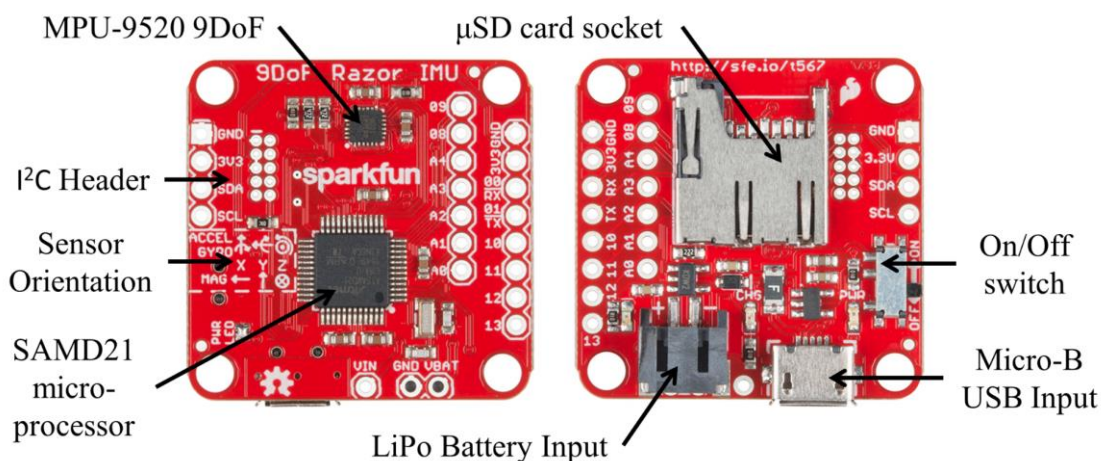
**Figure 2.15: Razor 9DoF Schematic (Adapted from SparkFun, 2016)**

Due to its small size, the Razor can be placed inside an enclosure, with a battery, that can be mounted onto the rail. A triggering system can be added via code that monitors the built-in accelerations from the MPU-9520 and triggers the Razor to start logging the external instrumentation. The trigger system monitors accelerations and starts logging when the accelerations are above a user-defined threshold and returns to monitoring when below the threshold. This configuration allows the measurement of trains without manual triggering or human interaction; thus, trains can be measured remotely. Accelerations from the rail and smart rail pad can be measured at the same time from the Razor when mounted to the rail. This provides enough information to measure any wheel defects that are present.

## 2.6    SMART RAIL PADS

Smart rail pads are a new concept that has only been researched and developed to a limited extent. Measurements from inside the rail pad can be obtained by the installation of instruments such as accelerometers, piezoelectric sensors, force sensors and fibre optics. Operational aspects such as accelerations, vibrations, axle load, frequency and temperature can be measured using sensing instrumentation installed inside a rail pad. The measurements will enable condition monitoring of the track structure. Zhang et al. (2018) suggested that because the rail pad is the component connecting the rail and the sleeper, it could provide useful information such as details on the load transmitted to the substructure when instrumented with load sensing capabilities. Instrumenting the rail pad with load sensing capabilities can enable the replacement of expensive weighbridges. Measuring accelerations in the rail pad can provide a better understanding of the acceleration and vibration dissipation of the track superstructure. This

understanding is crucial for the minimising of vibrations propagating through to the substructure.

Woschitz (2011) proposed the development of a rail-strain-pad (RASP) using FBG sensors. Newly developed pads are tested in test tracks over several years with no information about the stress and strain behaviour inside the pad. Woschitz (2011) suggested investigating the strain measurement inside a rail pad for material optimisation. Several FBG sensors were installed on a single fibre inside the rail pad. The fibre optic sensors were integrated into the rail pad during manufacturing to minimise the risk of damaging the sensors. Figure 2.16 shows the schematic of the RASP and its realisation.
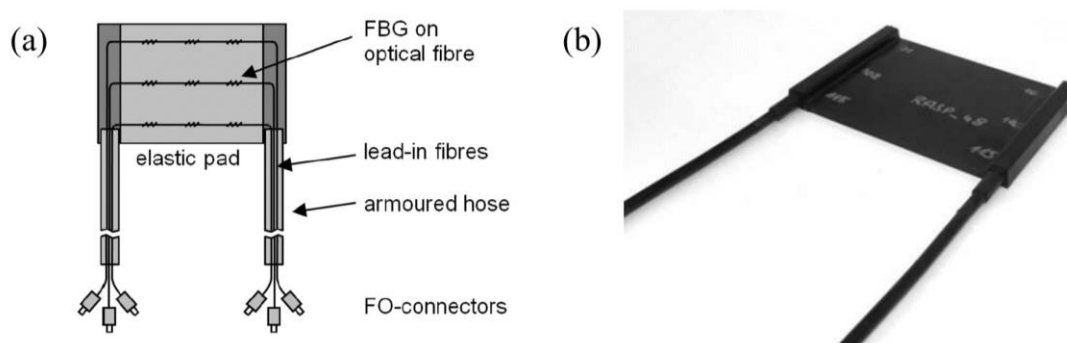


**Figure 2.16: (a) Schematic of the rail-strain-pad and (b) its realisation (Woschitz, 2011)**

Woschitz (2011) stated that the behaviour of negative strain present in the middle of the rail pad was previously unknown, and it suggests a non-linear Poisson's ratio for the rail pad. Field tests were carried out on a narrow curve section of track. A large wavelength difference between the field and the laboratory results was observed. Woschitz (2011) noted that the conditions in the laboratory and the field are different and that the knowledge about strain in the rail pad in real conditions is important for material optimisation. The author concluded that FBG sensors of the recoating type did not withstand the large strain values applied during dynamic loading. Draw-tower-gratings were found to be more suitable sensors for the application. The high elasticity of the rail pad makes sensing solutions a complicated task.

Prefabricated Fibre Optic Rail Pad Sensors (FORPS) are commercially available from a company based in Germany. The SL FORPS UIC 60 is, for example, designed to measure vertical wheel loads, vibrations and shocks in a wide frequency range for train and track maintenance diagnostics purposes. When a load is applied to the FORPS, it causes a decrease

of light transmitted through the fibre optic structure and with help from an optoelectronic interface it analyses the amount of light arriving at the opposite end (Sensorline, 2009).

Zhang et al. (2014) researched the effectiveness of a FORPS in monitoring and identifying wheel flats. Two methods were used in the study to identify the wheel flats. The first method was by impact load estimation where the wheel-rail interaction force is predicted after receiving the force-time history from the sensor. The second method comprises a genetic algorithm to identify the shape, length and depth of the wheel defect as well as the position where the impact occured. The authors concluded that the first method cannot recover the whole impact force as well as the estimation of wheel flat size. The advantage of the first method is the fast computational time making it suitable for real-time monitoring. The disadvantage of the second method is the computation time which makes it more applicable for offline applications.

Zhang et al. (2018) proposed a rail pad sensor for wheel-rail contact force monitoring. The proposed rail pad sensor consists of thin piezoelectric PVDF (polyvinylidene fluoride) sensing strips that are placed on top of an existing rail pad. The PVDF sensing strips have metalized electrodes on the top and the bottom and they are wrapped in an insulation layer. A sliding layer was placed inside the shielding layer to prevent excessive stretching of the PVDF film. The total thickness of the sensor is approximately 0.65 mm. The rail pad sensor was tested in both the laboratory and the field.

Zhang et al. (2018) concluded that the low-cost sensor displayed good linearity within the load scheme tested and functioned well under dynamic loading in both laboratory and field conditions. The rail pad sensor can be used to monitor the rail seat load; therefore, it can be used as a weigh-in-motion system as well as for the monitoring of surface defects. The authors noted that the system does not have a "blind" zone problem which the conventional strain gauge-based wheel load monitoring system has.

The results from the study showed that the PVDF rail pad sensor can accurately measure the rail seat load and detect any surface defects on train wheels. The low-cost aspect is relative to the location of the study and expensive data acquisition equipment was used to measure with the PVDF rail pad sensor. The data acquisition equipment cannot be left on site for remote monitoring of the track and rolling stock conditions. Thus, a solution where a system can automatically trigger to log the data from a smart rail pad and store it for post-processing is needed. A cross-section diagram of the rail pad sensor is shown in Figure 2.17.
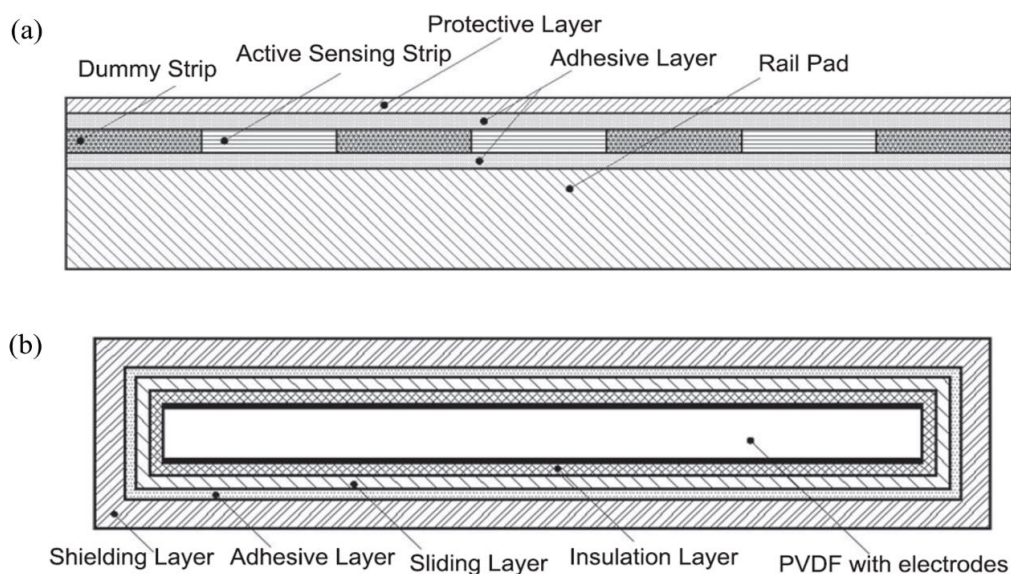
**Figure 2.17: (a) Cross-section of the rail pad sensor and (b) cross-section of one active sensing strip (Zhang et al., 2018)**

Sol-Sánchez et al. (2021a) studied the ability of a smart rail pad made from recycled polymers equipped with a conventional and low-cost piezoelectric device to monitor both rolling stock and track conditions. The rail pad and capsules comprised 50 % recycled HDPE (from recycled industrial plastic boxes) and 50 % rubber from discarded tyres. Both materials were melted and mixed before being poured into a mould. The piezoelectric sensor had a circular quartz sheet with a diameter of 24 mm placed on top of a metallic base (with 35 mm diameter). The total thickness of the sensor was 0.35 mm. A hole was drilled deep enough to protect the sensor from any damage from direct contact with the rail. Full-scale laboratory tests were conducted to determine three key aspects: (a) assessment of the piezoelectric sensors in the track components; (b) ability of smart components to measure traffic load; and (c) ability of smart components to monitor superstructure performance.

Sol-Sánchez et al. (2021a) observed from the results that lower signal values were recorded on the softer support, suggesting that the smart rail pads need calibration according to field conditions when absolute values are required since the boundary conditions could influence the rail pads. The authors concluded that both smart components demonstrated the capacity to detect traffic load changes. The authors also concluded that the smart rail pad provides a suitable solution for measuring traffic conditions and surface defects in the wheel-rail contact as well as the potential to be used for monitoring track functionality through changes in load distribution of the superstructure. The design and placement of the rail pad are shown in Figure 2.18.
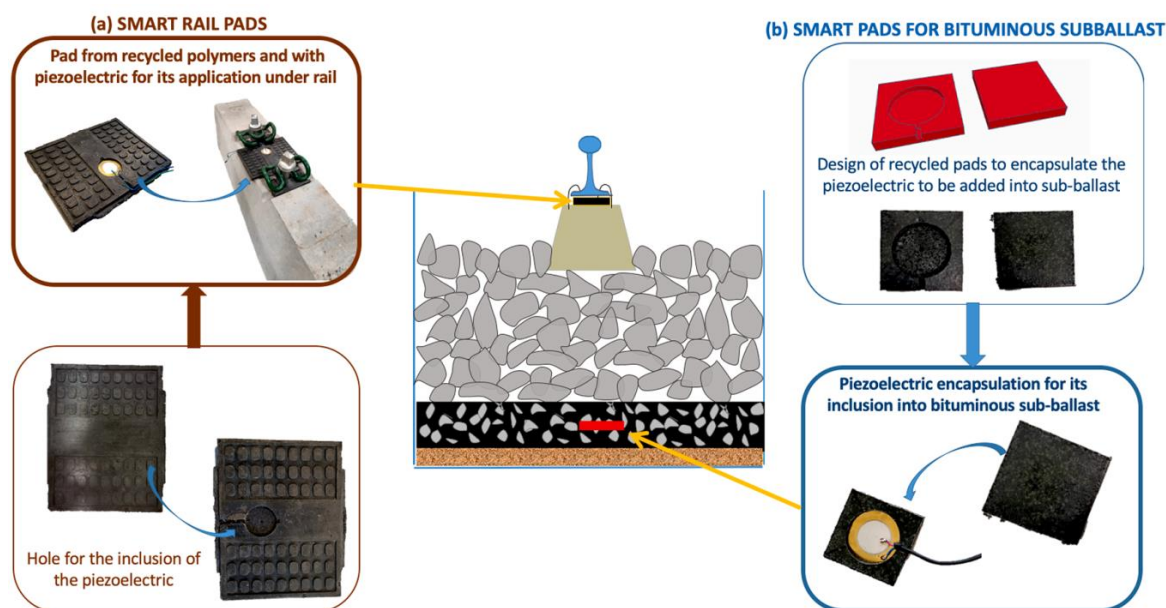
**Figure 2.18: Design of the smart rail pad and pads (Sol-Sánchez et al., 2021a)**

## 2.7 FUTURE OF RAILWAYS

According to the International Transport Forum (2011), passenger movement will increase by 200 - 300 % and freight supply by 150 – 200 %, in the next 30 years. To combat the rapid increase in transport demand, smart solutions will be required to accomplish adequate capacity. More intelligent and integrated systems are required for moving passengers and freight. Machine-to-machine (M2M) and Information Communication Technology (ICT) will increase efficiency by embedding sensors into a wide variety of objects to provide real-time analysis and continuous monitoring of assets (ARUP, 2019). Embedding accelerometers and strain gauges inside a 3D printed casing to create a smart rail pad will offer insight into the operation of a rail pad under in-service conditions. The accelerations and forces from a smart rail pad can provide conditional information about the train wheels as well as the rail. This information will be advantageous for predictive and preventative maintenance actions of train wheels and the rail.

## 2.8 GUIDANCE FROM THE LITERATURE

This chapter gives a brief overview of the track structure focusing on the rail pad. It provides background and application of 3D printing technology to fabricate a rail pad. Various types of instrumentation that can be installed inside a rail pad were discussed including MEMS accelerometers, strain gauges and FBG sensors. Previous research on smart rail pads was provided and discussed.

The previous literature and research on smart rail pads provided evidence that it is possible to produce a condition monitoring system by installing sensing instrumentation inside a track component. To date, no smart rail pad has been created that incorporates accelerometer and strain gauge technology. Previous research did not consider the possibility of fabricating a low-cost remote monitoring system that automatically detects an oncoming train and captures data from instrumentation inside a smart rail pad. Fabricating a rail pad from 3D printing filament is unexplored and can provide an exciting avenue for new possibilities. Creating a rail pad from 3D printing material can simplify the process of embedding instrumentation inside a rail pad to protect said instrumentation. Accelerometers inside the rail pad can provide monitoring of wheel defects when high impact forces occur. The magnitude and type of forces exerted on a rail pad can also be measured. Load sensing capabilities using strain gauges can provide the wheel load at the rail seat area which provides an insight into the wheel load distribution from the rail to the sleepers. Calibrating the smart rail pad to field conditions allows for direct wheel load measurement.

# 3 EXPERIMENTAL SETUP AND METHODOLOGY

This chapter provides a detailed description of the experimental setup and methodology followed during the research. The majority of the testing was performed at the University of Pretoria in the Engineering 4.0 Concrete Laboratory Gauteng as well as on an existing railway line near the South African town of Vryheid in KwaZulu-Natal.

The main experiment was to test the use of a 3D printing filament as a rail pad and the implementation of instrumentation embedded inside for condition monitoring in the laboratory and the field. Additional tests were conducted to determine material properties and prototyping of the smart rail pad.

## 3.1 MATERIAL TESTING

This section covers the material testing that was conducted on the three chosen 3D printing filaments namely PLA, PETG and TPU. The mechanical properties such as Young's modulus, compressive and tensile yield strength, were determined for each filament. The material testing was done according to the ASTM standards D638 and D695 for tensile and compressive plastic material testing, respectively (ASTM, 2014; ASTM, 2015).

### 3.1.1 Tensile Strength

According to the ASTM D638, a dog bone-shaped specimen is used to test the tensile strength of plastics (ASTM, 2014). The dimensions of the dog bone specimens differ for the rigid and non-rigid plastics. The specified specimen shapes are the following: Type I for rigid plastics and Type IV for nonrigid plastics and these are displayed in Figure 3.1. The dimensions displayed in Figure 3.1 include the width and length of the narrow section, the overall width and length and the thickness. As specified by ASTM D638 (2014), the minimum number of specimens needed for repeatability is five specimens. For testing purposes, five specimens of each of the three filaments at four different infill percentages (25 %, 50 %, 75 % and 100 %), with the "line" infill pattern, were tested. A total of 60 specimens were tested. An extensometer was only used on PLA and PETG and not on TPU because of its maximum extension of 5 mm. The TPU specimens were smaller in size due to the elasticity of the material and thus would extend further than the maximum limit of the extensometer.

(a) Type I specimen
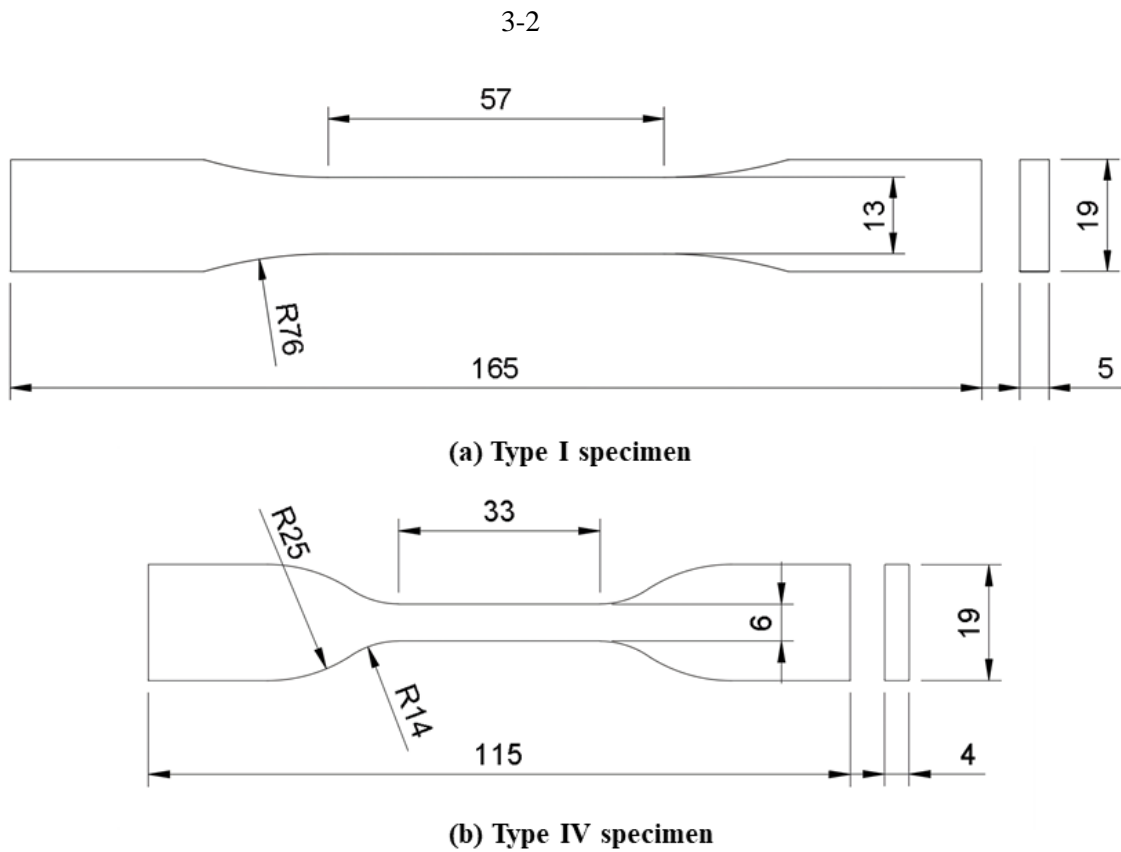


(b) Type IV specimen

**Figure 3.1: Dimensions (in mm) according to ASTM D638. (a) Type I and (b) Type IV specimen (ASTM, 2014)**

The speed of testing is measured in millimetre per minute (mm/minute). The speed of testing for rigid and nonrigid plastics were 5 mm/min and 50 mm/min, respectively. Tensile testing was conducted on a Lloyd LRX-Plus testing machine with a force range of 5 kN, as illustrated in Figure 3.2.
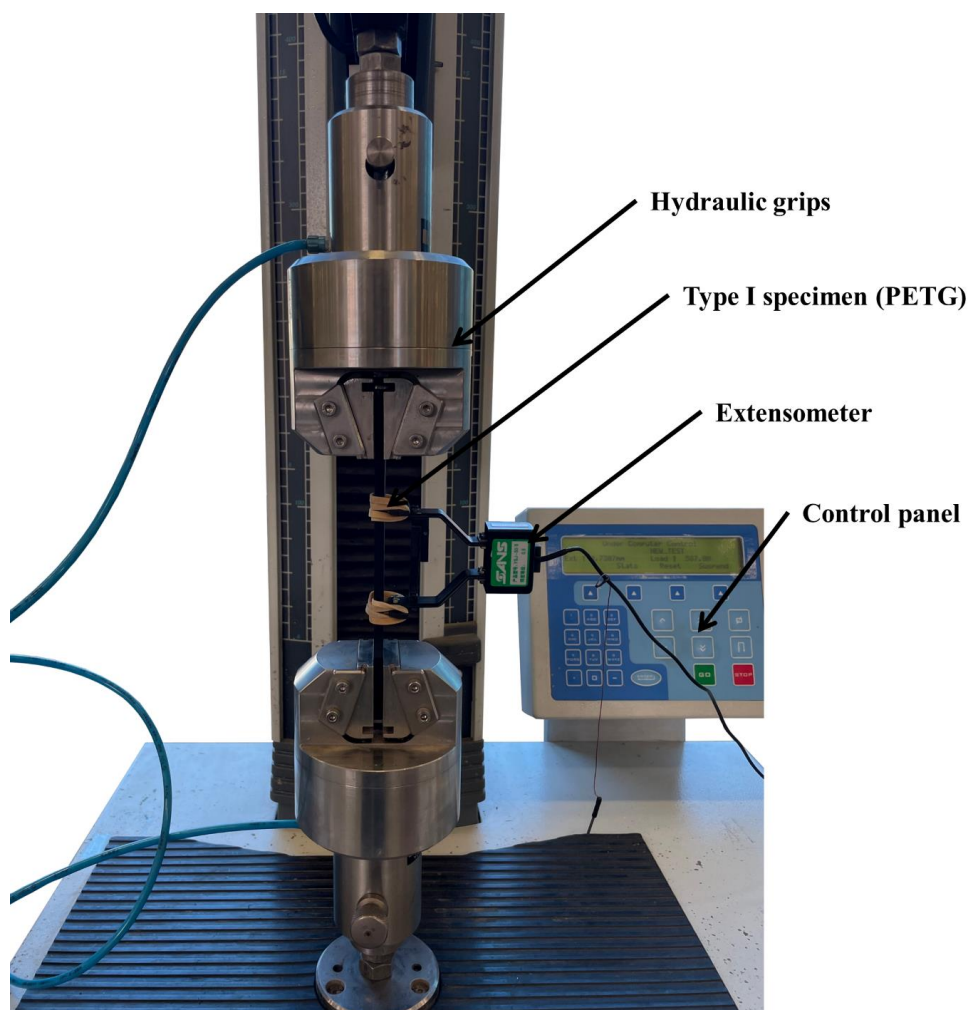
**Figure 3.2: Tensile strength setup**

### 3.1.2 Compressive Strength

According to ASTM D695, a standard-sized prism of $12.7 \times 12.7 \times 25.4$ mm is used to test the compressive strength of rigid plastics (ASTM, 2015). For testing purposes, five specimens of the PLA and PETG filament at four different infill percentages (25 %, 50 %, 75 % and 100 %), with the "line" infill pattern, were tested. A total of 40 specimens were tested. The speed of testing for compression was 1.3 mm/min. A Lloyd testing machine with a force range of 50 kN was used, shown in Figure 3.3
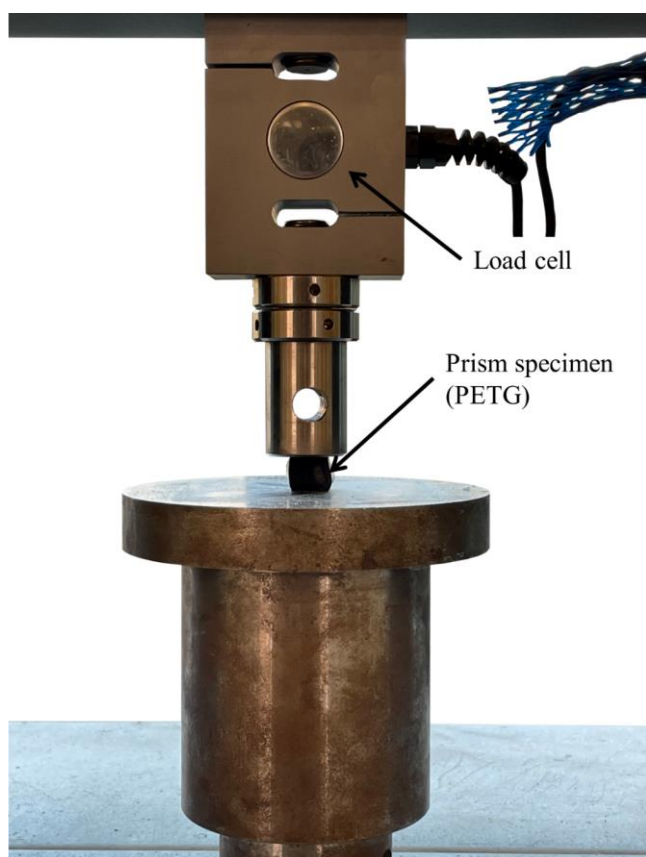
**Figure 3.3: Compressive strength setup**

## 3.2    PRINTING PROCESS

This section covers the printing process of the test prints, prototypes and the final smart pad. The printing was done on two different 3D printers: CReality CR-6 and CR-10 MAX.

### 3.2.1    Small scale test prints

Small-scale rail pads were printed to test various printing settings such as infill percentage, infill pattern, print temperature and speed. The "line" infill pattern was preferred because it uses less material compared to other infill patterns and it provides the best infill coverage from corner to corner. The techniques used by Hong et al. (2019) of stopping the printing process at 50 % and embedding the instrumentation inside before covering it with further printing and only using epoxy or glue where necessary, was used for all the 3D printed pads in this study. The small-scale test prints were used to test this procedure of stopping the printer at 50 % and then placing an object inside such as an instrument. Figure 3.4 displays the small-scale test prints at a 50 % printing percentage.
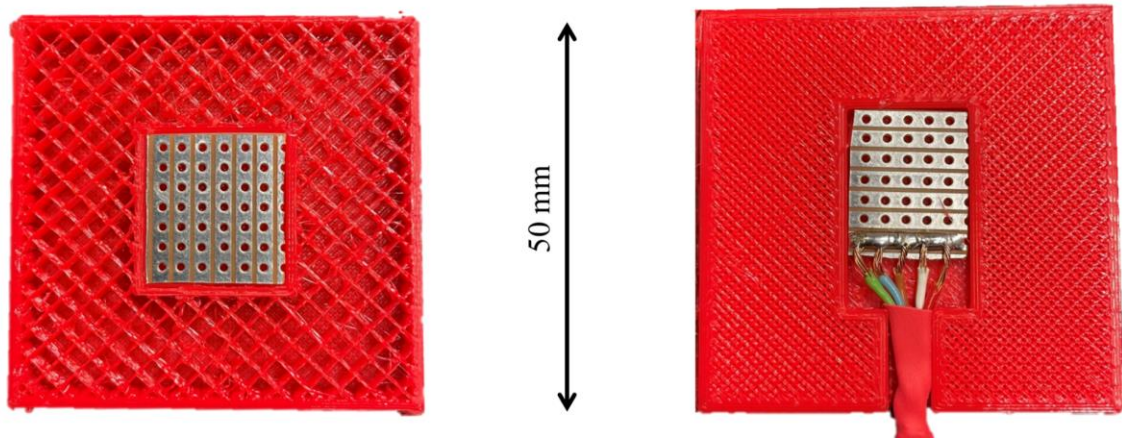
**Figure 3.4: Small scale test prints with a small circuit board to represent an instrument**

## 3.3 FULL-SCALE TEST PRINTS

Various rail pad designs can be used for a 3D printed rail pad. The optimal design must be at a height, high enough to accommodate all the instrumentation required inside while still providing enough structural support. The standard Hytrel studded rail pad design is only 3 mm thick in the middle section with 2 mm high studs on each side. Even though this design provides the best resiliency, there is not enough space for the planned instrumentation. The rail pad thickness was chosen as 10 mm to provide enough support above and below the instrumentation. This thickness is similar to an HDPE pad that was replaced in the field experiment. For simplification, the 3D printed rail pad was a rectangular shape of 168 mm $\times$ 175 mm $\times$ 10 mm (width $\times$ length $\times$ thickness). The width of 168 mm is the distance between the fastening supports of the sleeper in the laboratory. The width of 168 mm is small enough to conform to the field conditions. A simple rectangular design provides the most space for the instrumentation as well as shortens the printing time required.

Full-scale test pads were printed using the acquired information from the half-scale prints. Three different 3D printing filaments were tested namely PLA, PETG and TPU. All three test prints had a 50 % infill percentage with the "line" infill pattern. Figure 3.5 displays a full-scale test pad in the CURA software.
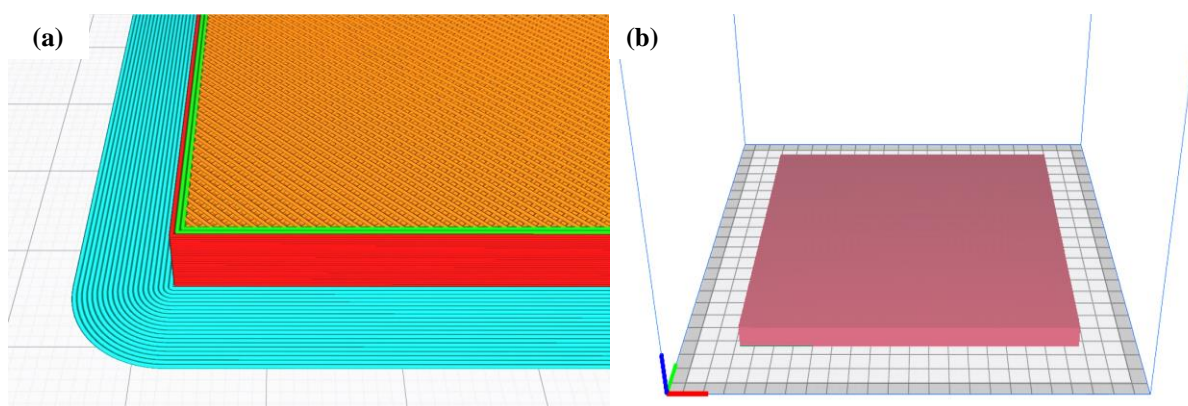
**Figure 3.5: (a) Infill pattern and density of 50 % and (b) preview of the rail pad in the CURA slicing software**

Table 3.1 provides the print settings for each test print that was entered in CURA to generate the G-code for the CReality CR-6 3D printer. The 3D printed pads were printed using a 0.4 mm nozzle in the extruder. The use of a 0.8 mm nozzle can decrease the print time because it needs to place fewer layers due to the increase of material flow through the extruder. The printing time for the final rail pad design was decreased to six and seven hours for PLA and PETG from 10 and 15 hours, respectively, with the use of a 0.8 mm nozzle on the CReality CR-10 MAX printer.

**Table 3.1: Printing settings for each test print**

| Filament | Infill [%] | Print speed [mm/second] | Layer Height [mm] | Temperature [°C] | | Print time [hours] |
| | | | | Extruder | Print bed | |
|---|---|---|---|---|---|---|
| PLA | 50 | 100 | 0.2 | 215 | 60 | 10.3 |
| PETG | 50 | 60 | 0.2 | 235 | 70 | 14.8 |
| TPU | 50 | 35 | 0.15 | 230 | 70 | 38.4 |

The printing speeds vary greatly due to the different levels of difficulty in printing each filament and in particular TPU. TPU is flexible and requires a slower printing speed to allow for the elastic filament to extrude through the nozzle. It must be printed on the CReality CR6 printer due to the length of the Bowden tube feeding the filament to the extruder being short enough to not cause problems. A direct-drive printer is recommended for TPU filaments because TPU can

clog the extruder of a Bowden tube printer. The overall print time for TPU was not feasible for printing prototypes or even for a small amount of TPU rail pads. PLA and PETG are rigid and are easy to print therefore the print speed can be increased. PLA and PETG have a short enough printing time such that it can be printed overnight. Using a 0.8 mm nozzle can allow the printing of two rail pads in one day.

### 3.3.1    Cyclic loading test procedure

The material testing was conducted on 6 – 14 April 2021 at the Engineering 4.0 laboratory on the Hillcrest Campus of the University of Pretoria. Cyclic testing was performed to determine whether the 3D printed rail pads can withstand the dynamic forces of an existing railway line. The rail pads tested under cyclic loading were the 3D printed pads as well as an HDPE and a Hytrel pad. Figure 3.6 displays the various pads that were tested with the sizing of each.
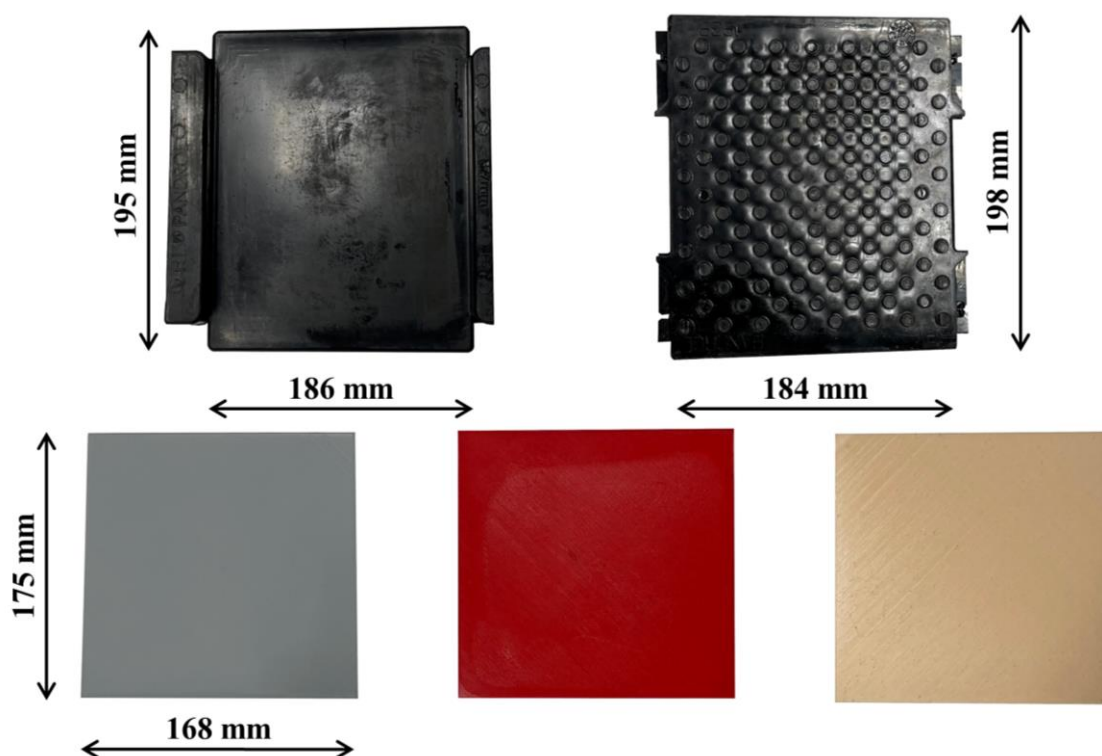


**Figure 3.6: Top left to right: HDPE; Hytrel. Bottom left to right: PLA; PETG; TPU**

The cyclic tests were performed on a hydraulic actuator that forms part of a load frame to create a load unit referred to as the Materials Testing System (MTS). The hydraulic actuator has a force capacity of 500 kN for both compression and tension. The maximum displacement length

of the piston is 150 mm. The hydraulic actuator can apply loads at a maximum frequency of 30 Hz granted that the piston displacement is small enough (Van Niekerk, 2021). The experimental setup consisted of a half-track structure that can be used in this way due to its longitudinal track symmetry. The rail was placed on top of the pad and fastened down with e-clips. The track structure was not placed inside a ballast box to mitigate the damping that the ballast would provide. This decision was taken to simulate higher forces than that on an existing track structure. This provided superior data on whether the 3D printed rail pads could withstand the forces exerted by a moving train. The experimental setup is displayed in Figure 3.7.
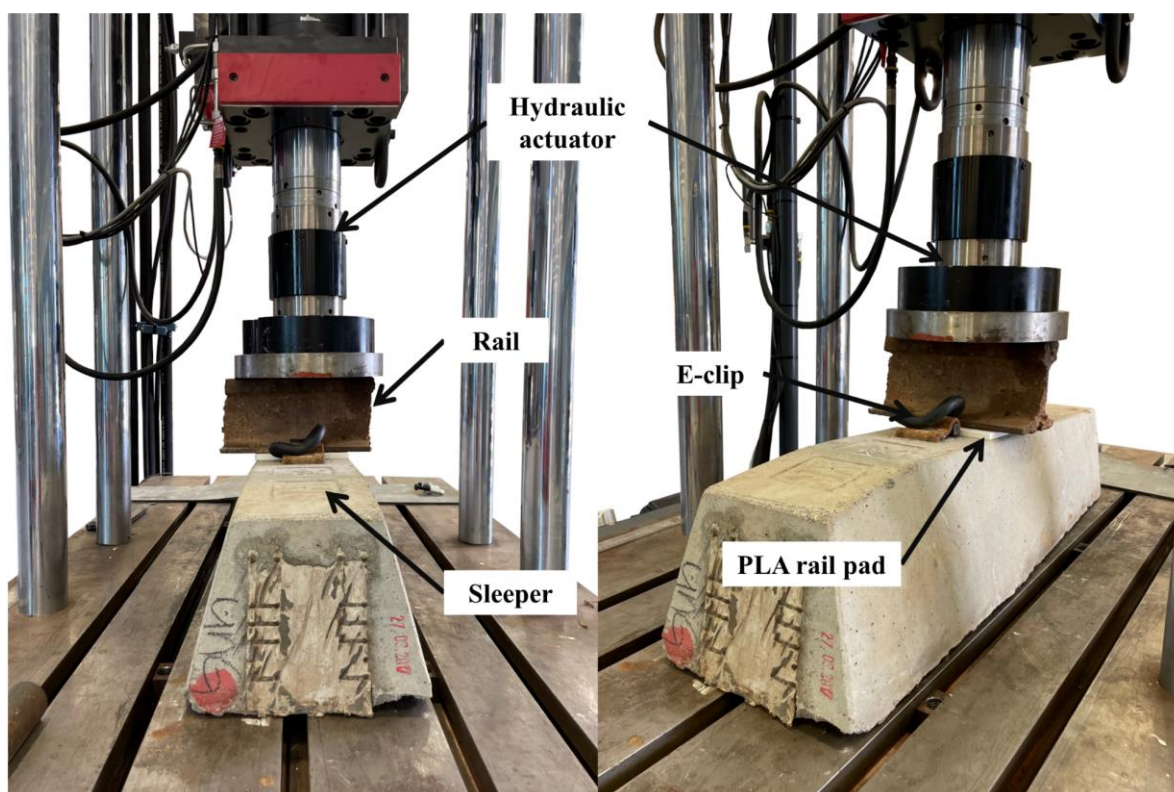


**Figure 3.7: Hydraulic actuator and experimental components**

The magnitude for the cyclic and static loading was the maximum rail seat load of 60 kN for general freight and passenger trains. The chosen load distribution percentage of 45 % of the wheel load was based on the findings of Russel et al. (2020) and Profillidis (2000). Although only one sleeper was used on the hydraulic actuator, the loading magnitude was chosen for field conditions. The maximum rail seat load includes a dynamic impact factor according to the Eisenmann (1972) approach given in Table 3.2.

**Table 3.2: Summary of variables for the maximum load calculation (from Broekman, 2018)**

| Parameter | Value | Unit |
|---|---|---|
| Average axle load for general freight and passenger trains | 18 | *tonnes* |
| Static wheel load, $P_{static}$ | 88.3 | *kN* |
| Vehicle speed, $V$ | 90 | *km/h* |
| $\eta$ | 1.214 | |
| Track condition, $\delta$ | 0.2 | |
| $t$ | 2 | |
| Dynamic impact factor, $\varphi$ | 1.486 | |
| Dynamic wheel load, $P_{dyn}$ | 131.2 | *kN* |
| Load distribution factor (Russell et al., 2020) | 45 | *%* |
| Maximum rail seat load, $q_r$ | 60 | *kN* |

The cyclic testing frequency was determined using the equation below in a sinusoidal pattern. A sinusoidal vibration wave is generated with a frequency $f$ when a wavelength $\lambda$ is present on the rail and travels at a speed $V$ written as (Thompson, 2009):

$$f = \frac{V}{\lambda} \qquad \qquad \text{(Equation 3.1)}$$

The frequency is in Hz where $\lambda$ is given in m and $V$ in m/s. The cyclic loading was applied at a frequency of 25 Hz. This frequency was determined using Equation 3.1. The vehicle speed of 165 km/h corresponds to the frequency of 25 Hz that is experienced by the rail. A wavelength of 1.83 m was used which is the axle distance of a CR-13 or CCR-11 coal wagon on the heavy haul line in South Africa. Heavy haul lines operate at low speeds (typically on average of 50 km/h). The frequency of 25 Hz corresponds to speeds above the upper limit for heavy haul lines in South Africa. Thus, the testing frequency is greater than that on a normal heavy haul line. According to Aursudkij et al. (2009), the typical loading frequency is between 8 - 10 Hz (assuming a train speed of 75 - 94 km/h and an axle spacing of 2.6 m) and up to 30 Hz for high-speed trains. The testing frequency of 25 Hz simulates high frequencies that can occur on an existing railway line due to wheel flats and vehicle or track irregularities. The high frequency

was chosen to test the 3D printed rail pad through more rigorous conditions to ensure that the 3D printed pad can operate as an existing rail pad and be able to protect the instrumentation contained within the rail pad. A cyclic test procedure was set up on the MTS testing software to control how the actuator performs. The cyclic test procedure is illustrated in Figure 3.8. A pre-load of 2 kN was applied from which the static test started to evenly apply 60 kN on the rail. The clamping force of 18 kN was already applied on the test track structure using e-clips (Sainz-Aja et al., 2020). After the static test, the cyclic testing of 100,000 cycles was repeated five times for a total of 500,000 cycles.

```
┌─────────────────────────────┐
│      Ramp up  to 2 kN       │
└─────────────────────────────┘
              │
              ▼
┌─────────────────────────────┐
│   Ramp from 2 kN – 60 kN in 60
│  seconds and back from 60 kN – 2 kN
│   in 60 seconds. Sampled @ 100 Hz
└─────────────────────────────┘
              │
              ▼
┌─────────────────────────────┐
│   Repeat cycle loop 5 times │
└─────────────────────────────┘
 ┌ ─ ─ ─ ─ ─ ─ ─│─ ─ ─ ─ ─ ─ ┐
              ▼
 │┌─────────────────────────┐│
  │   1000 cycles  @ 25 Hz  │
 ││  Between  2 kN – 60 kN   ││
  │    Sampled @ 500 Hz     │
 │└─────────────────────────┘│
              ▼
 │┌─────────────────────────┐│
  │  99000 cycles  @ 25 Hz  │
 ││  Between 2 kN – 60 kN     ││
  │  Sampled @ 1 Hz and 100 Hz│
 │└─────────────────────────┘│
              ▼
 │┌─────────────────────────┐│
  │  Rest period of 5 minutes│
 │└─────────────────────────┘│
 └ ─ ─ ─ ─ ─ ─ ─│─ ─ ─ ─ ─ ─ ┘
              ▼
┌─────────────────────────────┐
│    1000 cycles  @ 25 Hz     │
│   Between  2 kN – 60 kN      │
│     Sampled @ 500 Hz        │
└─────────────────────────────┘
              │
              ▼
┌─────────────────────────────┐
│      Ramp down to 2 kN      │
└─────────────────────────────┘
              │
              ▼
┌─────────────────────────────┐
│   Ramp from 2 kN – 60 kN in 60
│  seconds and back from 60 kN – 2 kN
│   in 60 seconds. Sampled @ 100 Hz
└─────────────────────────────┘
```
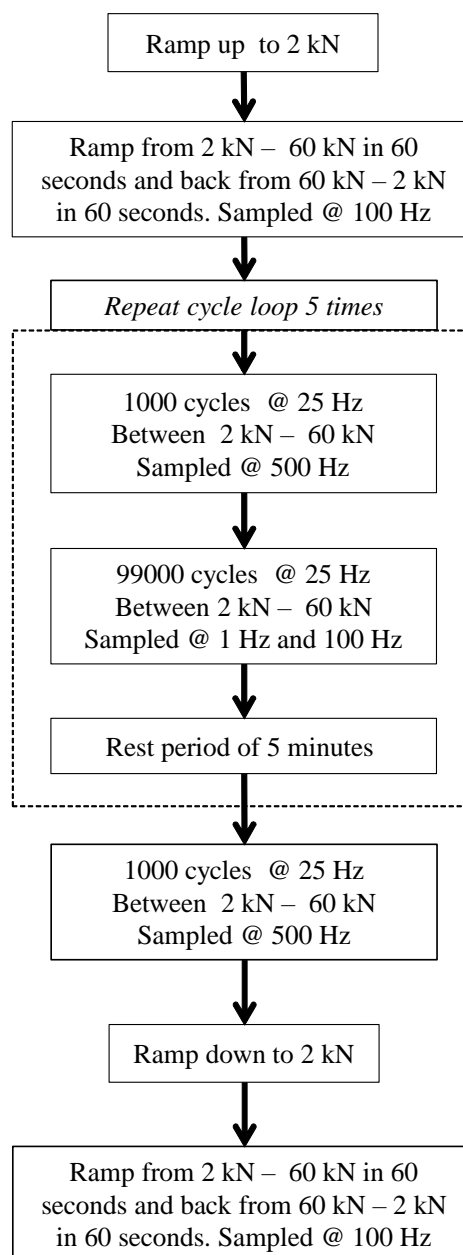
**Figure 3.8: Cyclic testing procedure**

The dynamic stiffness, $k_{dynamic}$, was calculated with a similar formula as Sainz-Aja et al. (2020). The formula determines $k_{dynamic}$ as the ratio between the average load range and the average displacement range from the first 1000 cycles of each 100,000-cycle stage, as well as the final 1000 cycles written as:

$$k_{dynamic} = \frac{\overline{F_{max}} - \overline{F_{min}}}{\overline{D_{max}} - \overline{D_{min}}}$$
(Equation 3.2)

Where $\overline{F_{max}}$ and $\overline{F_{min}}$ correspond to the average maximum and minimum applied force and $\overline{D_{max}}$ and $\overline{D_{min}}$ correspond to the average measured maximum and minimum deflection.

### 3.3.2 Static test procedure

Two static tests were conducted before and after each cyclic test. The purpose of the first static test was for initial loading and unloading while the second static test was for comparison to the first. The second static test also provided insight into the stiffening of the test pads after cyclic loading. The static loading consisted of a pre-load of 2 kN with an increasing load from 2 – 60 kN in 60 seconds and unloading back to 2 kN in another 60 seconds.

Five individual static tests were also conducted on each test pad. This was done to confirm the initial static tests as well as for the calculation of the static stiffness of each pad. The static stiffness, $k_{static}$, was calculated using a similar method presented by Sainz-Aja et al. (2020). The formula determines $k_{static}$ from, the ratio of the difference between the load range and the displacement range, from the last loading ramp written as:

$$k_{static} = \frac{F_{final} - F_{initial}}{D_{final} - D_{initial}}$$
(Equation 3.3)

Where $F_{final}$ and $F_{initial}$ correspond to the initial and final applied force in the static test and $D_{final}$ and $D_{initial}$ correspond to the initial and final measured deflection associated with the previously mentioned applied force. The dynamic and static stiffness for each tested rail pad is presented and evaluated in Section 4.2.

### 3.4 PROTOTYPE TESTING

This section gives an overview of the experimental setup of the two prototype pads: the Accelerometer prototype and the Strain prototype.

### 3.4.1   Introduction

The initial prototype testing was done with an inexpensive accelerometer (ADXL 335) to determine whether the PETG rail pad can protect an accelerometer embedded inside the rail pad while cyclic loading is applied. The final design would incorporate two accelerometers that can measure greater accelerations experienced inside a rail pad. The strain prototype included an XY-1 Rosette strain gauge that was configured as a Wheatstone half-bridge. The calibration of the ADXL 335 accelerometer and the HBM WI/10 mm LVDT is given in Appendix A1.

### 3.4.2   Experimental setup of the Accelerometer prototype

The prototype was printed from PETG filament with the same printing settings as the full-scale test prints, which was 50 % infill percentage and "line" infill pattern. Figure 3.9 illustrates the embedding process of the accelerometer from interrupting the printer at 50 % to the encapsulating of the accelerometer. The accessibility of embedding the accelerometer in the rail pad was enhanced by the ability to pause the printer. The printer retained the temperature of the extruder and the print bed at the correct temperature and can continue printing at any moment. Once the printer was paused, the extruder moved to the edge of the print bed which allowed for the installation of the accelerometer.
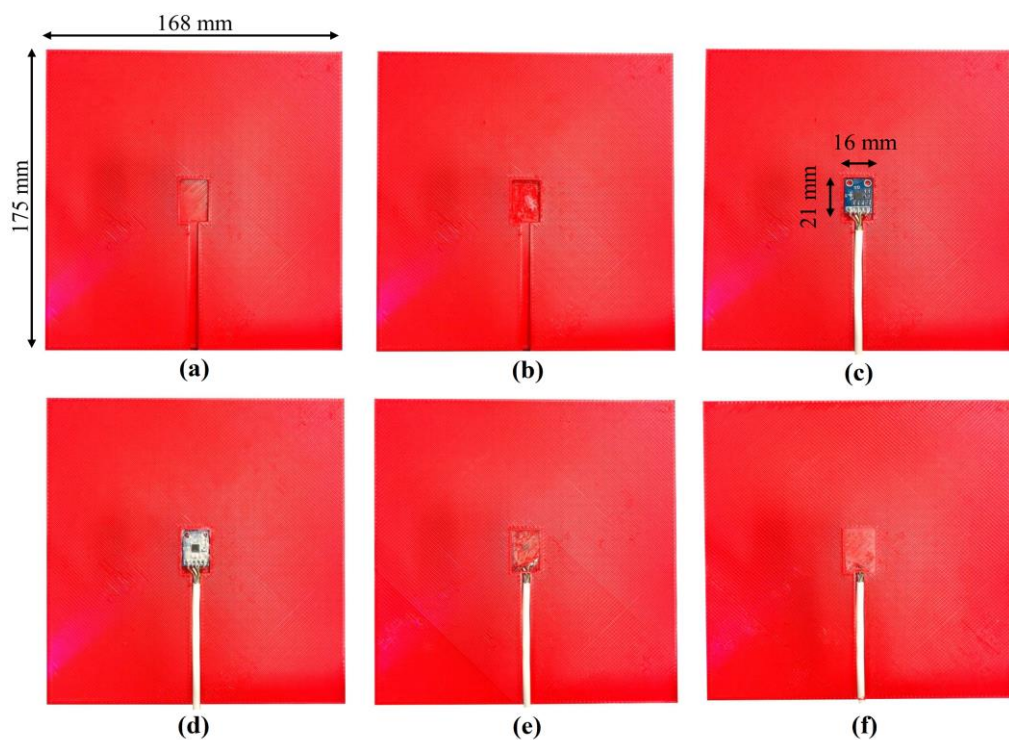


**Figure 3.9: Embedding process of accelerometer – (a) Printer paused at 50 % printing process, (b) layer of silicon for adhesion, (c) accelerometer placed, (d) layer of nail polish**

**to protect the accelerometer from moisture, (e) printed first top layer and (f) printed second top layer**

The prototype was tested on a hydraulic actuator for 1000 cycles at eight different frequencies with an applied maximum rail seat load, $q_r$ of 86 kN. The maximum load was updated for heavy haul freight with an axle load of 26 ton/axle and included the dynamic load factor according to the Eisenmann (1972) approach. The dynamic impact factor calculation is given in Table 3.3.

**Table 3.3: Summary of variables for the maximum load calculation (from Broekman, 2018)**

| Parameter | Value | Unit |
|---|---|---|
| Axle load | 26 | *tonnes* |
| Static wheel load, $P_{static}$ | 127.53 | *kN* |
| Vehicle speed, $V$ | 90 | *km/h* |
| $\eta$ | 1.214 | |
| Track condition, $\delta$ | 0.2 | |
| $t$ | 2 | |
| Dynamic impact factor, $\varphi$ | 1.486 | |
| Dynamic wheel load, $P_{dyn}$ | 189.47 | *kN* |
| Load distribution factor (Russell et al., 2020) | 45 | *%* |
| Maximum rail seat load, $q_r$ | 86 | *kN* |

A wide range of frequencies that exist on a railway was tested with the applicable train speed that the frequency corresponds to, which is summarised in Table 3.4. Equation 3.1 was used with the wavelength of 1.83 m to calculate the effective train speed. Priest et al. (2010) stated that the following loading frequencies by pairs of bogies at the ends of adjacent wagons (1 Hz), individual bogies (2 Hz) and axles (6 Hz) are apparent on a railway line. The other frequencies (8 – 25 Hz) were included to simulate the higher frequencies that could occur on a railway line due to wheel flats or rail and wagon irregularities.

**Table 3.4: Tested frequencies and the respective train speed**

| Frequency [Hz] | Effective Train speed [km/h] |
|:---:|:---:|
| 1 | 7 |
| 2 | 14 |
| 6 | 40 |
| 8 | 53 |
| 10 | 66 |
| 15 | 99 |
| 20 | 135 |
| 25 | 165 |

The prototype was placed in the same half-track structure with a 60 kg/m rail and e-clips as the fasteners, illustrated in Figure 3.10. An external HBM WI/10 mm LVDT was placed on the rail with the reference to the sleeper to measure the rail pad deflection. The external LVDT measures the pad deflection more accurately than the internal LVDT of the hydraulic actuator. A bracket was specially built to hold the LVDT in place on the foot of the rail displayed in Figure 3.11. The LVDT was placed parallel to the load path of the hydraulic actuator. Supports were attached to the loading frame to hold the sleeper in place and reduce any unnecessary movement. Keeping the half-track structure as motionless as possible allowed for a more accurate measurement of the acceleration and deflection that the rail pad experienced. The Arduino Mega, running the code to measure the accelerations, was placed next to a laptop that was used as a data acquisition system. Due to the ADXL335 being an analog accelerometer, the sampling rate was not programmable, and it was affected by the speed of the microcontroller and the data acquisition software. The sampling frequency range from the data acquisition laptop was 480 – 500 Hz.
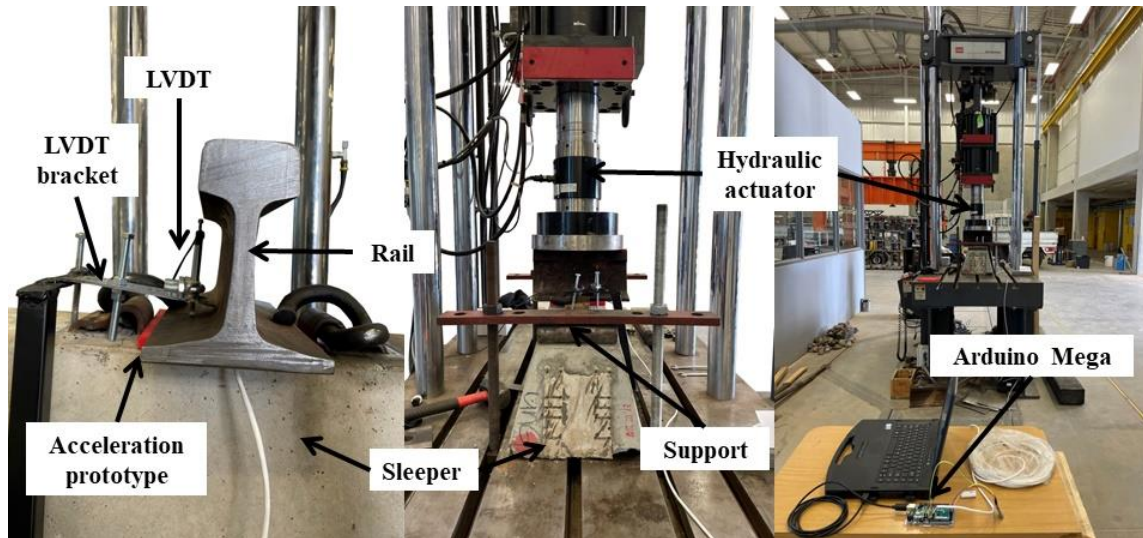
**Figure 3.10: Experimental setup for acceleration prototype testing**
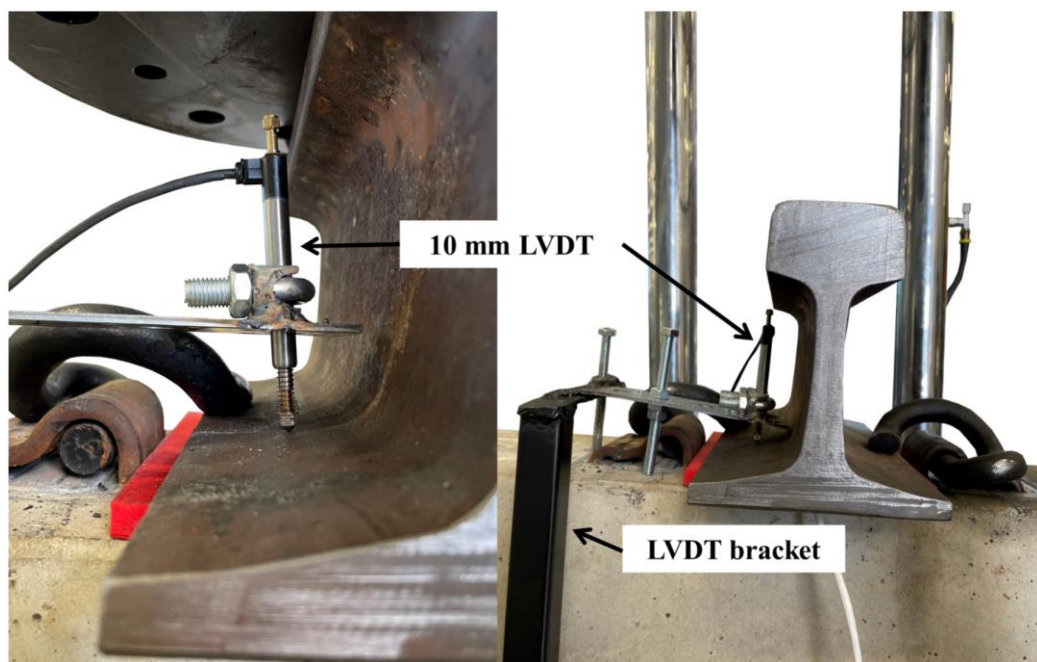


**Figure 3.11: LVDT placement and bracket**

### 3.4.3 Experimental setup of the Strain prototype

The Strain prototype was printed with the same print settings as the Accelerometer prototype, including the 50 % infill and "line" infill pattern. To save time in printing the prototype, the Strain prototype was printed on the CR-10 MAX rather than the CR-6. Figure 3.12 illustrates the embedding process, from preparation to the gluing of the strain gauge with X60.
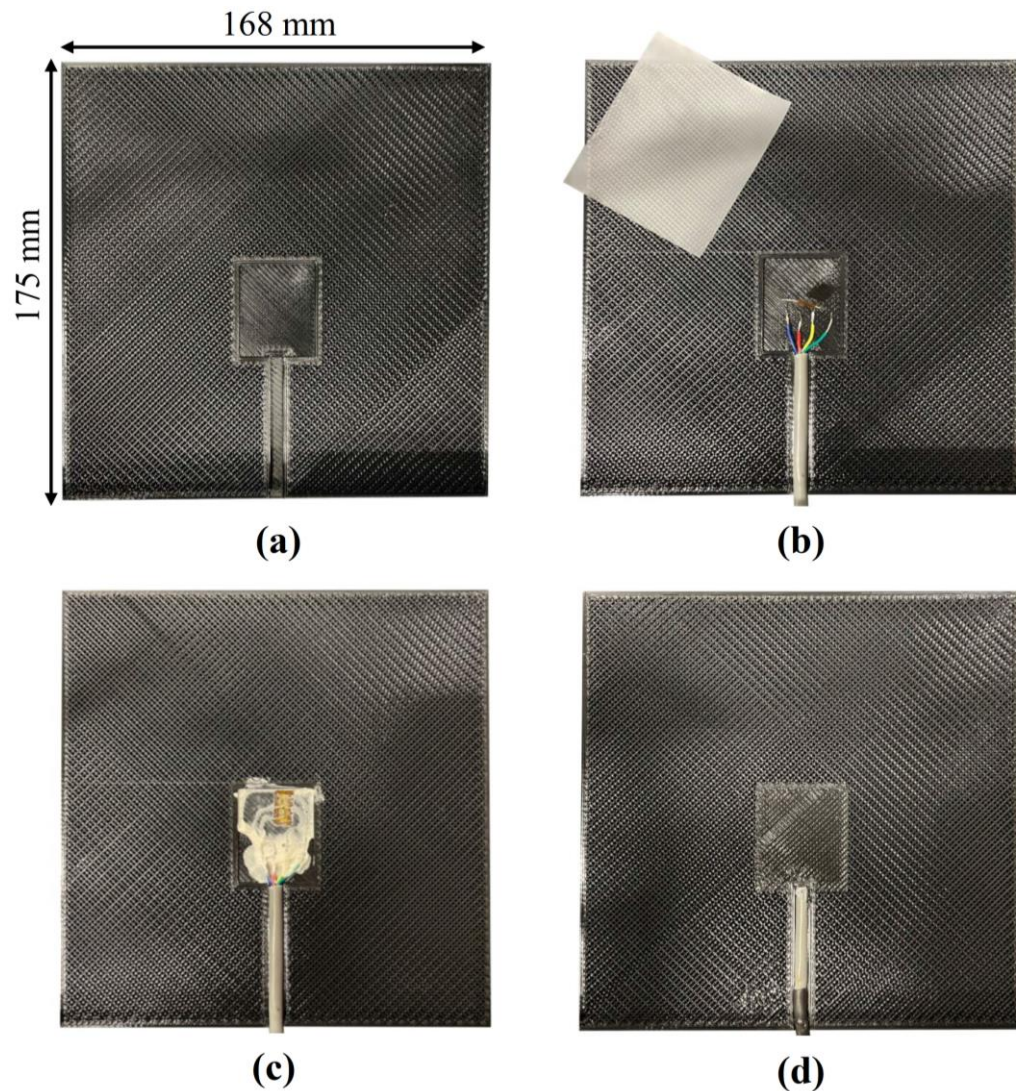
**Figure 3.12: Embedding process of strain gauge – (a) Printer paused at 50 % printing process, (b) preparation of strain gauge to adhere to the pad, (c) glued strain gauge, (d) printed third top layer**

X60 is a two-part glue that is typically used to adhere strain gauges to various surfaces, such as concrete or steel. It consists of a powder Part A and a colourless liquid Part B. X60 was placed beneath the strain gauge as well as over the wires to secure all parts in place. X60 can loosen when heated. To prevent this from happening, the print bed was kept at 30 °C, instead of the 70 °C normally used for PETG. A thin paper sheet was used to press down on the strain gauge. This was necessary to flatten and press out any excess glue beneath the gauge. The strain gauge was configured in a Wheatstone half-bridge to increase the sensitivity of the strain gauge, while compensating for temperature changes that could have an undesired effect. The chosen strain gauge was the 120 Ω XY-1 Rosette which can easily be used in a half-bridge configuration.

Two 120 Ω precision resistors were used for the completion circuit that was built into the external measuring enclosure.

The experimental setup for the Strain prototype was similar to the Accelerometer prototype, as seen in Figure 3.13. The prototype testing was done to determine whether strain can be measured from the strain gauge, in the middle of the rail pad. The output from the strain gauge was measured with the Razor microcontroller and an HBM acquisition system. This was done to confirm that the completion circuit and strain gauge were working as expected. The HBM acquisition system completes the Wheatstone bridge, inside the connection, and does not need an external completion circuit.
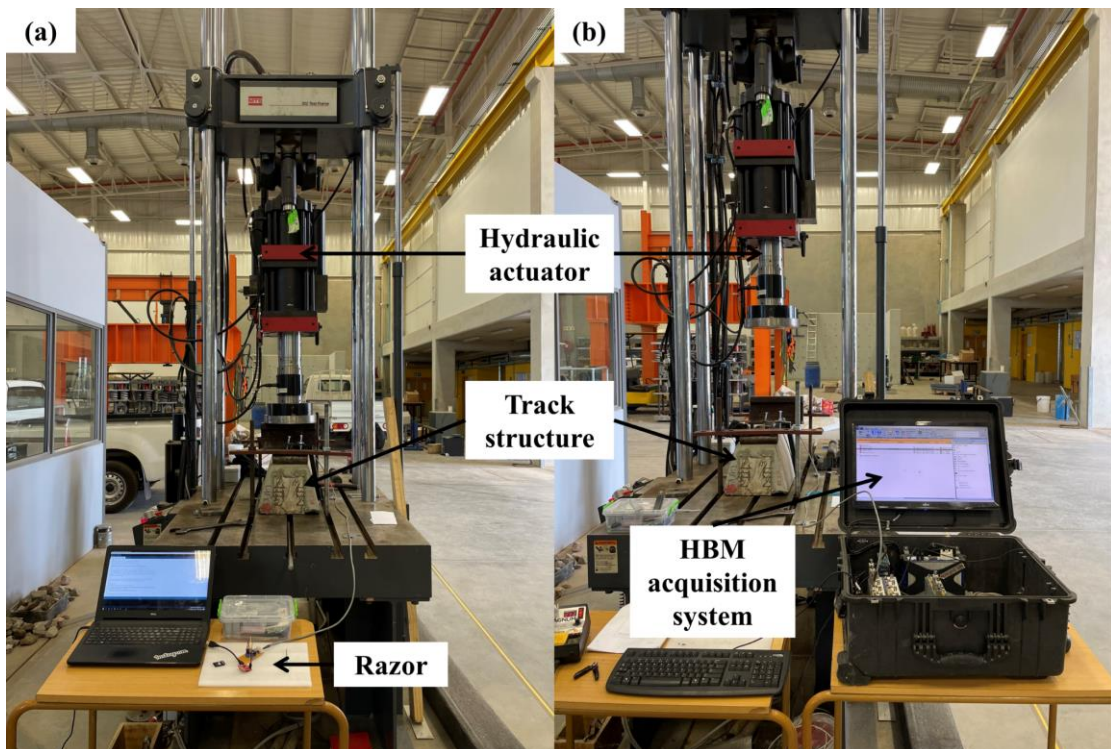


**Figure 3.13: Strain prototype experimental setup: (a) measuring with the Razor and (b) validating the prototype with the HBM system**

The testing procedure for the Strain prototype consisted of both cyclic and static loading. The cyclic loading scheme was as follows: 10 cycles of 86 kN at 0.25, 0.5, 0.75, 1, 2, 6 and 8 Hz to evaluate the signal response from the strain gauge at different frequencies. The initial cyclic test was done twice. Thereafter, another two cyclic tests of 2 – 8 Hz were done. Two different static tests were done: (1) series of increasing 10 kN step loads up to 90 kN and (2) the same series of

step loads but returning to 0 before each step. The static tests were done to observe any non-linearity that the 3D printed rail pad may exhibit and to evaluate the signal response from the strain gauge for this type of loading.

## 3.5 FINAL DESIGN

This section provides an overview of the design and fabrication of the final smart rail pad. The section also highlights the laboratory and field testing conducted with the final smart rail pads.

### 3.5.1 Embedding process

The initial design for the final smart rail pad had the connection of the two LIS331 accelerometers together inside the pad. This presented a challenge inside the pad due to limited space for the connection to be made and that if a problem should arise, it could not be addressed because of it being inside the rail pad. The updated design allowed the connection to be made outside the pad where it can easily be repaired if needed. Three cables therefore came out of the rail pad: one for the strain gauge and one for each accelerometer. The accelerometer was changed between the prototype and the final design because the final design required a digital accelerometer to connect two of them on a single $I^2C$ connection for ease of use and simplicity.

The embedding process was similar for both prototypes with only minor additions. Kapton tape was used to keep the shielded wires in place. Kapton tape is a very thin tape which renders well with the 3D printing and the 3D printer could easily print over the tape. This is shown in Figure 3.14 (d). Figure 3.14, (c) and (d) show the instrumentation embedded in smart Pads 1 and 2, respectively. Two identical PETG rail pads were made, one grey (Pad 1) in colour and another one black (Pad 2).
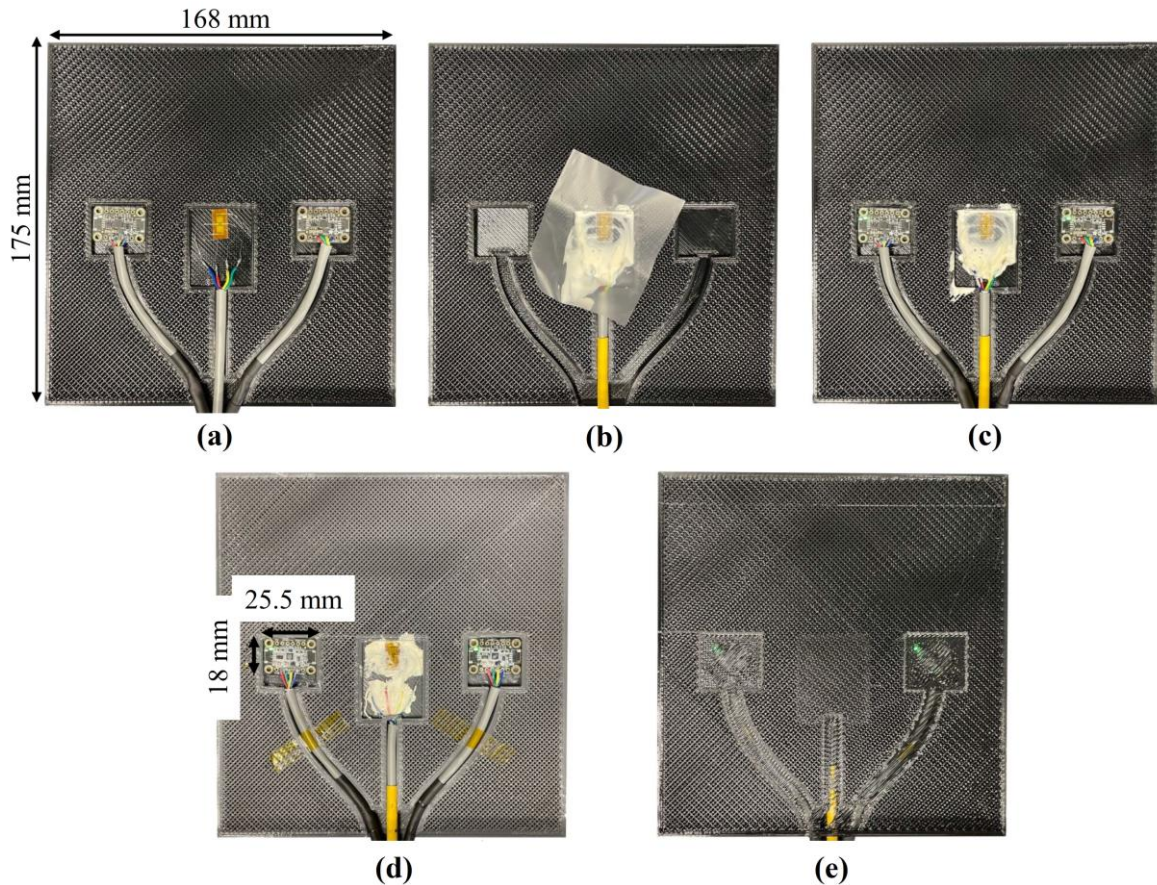
**Figure 3.14: Embedding process for final smart rail pads: (a) two LIS331 accelerometers and the XY-1 strain gauge, (b) glued strain gauge, (c) embedded instrumentation for smart Pad 2, (d) embedded instrumentation for smart Pad 1 and (e) first printed top layer**

### 3.5.2 External measuring enclosure

The external measuring box housed the Razor microcontroller, external strain gauge completion circuit, ADC, and the battery. The measuring enclosure was mounted to the rail with two magnets with a pull strength of 4 kg each. Two plastic pedestals were added to allow the enclosure to be level with the web of the rail. The Razor was fixed to the enclosure with standoffs that lift the Razor 10 mm in the air. This was done to minimise the magnetic interference that could affect the Razor measurements. All external wiring from the smart rail pad to the measuring enclosure is a 4-core shielded cable to mitigate any electrical interference that could cause problems in the field conditions. Logging the data from the instrumentation is indicated by the logging LED. The MCP3424 ADC is a part of the external circuit and converts the voltage signal from the strain gauge into digits. The ADC connects to the Razor through the $I^2C$ interface similar to the accelerometers. The digital address of the ADC can be changed manually by the user through two switches on the top of the ADC. The digital address was

chosen as 0x6E so that it would not interfere with any other instrumentation addresses. The resolution of the ADC can be set to 12, 14, 16, or 18-bit with corresponding sampling rates of 240, 60, 15 and 3.75 Hz, respectively. For the final design, a resolution of 14-bit was chosen to have enough sensitivity, while still sampling at a high enough frequency. A programmable gain amplifier in the ADC allows the amplification of weaker voltage signals. Figure 3.15 displays the final measuring box.
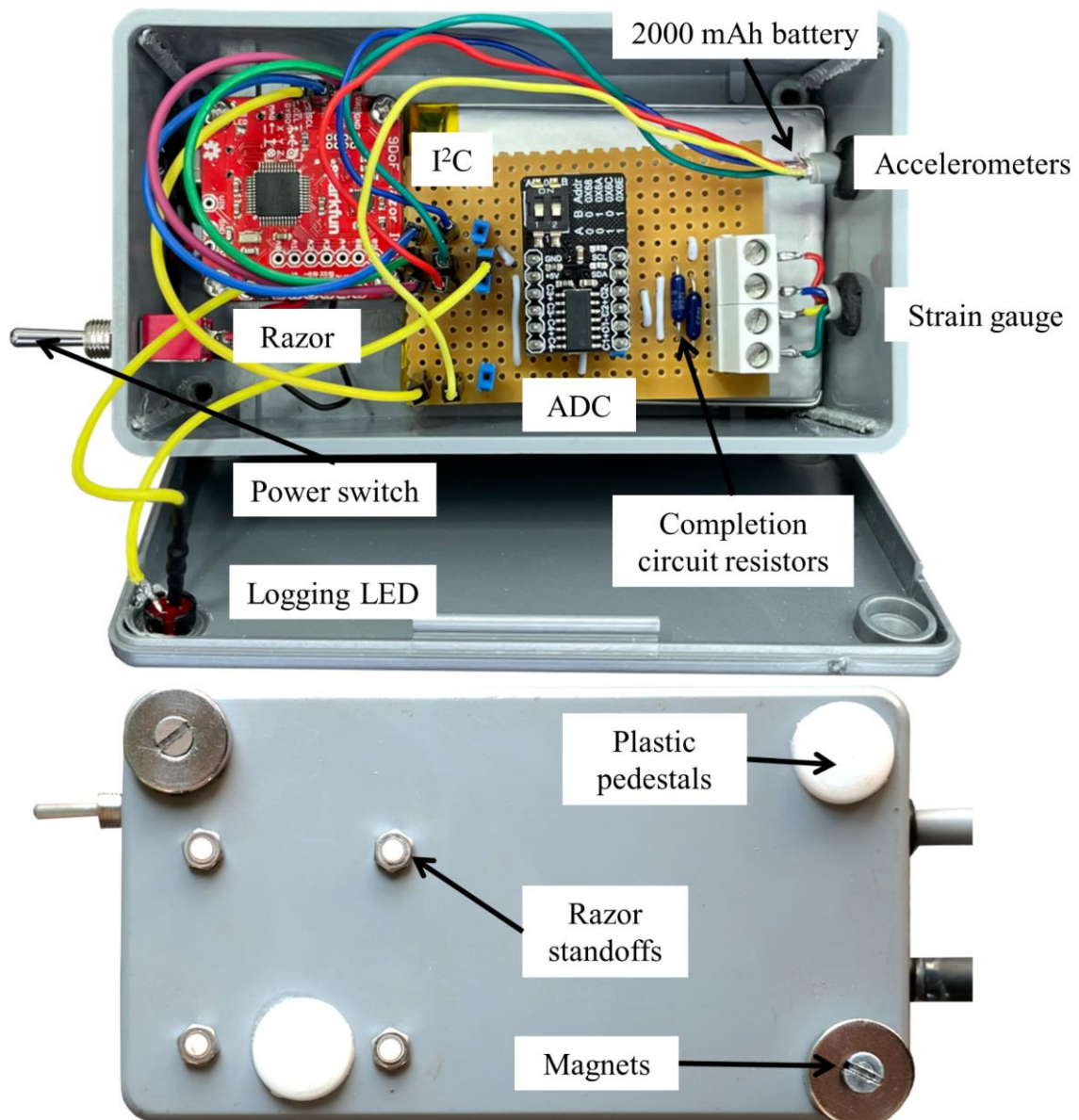


**Figure 3.15: External measuring enclosure top and bottom view**

The final sampling frequency of the smart rail pad was 40 Hz. The low sampling rate is due to two factors; (1) the ADC doing the voltage conversions and (2) the amount of instrumentation and axes that needed to be logged. The low sampling rate is not ideal, but it is still high enough for sufficient information. The Nyquist frequency is half the sampling rate and provides the lower bound at which the sampled data can be reproduced without an error. The minimum sampling frequency must be at least twice that of the highest frequency component present in the signal (Leis, 2011). The highest frequency component of interest, present in the field experiment, was between 8-10 Hz for the axles of the wagons. Theoretically, the sampling rate of 40 Hz is sufficient to sample the signal of the axles.

### 3.5.3 Laboratory testing of smart rail pads

Initial testing in the laboratory included cyclic tests at various frequencies to evaluate the final performance of the smart rail pads before the field experiment. The tested frequencies were 1, 2, 8 and 10 Hz for 60, 60, 500 and 500 cycles, respectively. Figure 3.16 displays a similar test setup.
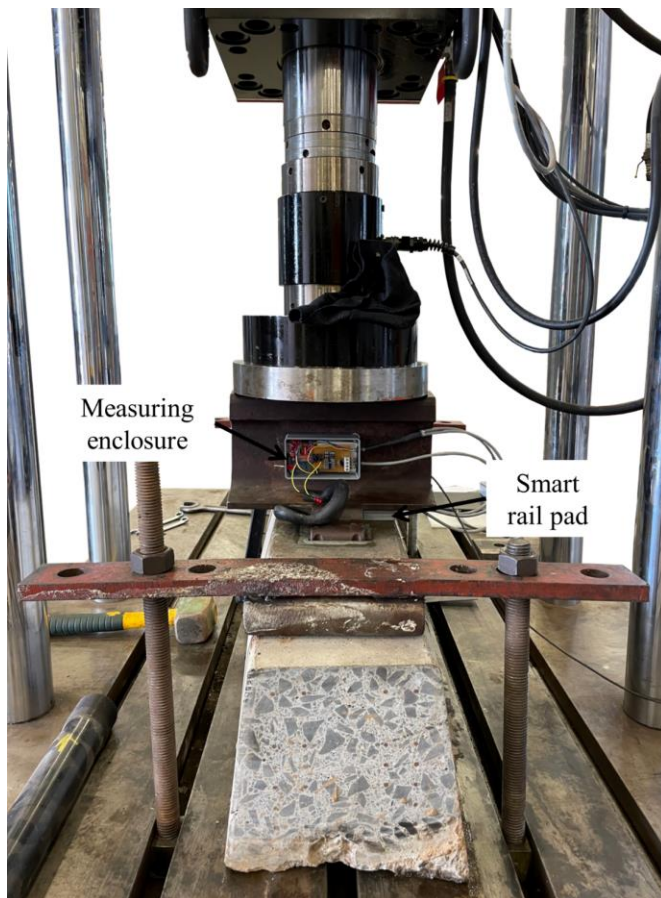


**Figure 3.16: Final design laboratory test setup**

### 3.5.4 Field experiment

The field experiment was conducted between 31 August – 2 September 2021 on the Ermelo-Richards Bay coal line, at the test site called "Bloubank" situated 60 km from Vryheid, KwaZulu-Natal. Details of the specification for the heavy haul coal line is given by Gräbe et al. (2005):

- Track gauge: 1065 mm
- Sleepers: FY concrete
- Axle load: 26 ton/axle
- Sleeper spacing: 650 mm
- Fastening system: Fist fasteners
- Electrified

The field setup was done on Line A of the double line track located at the test site. The loaded trains travel on Line A, running from northwest to southeast (increasing kilometres). The track alignment consisted of a curve with a tangent section, passing the test site, before entering a tunnel. Figure 3.17 shows the locality map of the test site.
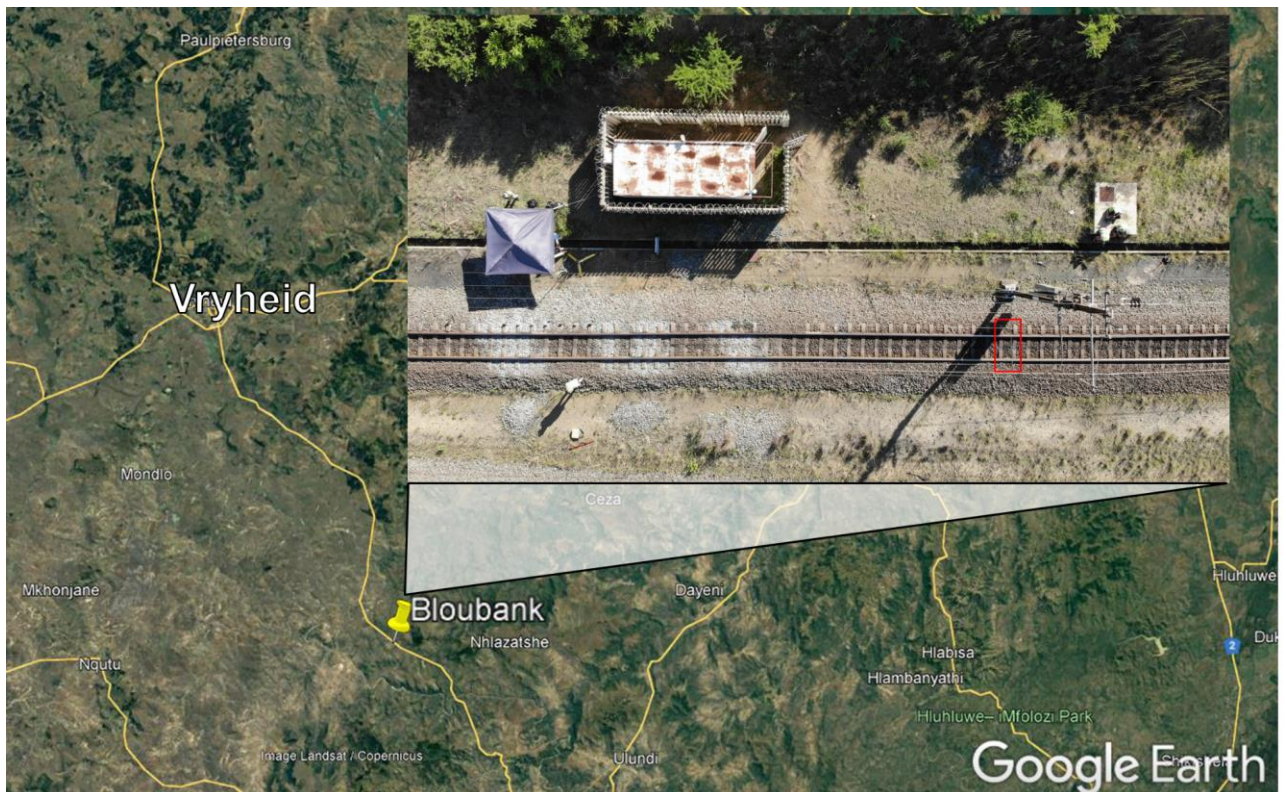


**Figure 3.17: Field experiment locality map (the testing site displayed with the red box)**

The selected section of the track, where the smart rail pads were installed, is displayed and identified with a red rectangle in Figure 3.17. The selected section was chosen because it had a good ballast layer that would not have any excessive deformation as well as be close enough to the container for electricity. The mast pole served as a good infrastructure reference point. The crib ballast, from six sleepers, had to be moved away, three on each side of the chosen sleeper. This had to be done before the Fist fasteners could be removed in order to lift the rail. After the rail was lifted with a hydraulic jack, two smart rail pads were installed on either side of the sleeper. The replacement process is displayed in Figure 3.18



**Figure 3.18: Rail pad replacement: (a) opening made for removing fist fasteners, (b) process of removing fist fasteners, (c) hydraulic jack to lift the rail and (d) the installation of the smart rail pad**

Control measurements were done to validate the performance of the smart rail pads similar to Zhang et al. (2018). Four vertical strain gauges were installed on each rail for wheel load measurements. The rust on the rail was grinded away before the strain gauges were glued to the rail to ensure a clean bond between the two. The strain gauges were glued to the rail with X60.

This process was the same as the process carried out for the installation of the WIM-WIM (Wheel-impact-monitoring) system by TLC Engineering Solutions, on the coal line. The WIM-WIM system is used for wheel impact monitoring and overload detection and can double as an in-motion weighbridge. Five LVDTs were installed to measure pad deflection. Four LVDTs were placed on the chosen sleeper, to validate the pad deflection of the smart rail pads, with another LVDT measuring the pad deflection of a normal HDPE pad. Figure 3.19 displays the installation of the control instrumentation. The LVDTs were mounted to the rail with magnetic rods and was held in place with a steel clamp. The position of the LVDTs were as such that the relative deflection difference between the rail and the sleeper could be measured, which equalled the pad deflection. The measuring enclosure was placed inside a Ziploc bag to protect the magnets from steel fibres and to protect the electronics from moisture. A diagram of the experimental setup and an image of a passing train over the setup, can be seen in Figure 3.20 and Figure 3.21.
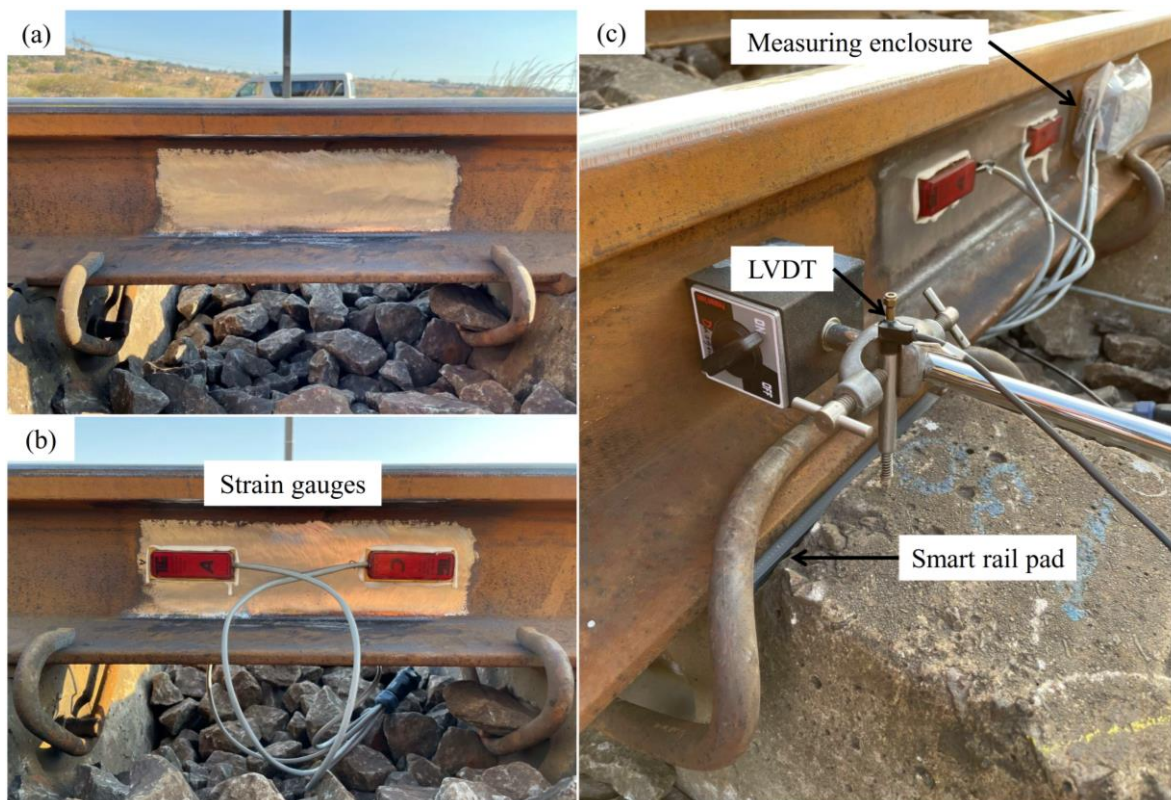


**Figure 3.19: Installation of control instrumentation: (a) grinded rail, (b) glued strain gauges and (c) LVDT clamped onto the magnetic rod**
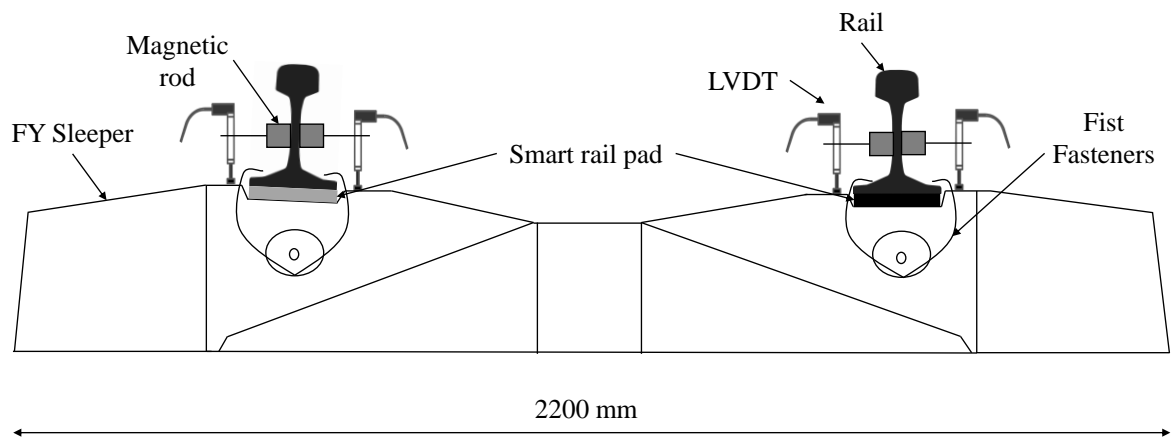
**Figure 3.20: Cross-section diagram of the field test setup**



**Figure 3.21: Train 3 travelling past the experimental field setup**

Six trains in total, were logged with both the smart rail pads and the control instrumentation. Various locomotive and wagon types were captured. Table 3.5 shows the train list and related information. The smart rail pads were left overnight to test the automatic triggering and the battery life of the system. The maximum runtime of the system was 42 hours with a 2000 mAh battery while logging all the instrumentation, which was sufficient for short-term testing. The automatic triggering allowed the rail pads to respectively measure six trains during the night. This provided evidence of the effectiveness of the automatic triggering of the Razor to log the data from the instrumentation inside the smart rail pad. The automatic triggering allowed for continuous condition monitoring of the train wheels.

**Table 3.5: Train list and information**

| Train no. | Amount | | Time of day | Type | | Notes |
|---|---|---|---|---|---|---|
| | Locomotives | Wagons | | Locomotive | Wagon | |
| 1 | 6 | 200 | 11:21 | 21E | Coal | No data for smart rail pad 1 |
| 2 | 6 | 200 | 11:43 | 21E | Coal | instrumentation logging |
| 3 | 2 | 120 | 12:05 | 22E | Wood | LVDT added for real HDPE pad |
| 4 | 6 | 200 | 14:41 | 21E | Coal | All instrumentation logging |
| 5 | 2 | 50 | 16:32 | 22E | General freight | Only accelerometers logging in smart pads |
| 6 | 6 | 200 | 17:16 | 19E | Coal | All instrumentation logging |
| 7 | 5 | 98 | 09:00 | 22E | Coal | Both smart rail pads logging |

## 3.6 TYPICAL RESULTS

This section displays the typical response of the smart rail pad and the data outputs versus time. An example of the accelerations versus time of the 10 Hz test from the accelerometer prototype, is given in Figure 3.22. A comparison between the LVDT and the displacements integrated from the accelerations of the accelerometer prototype, is shown in Figure 3.23. An example of the

strain gauge voltage versus time is given in Figure 3.24. An example of an accelerometer and strain gauge output versus time, of the smart rail pad in the field, is shown in Figure 3.25.
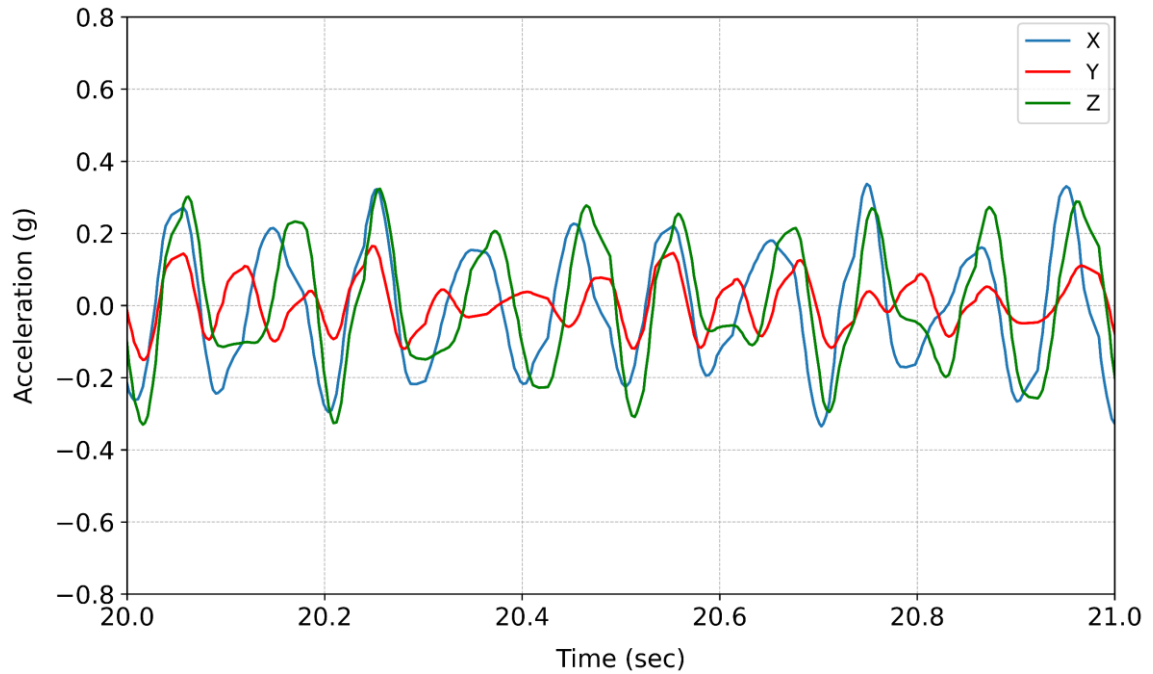


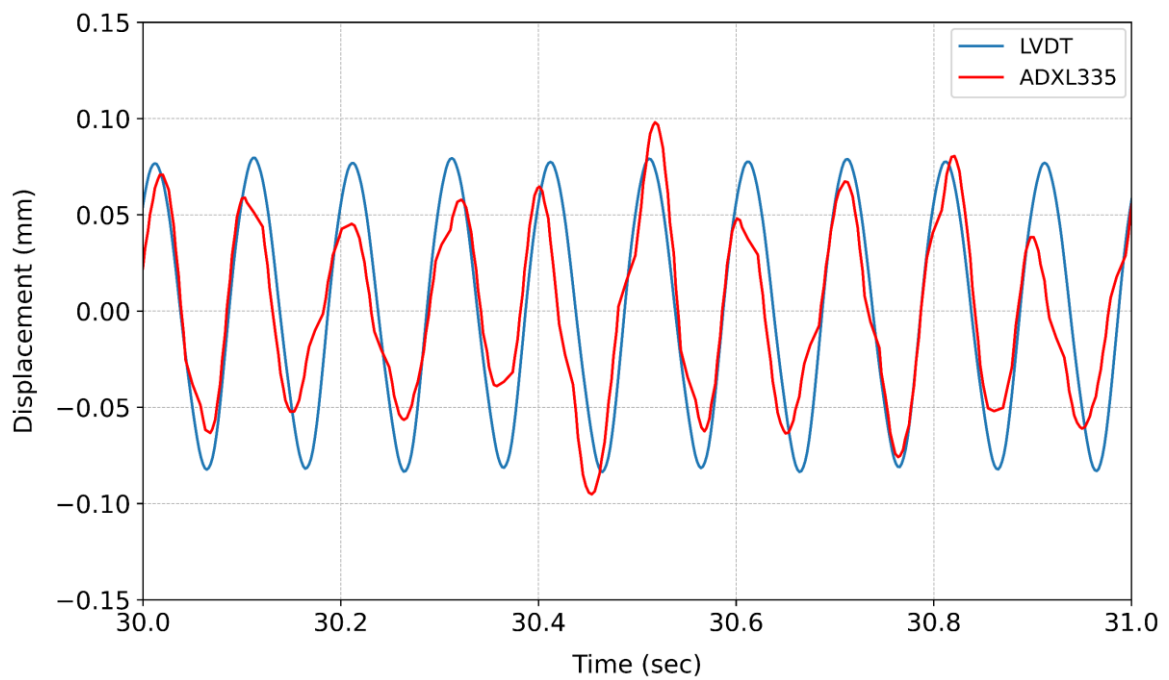**Figure 3.22: Acceleration: All axes of ADXL335 (10 Hz - Accelerometer prototype)**



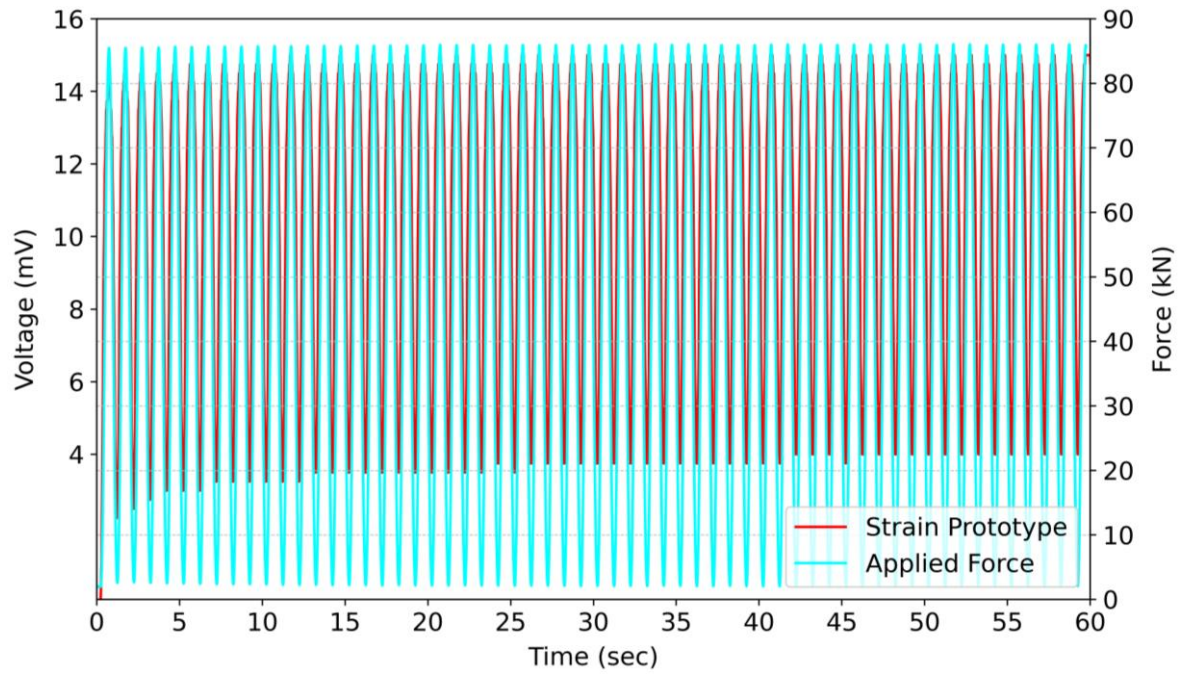**Figure 3.23: Displacement: LVDT compared to integrated displacements (10 Hz)**

**Figure 3.24: Voltage output from strain prototype under 1 Hz loading of 86 kN**
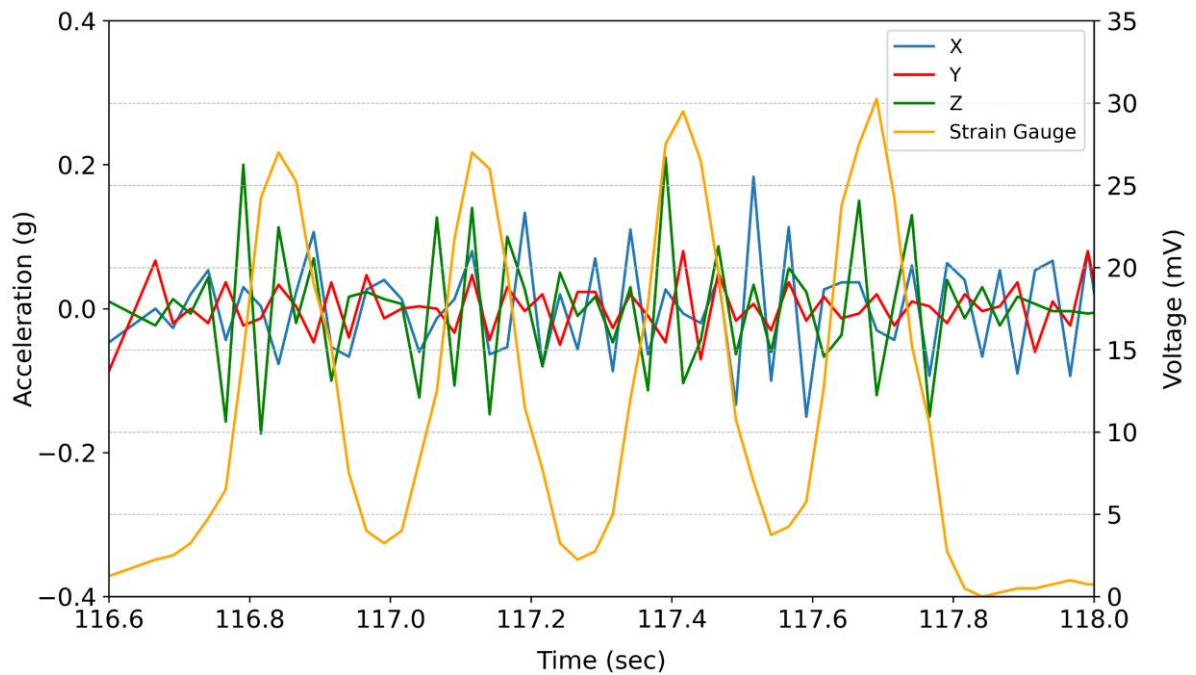


**Figure 3.25: Accelerometer 1 and strain gauge output for a deflection bowl in Train 04**

# 4 ANALYSIS AND DISCUSSION

The analysis and discussion of the experimental results of the 3D printed rail pad testing and acceleration and loading data, are discussed in this chapter. The chapter is divided into three sections, namely: 3D printed rail pad results, prototype testing results, instrumented (smart) rail pad laboratory and the field results. The first section discusses material testing and evaluates the ability of a 3D printed rail pad to withstand the typical forces exerted on a railway line. The second section discusses the testing of the two prototypes. The third section analyses the performance of a smart rail pad in the laboratory and the field.

## 4.1 MATERIAL TESTING

Material testing was conducted on all three filament types to determine which would be best suited for fabricating a rail pad. Four different infill percentages were tested namely: 25 %, 50 %, 75 % and 100 %. Tensile and compressive strength tests were done following the ASTM standards for plastics. No compressive strength tests were conducted on TPU as no standard was found for non-rigid plastics. The mechanical properties of plastics, in general, are sensitive to the rate of deformation (strain rate) and temperature (Callister & Rethwisch, 2015).

### 4.1.1 Tensile Strength Tests

Tensile strength tests were conducted according to the ASTM D638 standard (ASTM, 2014). The tensile elastic modulus and yield strength were calculated from the results from each test. The elastic modulus is the ratio of stress to strain below the yield point of the material. The elastic modulus was calculated by determining the slope of the elastic (linear) region of the stress-strain curve. Figure 4.1 displays the elastic modulus calculated from the tensile strength tests for PETG, PLA and TPU. The elastic modulus of PETG and PLA is in the units GPa where TPU is in MPa.

The average yield force for the 100 % specimens of PETG, PLA and TPU was 1.66 kN, 2.03 kN and 0.66 kN, respectively. The average results for tensile strength and elastic modulus of 31.3 MPa and 5.2 GPa for PLA (100 %) are similar to those found by Farah et al. (2016) and Johnson & French (2018). The results for the tensile strength of TPU agree with Wang et al. (2020) and Lee et al. (2019). The tensile strength of 25.6 MPa for 100 % infill of PETG correlates well with Srinivasan et al. (2020). The results showed that PLA is stronger and more rigid than PETG, while PETG still has a relatively high tensile strength. Figure 4.2 illustrates the typical stress-strain curve of PETG, PLA and TPU.
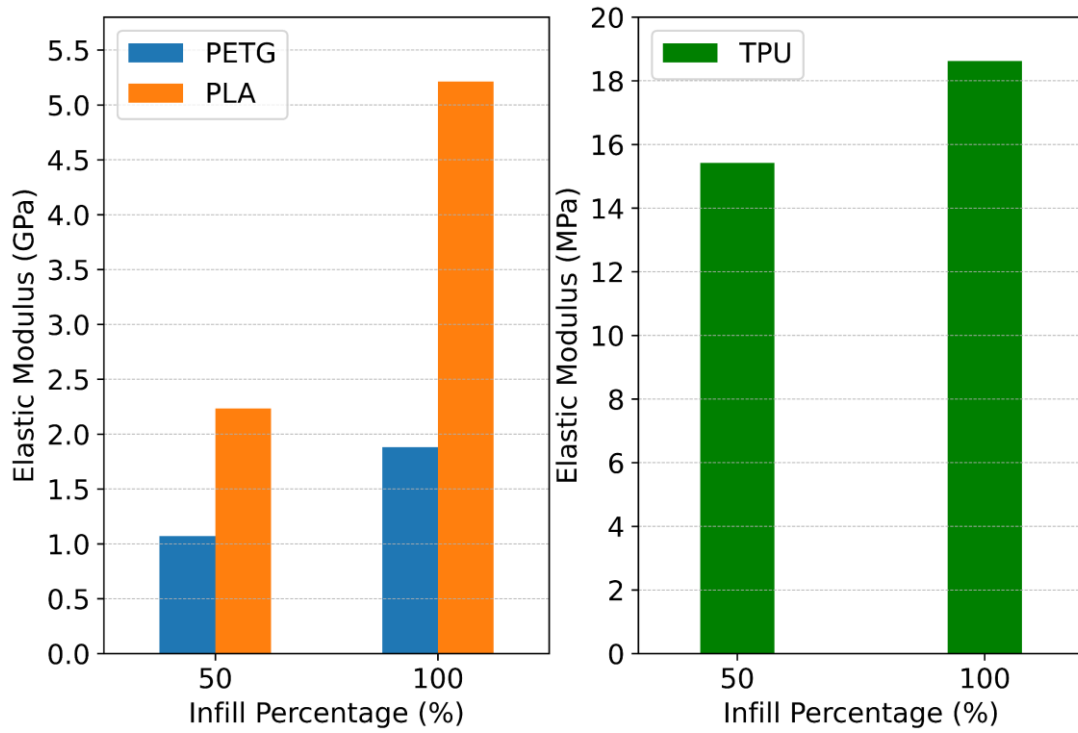
**Figure 4.1: Tensile Elastic Modulus for PETG, PLA and TPU**
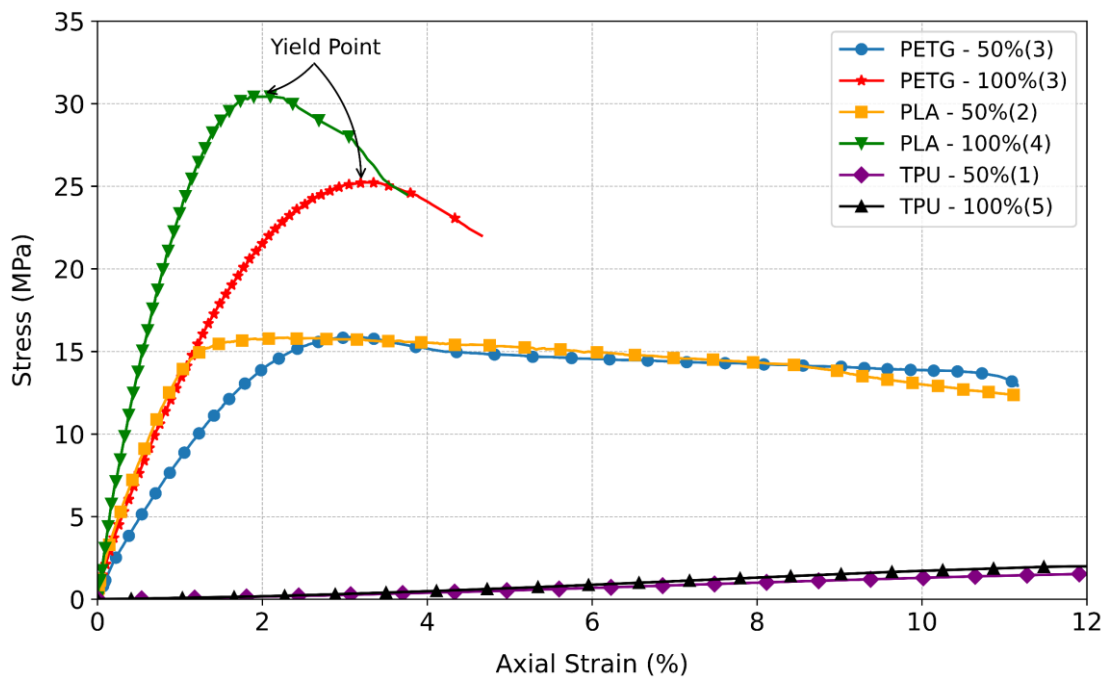


**Figure 4.2: Stress-strain curve of PETG, PLA and TPU under tensile loading**

The stress-strain behaviour for PETG and PLA is the same as that of some metals where the initial deformation is elastic, followed by the yielding of the material and a region of plastic deformation (Callister & Rethwisch, 2015). For PETG and PLA, the yield point is taken as the maximum on the curve just past the end of the linear-elastic region. The yield strength is the stress at the maximum peak of the curve. TPU displays elastic behaviour that has large recoverable strains at low-stress levels, common in elastomers (Callister & Rethwisch, 2015). The 50 % infill specimens were closer to each other in terms of yield strength whereas the 100 % PLA was stronger than the PETG specimen. The stress-strain behaviour, in Figure 4.2, of the 50 % infill specimens for both PETG and PLA, show the increase in strain for the same stress levels, illustrating the ductile behaviour that can take place in the plastic region. Figure 4.3 displays a typical brittle and ductile fracture for PETG and PLA. Figure 4.4 displays two different fractures seen in the TPU specimens.



**Figure 4.3: Typical brittle and ductile fracture for PETG (Black) and PLA (Grey) specimens**
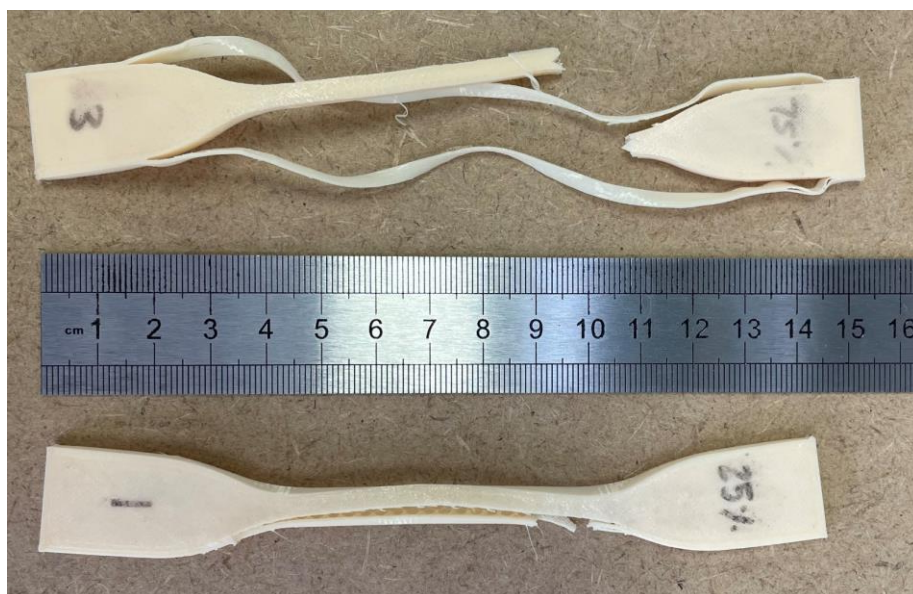
**Figure 4.4: Two different fractures for the TPU specimens**

The 100 % infill PLA specimen shows how the plastic fractures in a brittle manner as is shown in Figure 4.3. In Figure 4.4, the 75 % infill specimen simply fractured at one place whereas the 25 % infill specimen split open on one side of the specimen. The TPU specimens had an initial length of 115 mm and Figure 4.4 shows the permanent deformation that occurred when the TPU was stretched well past the elastic region.

### 4.1.2 Compressive Strength Tests

Compressive strength tests were conducted according to the ASTM D695 standard (ASTM, 2015). The compressive elastic modulus and yield strength were calculated from the results of each test. The compressive strength of the material is more applicable due to the type of loading experienced by rail pads. The information from the compressive strength test provides a good indication of whether PLA or PETG can function as a rail pad material. The average yield force for the 100 % infill specimens of PETG and PLA were 6.80 kN and 9.12 kN, respectively. Figure 4.5 displays the calculated elastic modulus from the compressive strength tests for PETG and PLA. The elastic modulus is similar for the two filaments with PLA having a higher modulus than PETG as expected. The compressive elastic modulus is less than the tensile elastic modulus suggesting that the slope of the linear-elastic region in tension is steeper than the linear-elastic slope in compression. Another reason for the difference could be the different types of specimen shapes and the rate of loading on the material in the tests. Figure 4.6 displays the stress-strain curve for PETG and PLA under a compressive load.

**Figure 4.5: Elastic Modulus for PETG and PLA**



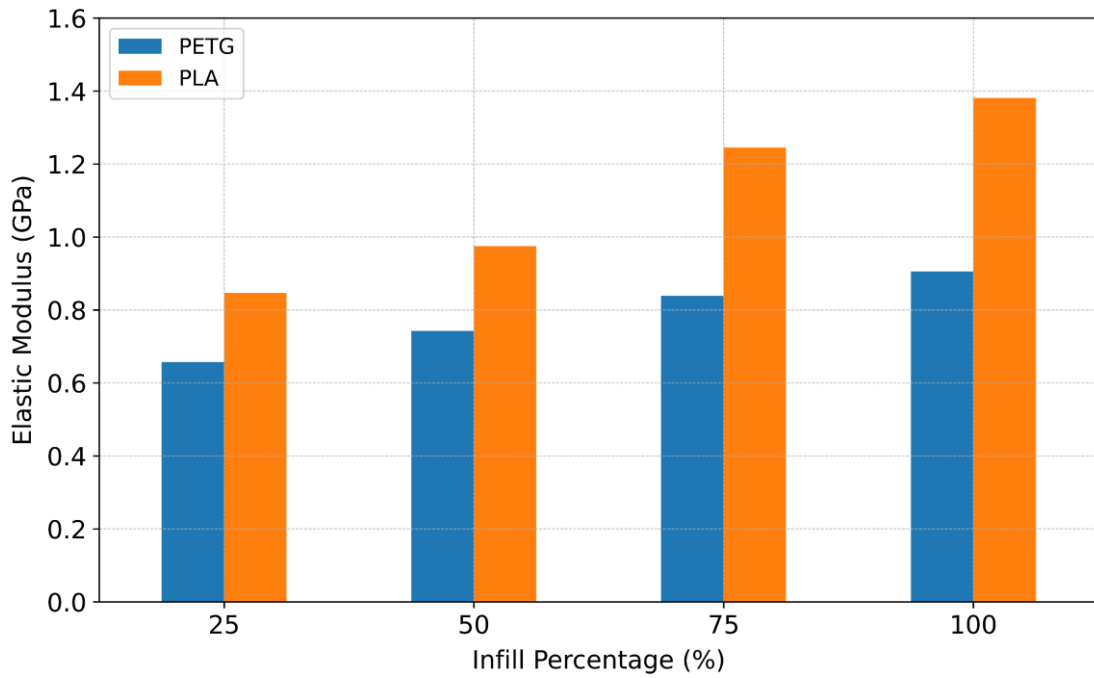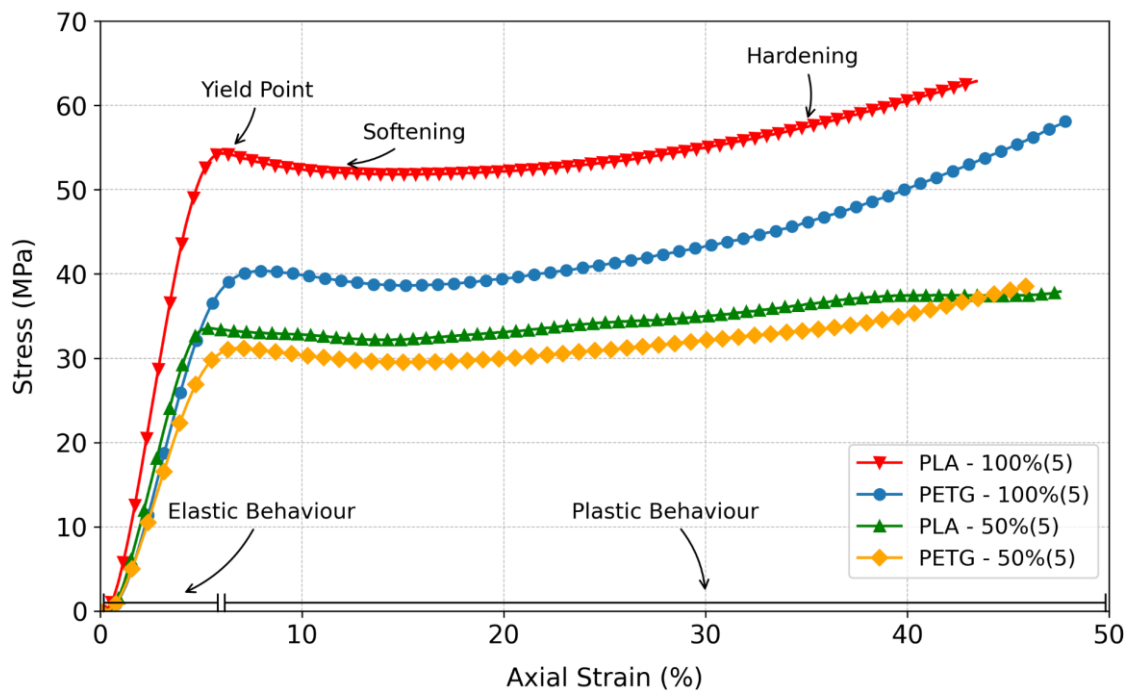**Figure 4.6: Stress-strain curve of PETG and PLA under compressive loading**

The yield force and yield strength are calculated at the yield point where the material deforms past the elastic region and into the plastic region, shown in Figure 4.6. A rail pad is an elastic

track component and thus only the elastic region before the yield point is considered for calculations. PLA has a higher yield strength than PETG, however, PETG is more elastic and can therefore have more recoverable deformation before the yield point is reached. This is expected, as PLA is slightly more brittle than PETG. The linear slope for the elastic modulus of PLA is steeper than PETG, as illustrated in Figure 4.6. The stress-strain curve has the same regions, as mentioned before, with the linear-elastic region up to the yield point, followed by softening and hardening of the material. The 50 % infill specimens also have similar yield strengths whereas the 100% infill had a higher difference with PLA being stronger than the PETG specimen. Figure 4.7 displays a PLA specimen during the test and a PETG and PLA specimen after the test.
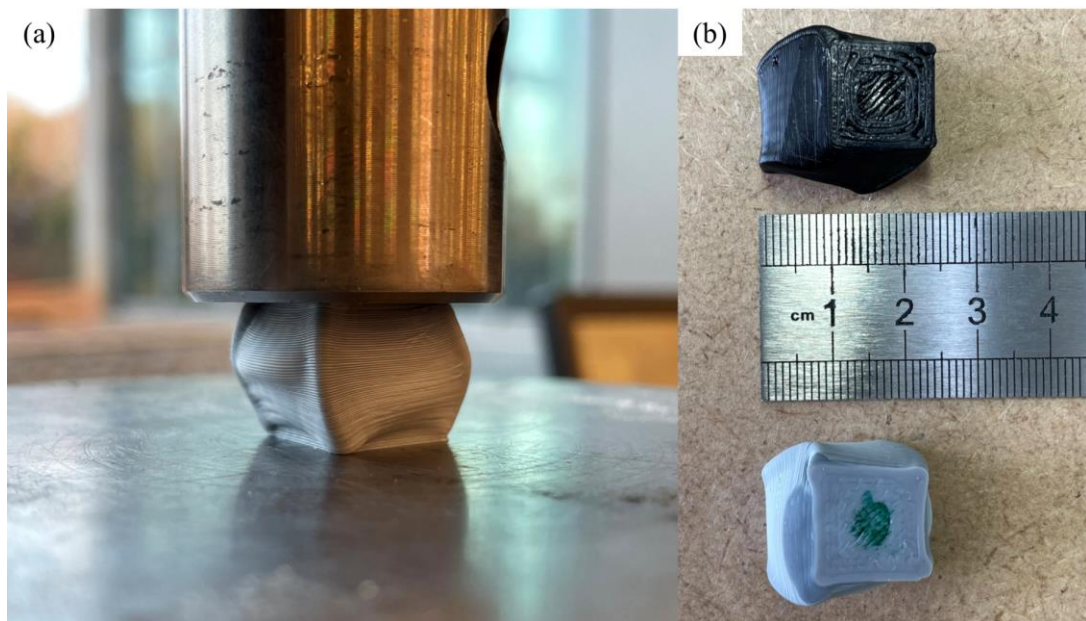


**Figure 4.7: Compression test specimens (a) during and (b) after the test**

The specimen in Figure 4.7 (a) is beyond the elastic region and has permanently deformed. Some twisting can be seen from the specimen during and after the test. Barrelling of the sides of the specimen is a common failure mode of the specimens. These tests were important in the decision on which 3D printing material would be the best suited for making a rail pad. The results provided insight into how the various 3D printing materials behave and deform. The results showed that PETG, although softer than PLA, had a high enough compressive strength that it could be used to fabricate a rail pad. The results proved that the strength of the material increased as the infill percentage increased.

## 4.2    3D PRINTED RAIL PAD

The material testing which was conducted to determine whether 3D printed material can be used to create a rail pad with appropriate strength and stiffness properties is discussed in this section. Static and cyclic loading was applied to the three 3D printed rail pads to ascertain whether the 3D printed rail pads could sustain the typical forces exerted on a rail pad without excessive plastic deformation. Five rail pads were tested with static and cyclic loading, two of which were control rail pads and three 3D printed rail pads. The control rail pads were the HDPE pad (hard) and the Hytrel pad (soft).

### 4.2.1    Static Stiffness

Static loading tests were done before and after the cyclic loading and five separate tests there-after to determine the static pad stiffness. The five static loading tests were conducted to mitigate any bedding effects on the results that can occur in the initiation of the loading test. The static stiffness for each test was calculated using Equation 3.3. Figure 4.8 displays the results of the five separate static stiffness tests on the five rail pads.
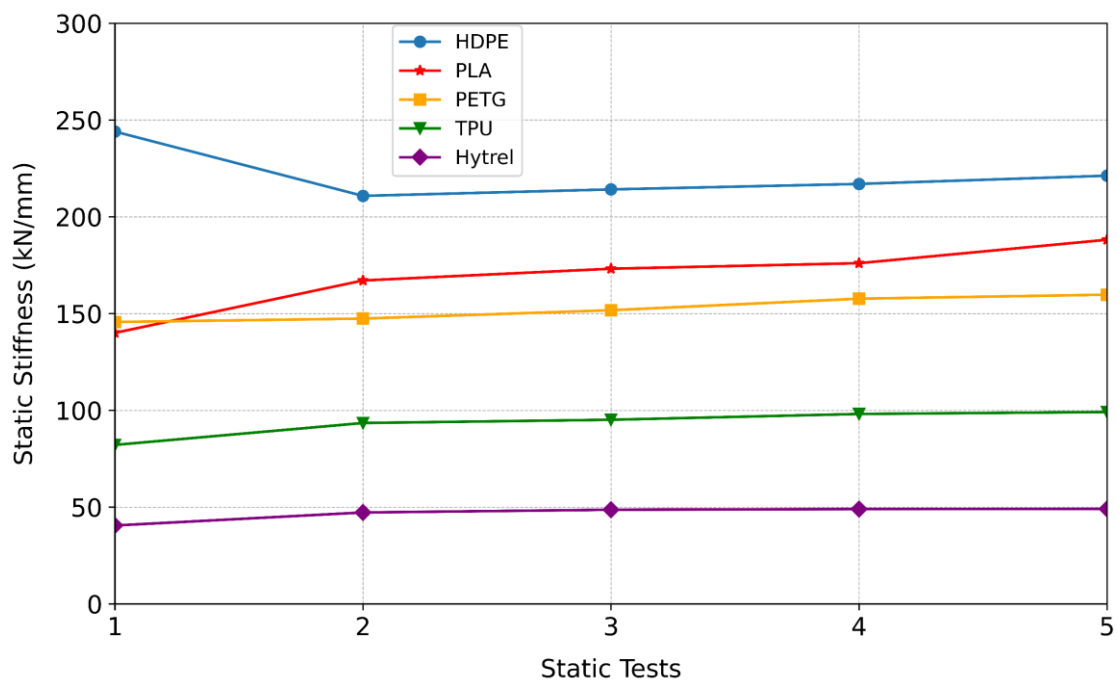


**Figure 4.8: Static stiffness across five static tests of each rail pad**

The static stiffness increases somewhat in each test and illustrates how the rail pads stiffen as they are loaded. The initial increase from Test 1 to 2, is the highest in stiffness for PLA, TPU

and the Hytrel pad. HDPE has an initial decrease in stiffness whereafter it increases again. The results of the three 3D printed rail pads were located between the two control rail pads. PETG is situated in the middle and has a good consistency in its static stiffness.

Figure 4.9 shows the loading and unloading of the rail pads in the static test at the end of the 500,000 cycles. All the rail pads, except TPU, had an elastic loading and unloading curve, where the start and the end of the curve were at the same place, suggesting there is no plastic deformation. The opposite is true for TPU, which has plastic deformation where the unloading path ends with 0.56 mm of permanent deformation. There was minor hysteresis for PETG, PLA and HDPE. The TPU pad exhibited the greatest extent of hysteresis for an elastic loading and unloading curve. Hysteresis, the divergence of the two paths, shows the amount of energy loss in the form of heat between the two loading phases.
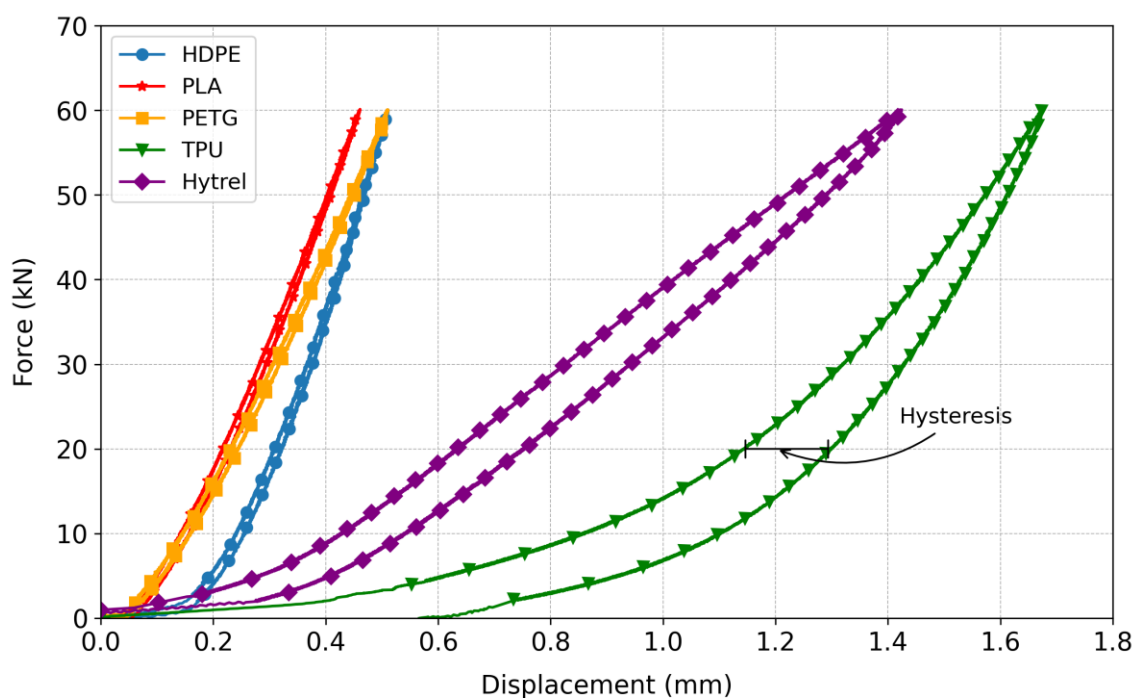


**Figure 4.9: Loading and unloading curves for each tested rail pad**

### 4.2.2 Dynamic Stiffness

Dynamic testing was done on all five rail pads over 500,000 cycles at 25 Hz. The main purpose of the dynamic material testing was to determine whether a 3D printed rail pad can sustain the typical forces that a real rail pad experiences without excessive plastic deformation. The dynamic stiffness for each pad was calculated using Equation 3.2. The dynamic stiffness of the

first 1000 cycles of every 100,000 cycles was calculated, as well as that of the last 1000 cycles at the end of the test. The dynamic stiffness of each rail pad is displayed in Figure 4.10. The dynamic stiffness rapidly increased for each rail pad as the cycles increased. The rail pads stiffen and harden to an extent as loads were applied to it. There is an aspect of non-linearity in the behaviour of the rail pad under loading. The results of the dynamic stiffness of the three 3D printed rail pads are located between the two control pads. PLA is stronger and stiffer than PETG. A requirement for a 3D printed rail pad was that it needed to provide support for the internal instrumentation, while still providing the elasticity of a rail pad. The natural first choice would have been PLA because it is the strongest of the three filaments. However, PETG is strong enough to support the internal instrumentation and provide some elasticity when in the form of a rail pad.
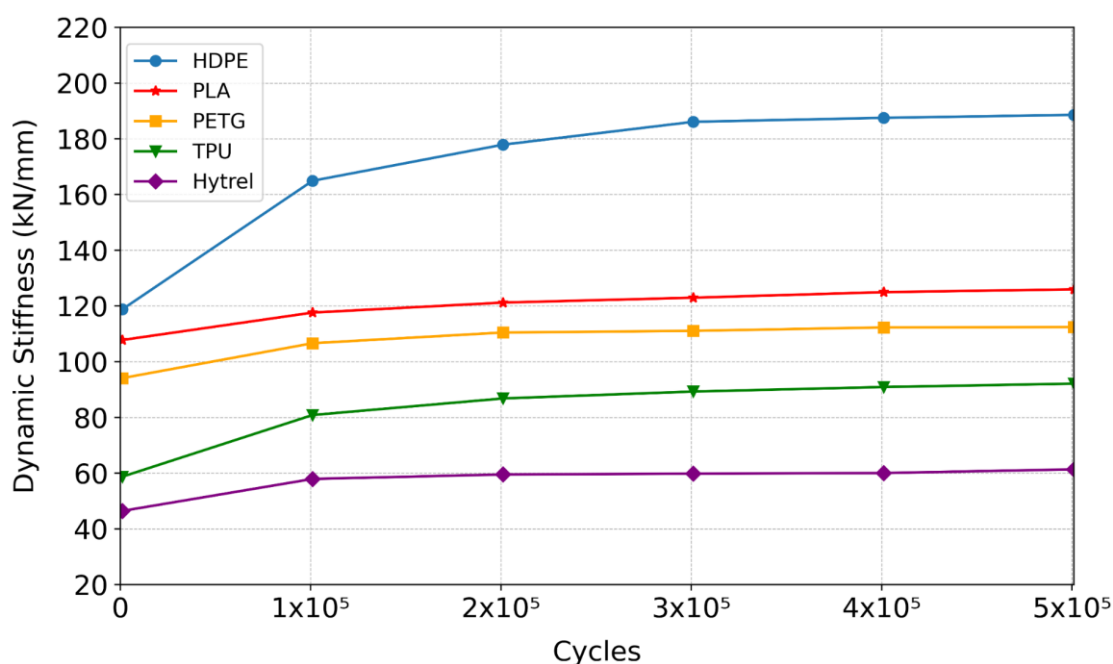


**Figure 4.10: Dynamic stiffness of each rail pad during 500,000 loading cycles**

Initially, TPU was expected to be the best filament for fabricating a rail pad because it could provide the highest elasticity of the three filaments. However, after the 500,000 cycles, the TPU rail pad had permanently deformed and any internal instrumentation would have been damaged, as displayed in Figure 4.11. Another reason TPU would not have been effective was that it took 40+ hours to print a TPU rail pad. The TPU pad deformed elastically when it was bent or compressed, however, after the 500,000 cyclic loads the TPU pad deformed permanently. The

permanent footprint left by the rail section can be seen in Figure 4.11 (c). Any instrument inside would have been damaged and thus the TPU filament could not be used as a rail pad.
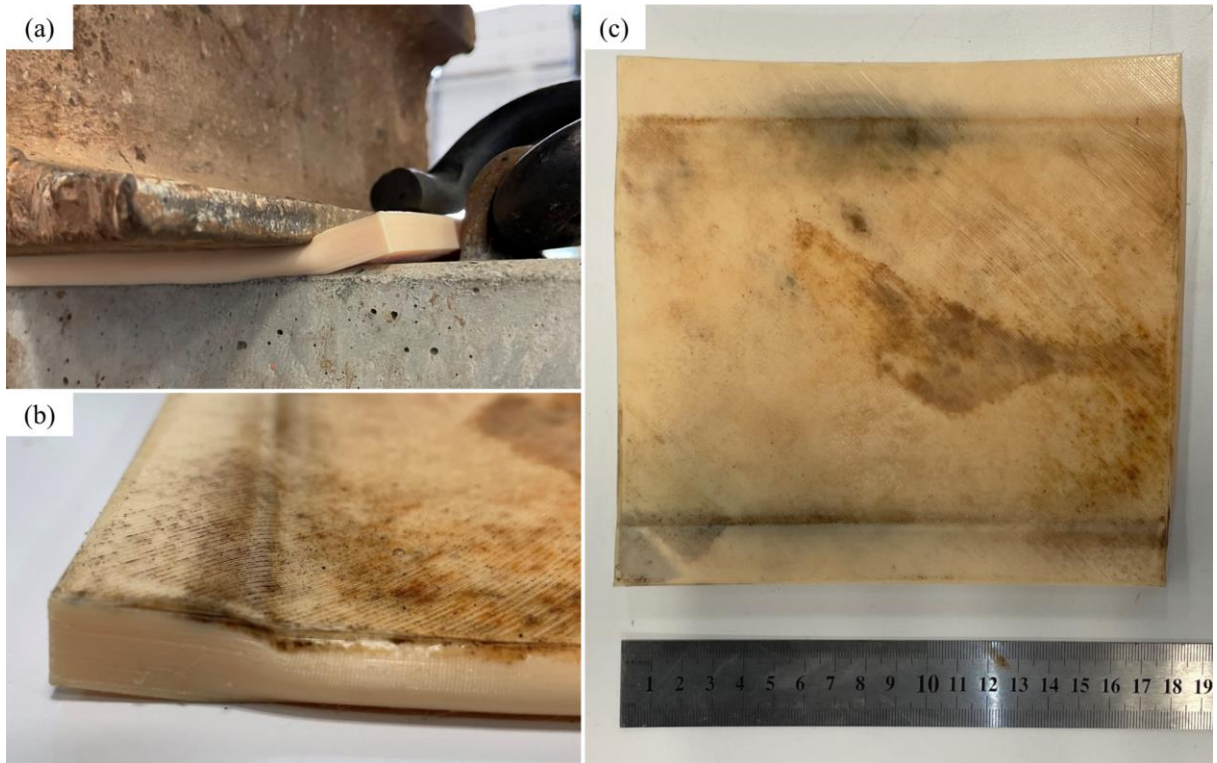


**Figure 4.11: TPU rail pad after 500,000 cycles. (a) During the test, (b) close-up of the rail pad and (c) the deformed rail pad**

The PLA and PETG rail pads performed well under the cyclic loading and no permanent deformation occurred, as shown in Figure 4.12. Merely some minor scratches and dust from the rail section were left on the surface. PETG and PLA showed that it can provide sufficient support for internal instrumentation and that it will not permanently deform under cyclic loading. The decision on which filament to use for the 3D printed smart rail pad was between PETG and PLA. The decision was made to use PETG because of its strength to protect internal instrumentation while providing elasticity to the track structure. It also has a greater glass transition temperature, meaning that it will perform better in hot climates and not deform due to high temperature, compared to PLA.

**Figure 4.12: PETG (red) and PLA (grey) rail pads after 500,000 cycles**

## 4.3 PROTOTYPE TESTING

Static and dynamic testing was conducted on the two prototypes. Initial prototyping served as trial-and-error testing of a smart rail pad. Descriptive statistics were used to compare measurements from the different instruments with the control instruments. The peak-to-peak amplitude was the main parameter of interest for the cyclic loading.

### 4.3.1 Accelerometer Prototype

The accelerometer prototype housed an ADXL335 accelerometer and was logged with an Arduino Mega. The calibration of the accelerometer is given in Appendix A. The cyclic testing consisted of 1000 cycles at various frequencies to simulate trains and axles travelling at different speeds. A Fast Fourier Transform (FFT) analysis produced the average frequency content of a signal over the entire measurement period (Cerna & Harvey, 2000). The FFT of each test was calculated to determine and isolate the test frequencies. The results from the FFT show each of the tested frequencies as well as other external frequencies that influenced the data as shown in Figure 4.13.
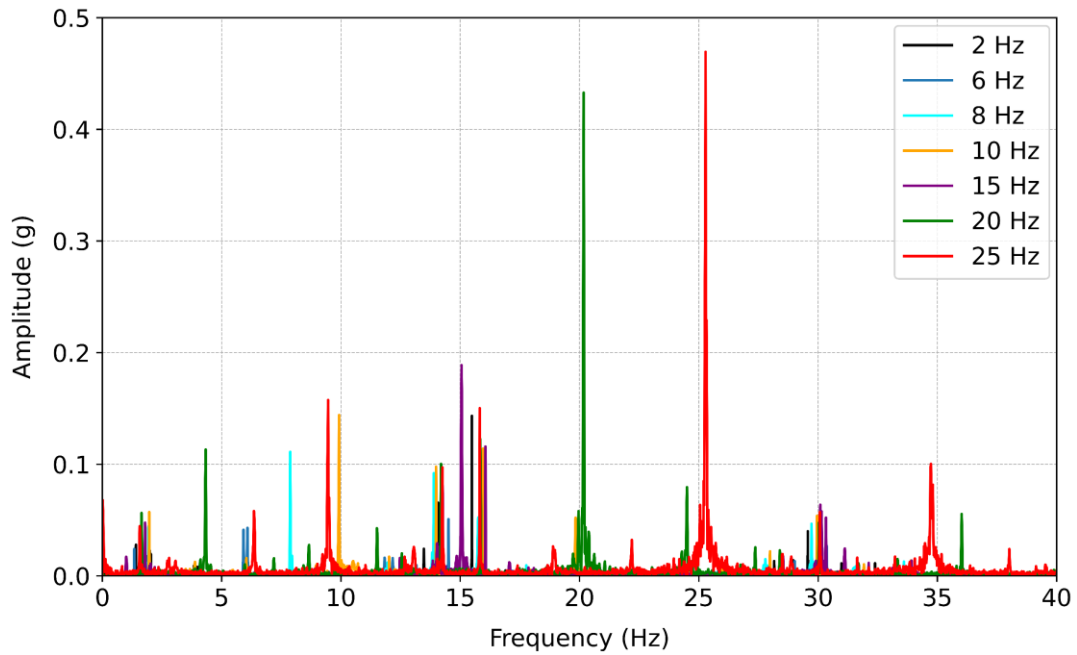
**Figure 4.13: FFT of the tested frequencies**

The peak for each frequency from 8 - 25 Hz is visible in the FFT analysis. The peaks of 2 Hz and 6 Hz are over-shadowed by a frequency at 15.8 Hz when plotted separately. The same peak at 15.8 Hz can be seen in every tested frequency, which suggests that there was an external frequency that was measured by the accelerometer. A cluster of frequencies exist around 15 Hz. The source of this frequency is unknown; however, it is suspected to be associated with the MTS or Arduino.

An LVDT was used as the control measurement to verify the displacements obtained from the double integrated accelerations of the accelerometer. The comparison was done to ascertain whether the accelerometer can accurately determine the pad deflection. Pre-processing of each tested frequency was done before analysing the data. The accelerations of the tested frequencies: 1, 2, 6, 8, 10, 15, 20 and 25 Hz were filtered with a 4th order bandpass Butterworth filter around each frequency magnitude. Thereafter, the filtered accelerations were integrated twice, using the trapezoidal rule, to calculate displacements with a first-order trend removal at the end of the process to compensate for the cumulative nature of the integration.

The descriptive statistics related to the mean, standard deviation, minimum and maximum are evaluated and compared for the LVDT and the accelerometer prototype. Any outliers, for both the minimum and maximum measurements, were removed before peak detection. The peak detection method used identifies a maximum point when it has a maximal value and was preceded (to the left) by a value lower than the threshold value (Billauer, 2010).

The method suggested by Billauer (2010) was deployed in Python and is derived from a MATLAB program. Each frequency was tested with 1000 cycles on the MTS. The peak detection method identifies as many of the peaks as possible to create a large enough sample size for each test. Figure 4.14 displays the mean displacement difference between the LVDT and the accelerometer data across the tested frequencies. To compare the results, the mean peak-to-peak displacement was calculated to provide an average characteristic displacement for each instrument (Milne et al., 2016). The frequencies of 1 Hz and 2 Hz are omitted because the mean, maximum and standard deviation values, for each, are too large to display with the other values. The peak-to-peak mean difference between the accelerometer and the LVDT was 4.42 mm and 0.91 mm, for 1 Hz and 2 Hz respectively. Considerably small accelerations were measured for the frequencies of 1 Hz and 2 Hz. It was noted by Milne et al. (2016) that this is a performance limitation of the sensor. To this end, the displacements were overestimated by the integration of the small accelerations resulting in unrealistic displacements. This must be considered since it could limit the detection of minor track variations and only be suitable for significant changes in track performance such as hanging sleepers and high-impact wheel flats (Sol-Sánchez et al., 2021b).
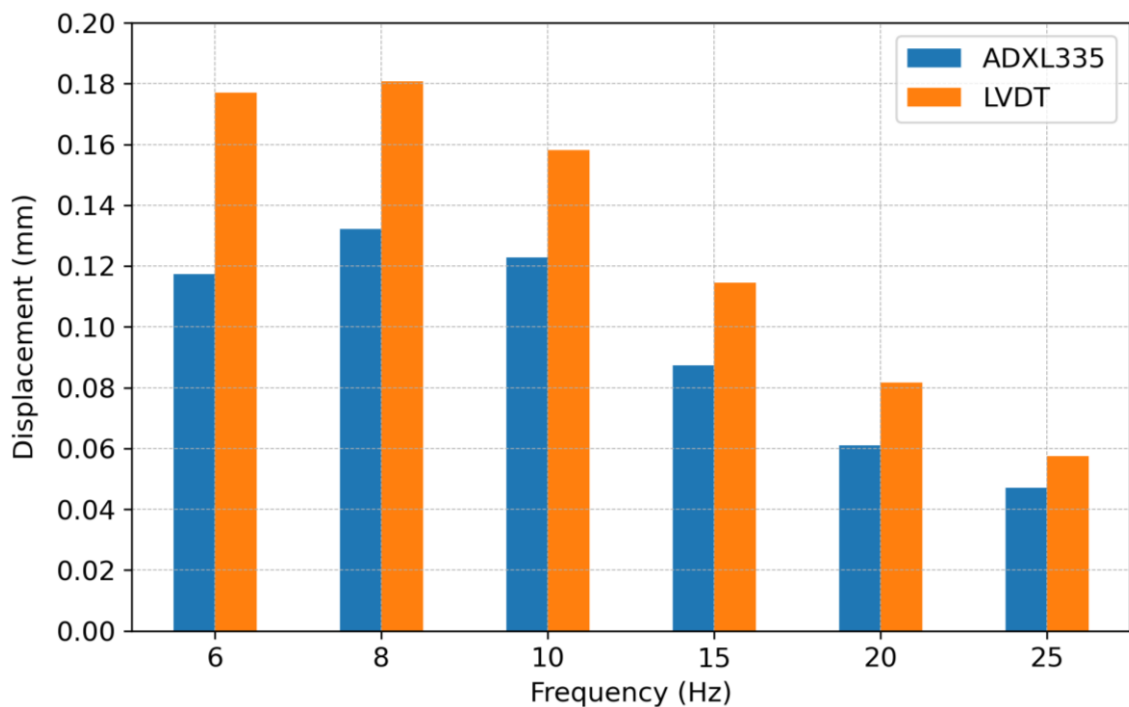


**Figure 4.14: Mean peak-to-peak displacements from the accelerometer and LVDT**

The rail pad deflection was underestimated across all frequencies by the integrated displacements from the accelerometer data when compared to the LVDT measurements. The degree of underestimation decreases as the frequency increases, which agrees with that of Milne et al. (2016). This is in part due to the large standard deviation of the integrated displacements that decreases the mean value. The mean difference between the two decreases as the frequency increases. As the frequency increases, the magnitude of the displacements decreases, for both instruments. Figure 4.15 displays the maximum displacements between the LVDT and the accelerometer.
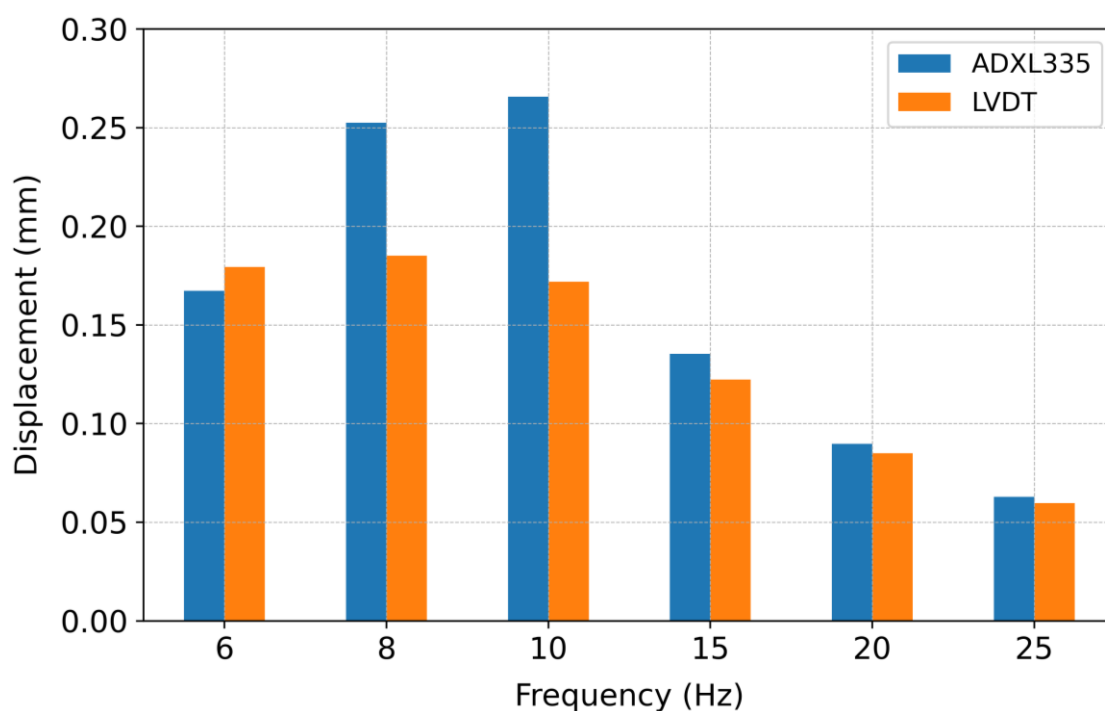


**Figure 4.15: Maximum peak-to-peak displacements from the accelerometer and LVDT**

The maximum displacements for 8 Hz and 10 Hz are considerably larger for the accelerometer than for the LVDT. The maximum displacements from the two instruments were in reasonably close agreement with small differences noted at the higher frequencies. This implies that the accuracy of displacement measurement increases as the frequency increases. The same observation can be seen where the magnitude of the displacement decreases, as the frequency increases. The LVDT results showed less variation, with a relative standard deviation of 2 % compared to 21 % for the accelerometer, as illustrated in Figure 4.16. Figure 4.16 clearly illustrates the variation in displacement results from the accelerometer and the LVDT. The variation in the displacement decreases as the frequency increases, similar to the mean peak-to-

peak displacement differences. Displacements can successfully be acquired from the acceleration data obtained from the accelerometer prototype, especially at frequencies higher than 6 Hz.



**Figure 4.16: Box and whisker plot for the LVDT (left) and the accelerometer (right)**

### 4.3.2   Strain Prototype

The strain prototype testing was done to determine whether any strain can be measured from the strain gauge in the middle of the rail pad. The output from the strain gauge was measured with the Razor microcontroller and an HBM acquisition system, to verify that the complete circuit and strain gauge was working as expected. Short cyclic tests and two static tests were conducted.
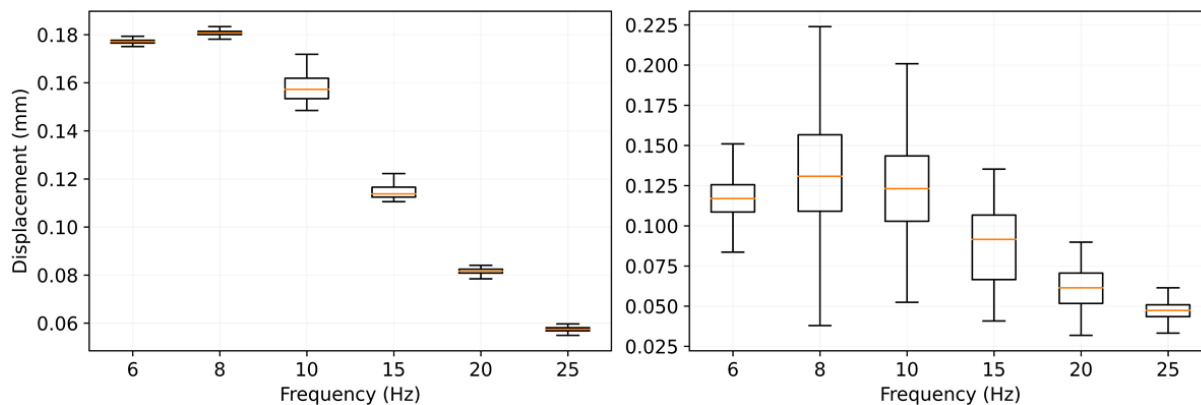
The strain response shows that some non-linearity exists in the strain prototype. The strain response does not return to the original and lowest value after each cycle. The response does eventually stabilise after 25 cycles at the lower bound. The upper bound stabilises faster and stays consistent throughout the test. The signal from the prototype was in close agreement with the applied load. The upper bound or maximum load is of interest when considering wheel loads and wheel flats that can occur on a railway line, thus the lower bound offset is not of importance. The width of each amplitude is wider for the strain prototype compared to the force applied by the MTS. Figure 4.17 shows the response of the strain prototype from a 1 Hz cyclic loading test. A maximum rail seat load of 86 kN was used in the cyclic test.

The small steps in the strain prototype graph are due to the sensitivity of the sensor at the set resolution. The sensitivity of the ADC used to measure the strain gauge output is 0.25 mV/digit at the resolution of 14 bits.
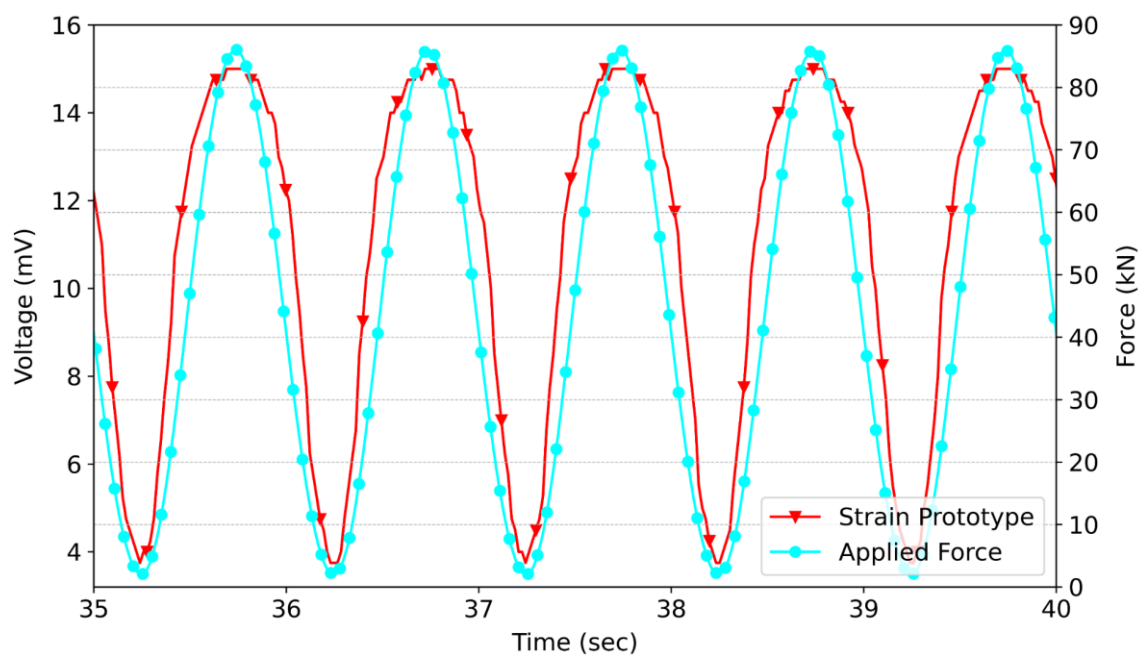
**Figure 4.17: Strain prototype response from a 1 Hz cyclic loading**

## 4.4 SMART RAIL PAD

### 4.4.1 Initial laboratory testing

The initial testing was done before the field experiment to test whether the entire system was working as intended. The same experimental setup as both prototypes was used. Short cyclic tests were done at 60 kN to prevent any damage before the field experiment.

### 4.4.2 Identification of wheel defects in the field

The two identical PETG smart rail pads were installed on opposite ends of the same sleeper at the Bloubank test site. The grey pad was installed on the left rail and the black pad on the right rail (as per increasing kilometre direction). Two LVDTs for each smart pad were installed as control measurement for the rail pad deflection and wheel defect detection. The acceleration data from the smart rail pad was integrated twice, using the trapezoidal rule with a 1 Hz high pass Butterworth filter, for displacement. Thereafter, a mean filter with a window size of three, was used to remove the trend/drift that occurs when double integrating acceleration to displacement. Due to the low sampling rate of 40 Hz, no filtering of the data was required for the removal of any high frequencies.

The wheel defects, which were identified by the LVDT data, was used as a control to compare whether the smart pad was able to successfully identify the same defects. The position and the magnitude of the wheel defects, between the LVDTs and the smart pads, were compared. This

was done to ascertain the success factor to which the smart rail pads identified any wheel defects. The accelerometers and the strain gauge were used to detect any wheel defects. The smart rail pads missed some wheel defects where it did not create a large enough displacement or event to classify it as a wheel defect when compared to the LVDT displacement. This was due to the limitation of the 40 Hz sample rate and the 3D loading of the wheel on the rail. The smart rail pads also had false readings of wheel defects where other external elements such as rolling stock movement and a wide range of excited external frequencies created large displacement readings for the smart rail pads and not for the LVDTs.

The average displacement of each train was used as an indication to distinguish between a normal wheel and a defective wheel. The defective wheels were taken as any displacement above 0.5 mm, whereas any displacement below that was classified as normal. A wheel defect was only successfully identified when it had a distinct peak and/or shape or a big disturbance/event in the accelerometer displacement data and was above 0.5 mm. The accelerations from the smart rail pads had positive and negative symbols indicating the direction of movement. The symbols stay when double integrating the acceleration to displacement. However, the symbols in front of the displacement did not play a role in identifying the defects, as a distinct peak or shape can be seen in both the positive and negative direction. Some of the peak displacements from the LVDTs were under- or overestimated by the accelerometers, however, it still had a clear indication that it was a wheel defect. Figure 4.18 displays the percentage of successfully identified wheel defects for both the smart rail pads.
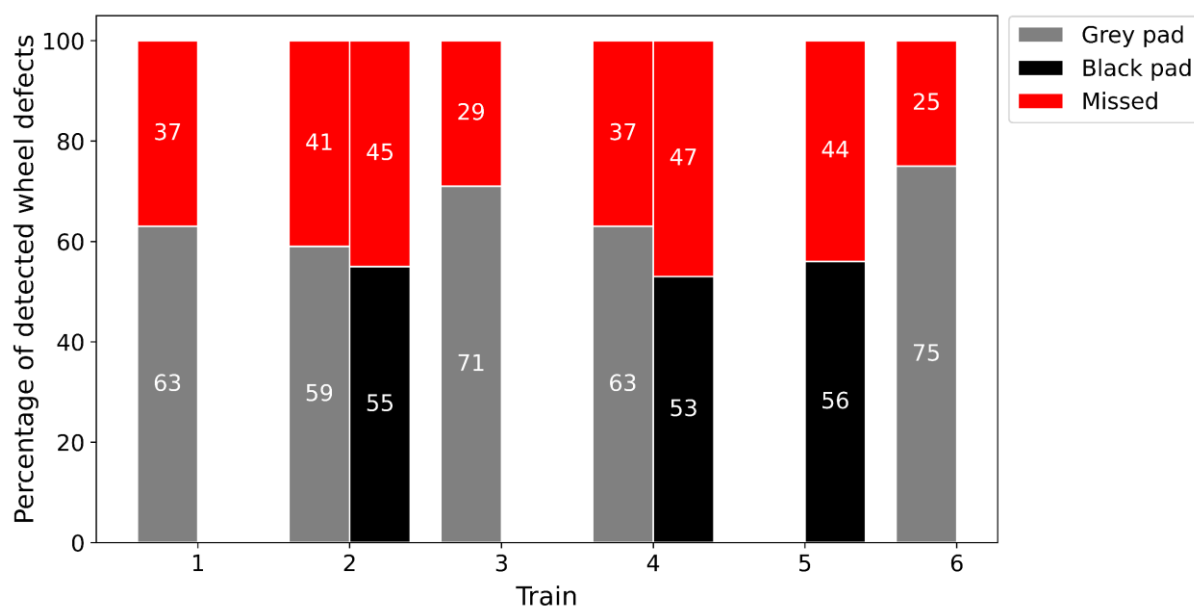


**Figure 4.18: Successfully identified wheel defects from both smart rail pads**

The results were normalised to a percentage of the true wheel defects from the LVDTs that were identified by the smart rail pads. The grey and black bars indicate the successfully identified wheel defects for each smart rail pad and the red bars indicate the missed wheel defects. The number of successfully detected wheel defects were relatively constant across all the trains for the grey smart rail pad. The level of accuracy was not high due to the limiting sampling rate of 40 Hz, the other external frequencies that could influence the readings and the type of loading that the rail pad experienced in the field. All the successfully detected wheel defect percentages, for the grey and black smart rail pads, were above 50 %, proving that wheel defects can be detected to an acceptable extent by using accelerometers and the strain gauge inside the smart rail pad. There was only one instance where the strain gauge was used to detect a wheel defect which was on Train 3 from the grey smart pad, as illustrated in Figure 4.19. The strain gauge clearly shows an irregular shape at the position of the wheel defect.
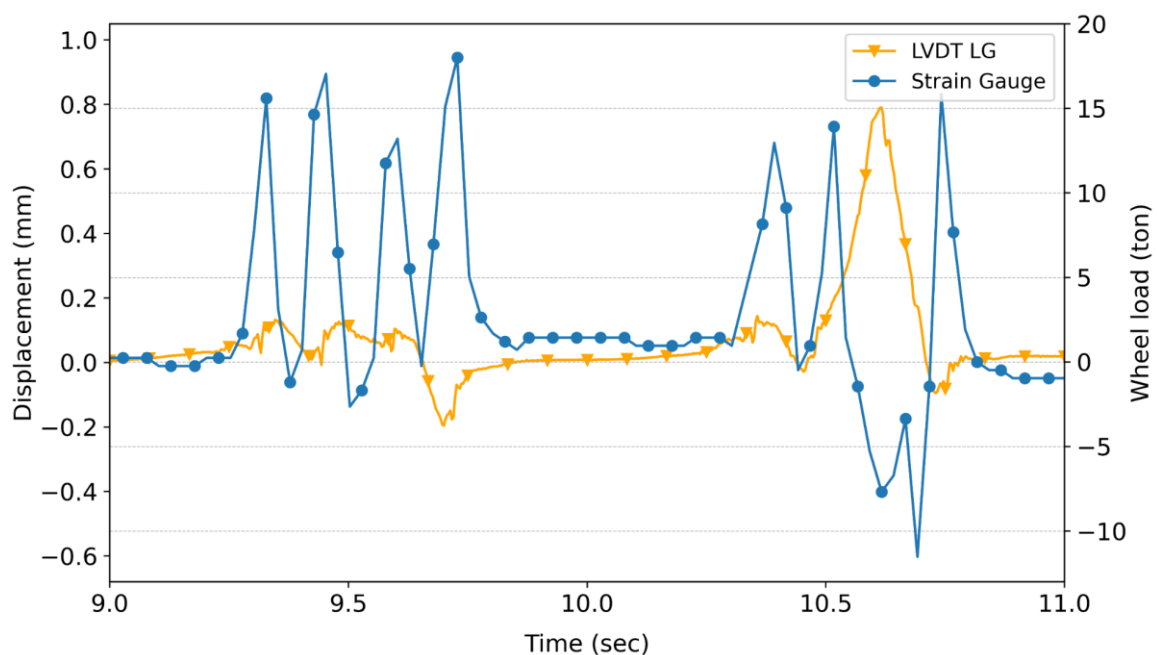


**Figure 4.19: Strain gauge response to wheel defect on Train 3**

### 4.4.3 Load sensing capabilities

The main purpose of the strain gauge was to be used as the load sensing instrument in the smart rail pad. No laboratory calibration was done to determine a calibration factor to convert the mV readings to kN values. The reason for this decision is that it was not possible to replicate the same conditions in the laboratory as in the field. The type of fasteners and the 3D loading from

the wheel in the field influenced the calibration of the strain gauge in the laboratory. The strain gauge in the smart rail pad was calibrated according to the field conditions using the control strain gauges glued to the rail. A calibration factor of 1.98 mV/ton or 0.2 mV/kN with a coefficient of determination ($R^2$) for the linear fit of 0.991 was determined. The calibration was done on the known mass of the locomotives in front of each train. The calibration factor was used to convert the mV signals from the smart rail pad into tons for the approximated wheel load. The calibrated signal response from the grey smart pad, below the left rail, compared with the control strain gauge is illustrated in Figure 4.20. No strain gauge data from the black smart rail pad was obtained due to a cabling problem in the pad.
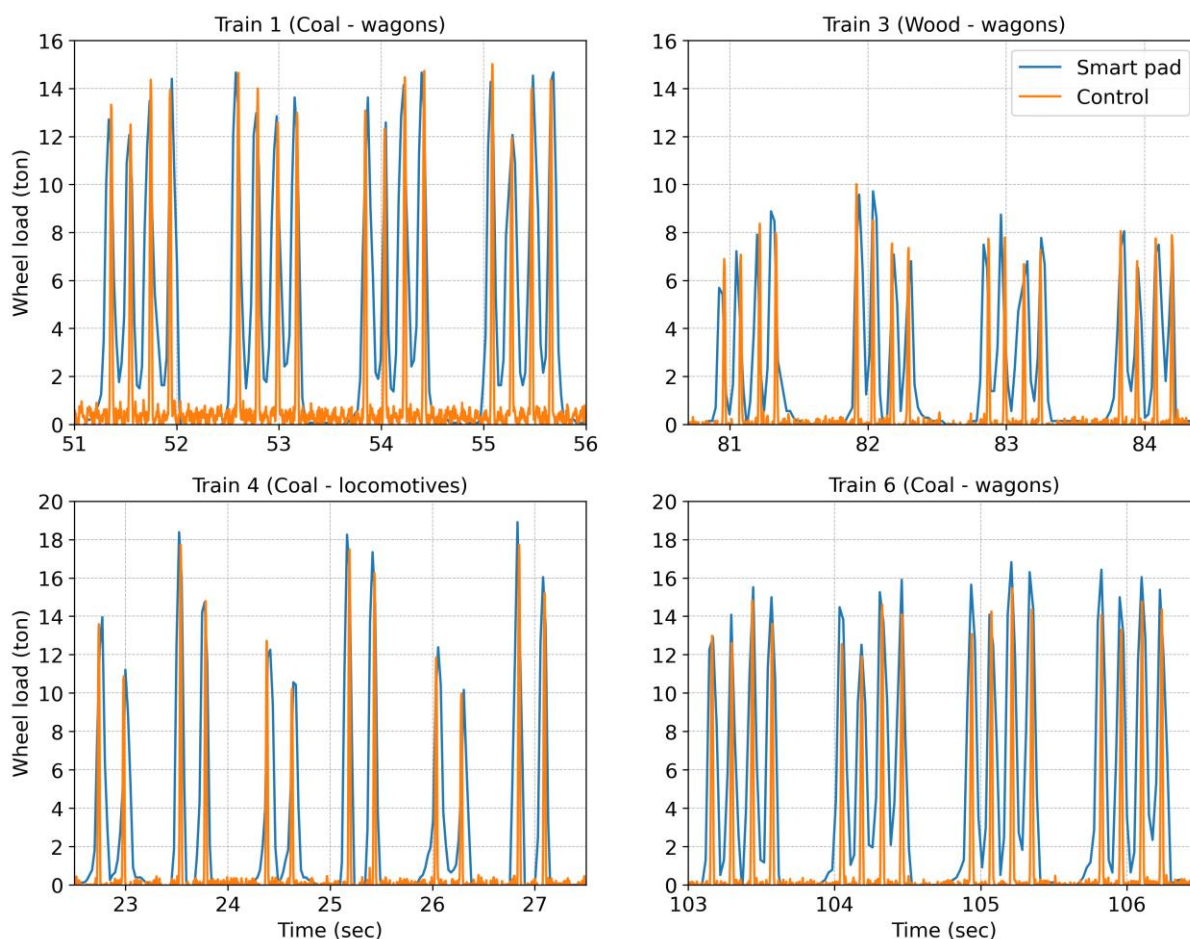


**Figure 4.20: Wheel loads from the smart rail pad for Trains 1, 3, 4 and 6**

The smart rail pad showed excellent signal response to the variation in loading magnitude of the tested trains and could therefore successfully be used to measure the wheel loads. The calibrated wheel loads from the smart rail pad were in close agreement with the true value of the wheel

loads from the control strain gauges, as shown in Figure 4.20. Figure 4.21 displays the mean peak wheel load from the smart rail pad and the control strain gauge measurements with standard deviation bars. It illustrates that the smart rail pad was able to accurately measure the wheel loads. The standard deviation is relatively close between the smart rail pad and the control, across all the trains, except for Train 3 containing the lower wheel loads. The smart rail pad can also be used as an axle counter because of the clear differentiation between the axles of the trains.
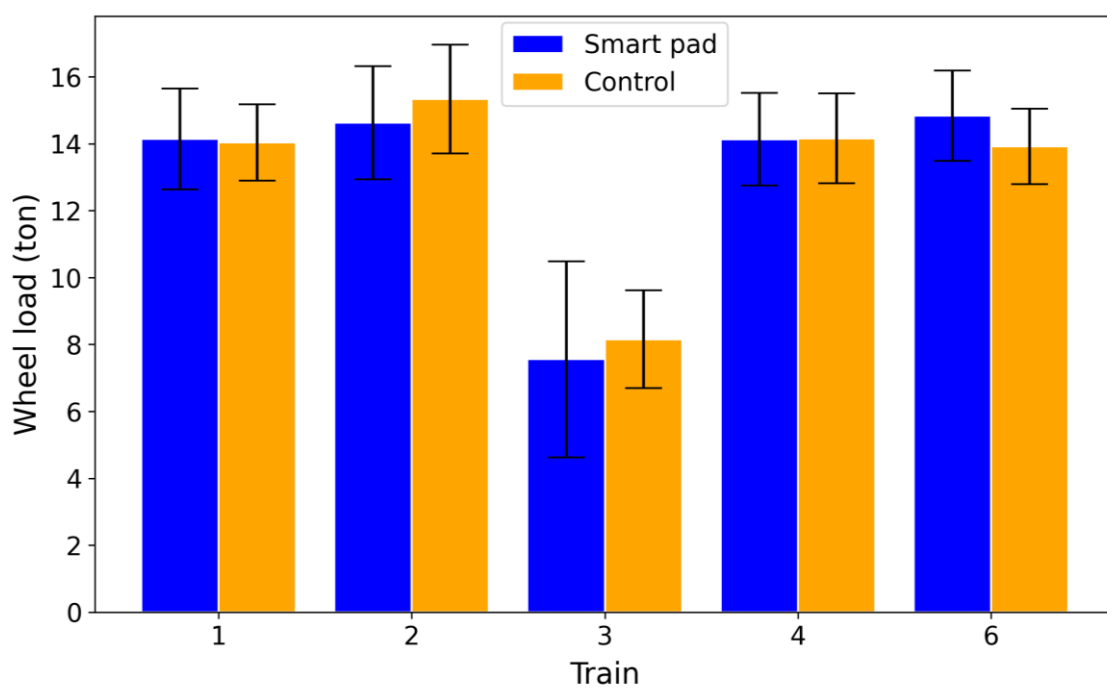


**Figure 4.21: Mean peak wheel load of the smart rail pad and the control strain gauge measurements**

Figure 4.22 displays the percentage error of the smart rail pad wheel load measurements. Train 3, transporting timber logs, had the lowest wheel loads and possibly also the highest variation in wheel load and subsequently exhibited the highest measurement error.
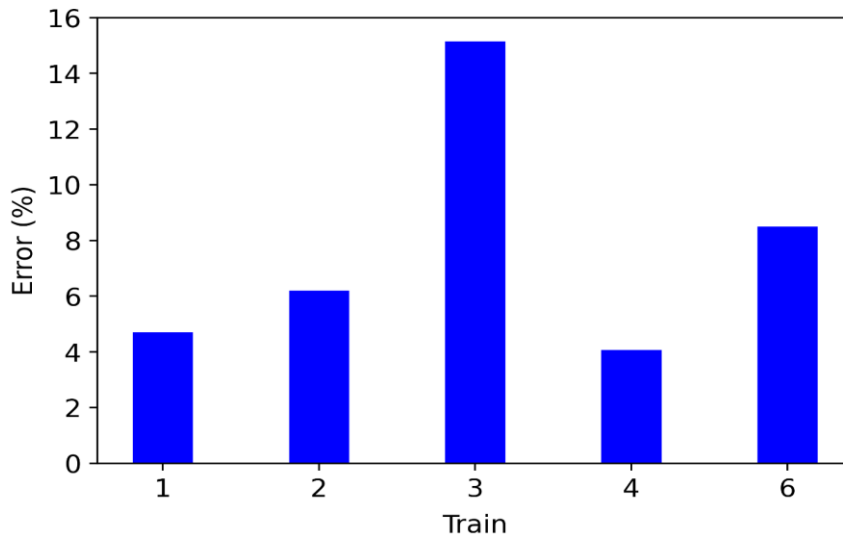
**Figure 4.22: Percentage error for the smart rail pad**

### 4.4.4 Comparison between the smart rail pad and the HDPE pad (field test)

A comparison of the pad deflection between the smart rail pad and an HDPE pad, installed in the field, was done by installing an LVDT to the sleeper next to the test sleeper. This was done to determine whether the smart rail pad could operate as a normal rail pad under service conditions. Figure 4.23 displays the LVDT mean peak displacement (or deflection) of the smart rail pad and the HDPE pad.
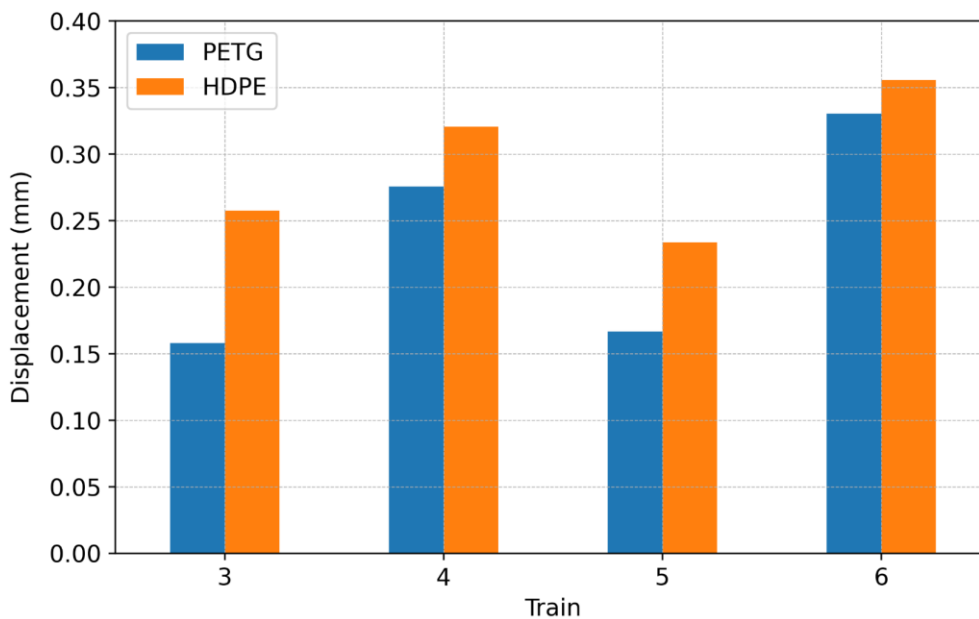


**Figure 4.23: LVDT Mean Peak displacement (Smart Rail Pad versus HDPE)**

The mean peak displacement of the smart rail pad was less than that of the HDPE rail pad for all four trains. This could have been due to the condition of the HDPE rail pad and it being softer and closer to the end of its service life.

The maximum LVDT peak displacements of the smart rail pad and the HDPE pad are shown in Figure 4.24. The maximum peak displacements of the two pads are almost identical and exactly the same for Train 4. This proves that the smart rail pad deforms and reacts in a similar way compared to the HDPE rail pad. The smart rail pad can be used in place of a real rail pad and will not jeopardise the track structure. The magnitude of the displacement for Trains 3 and 5 clearly show that a major wheel defect occurred with a maximum displacement greater than 1 mm.
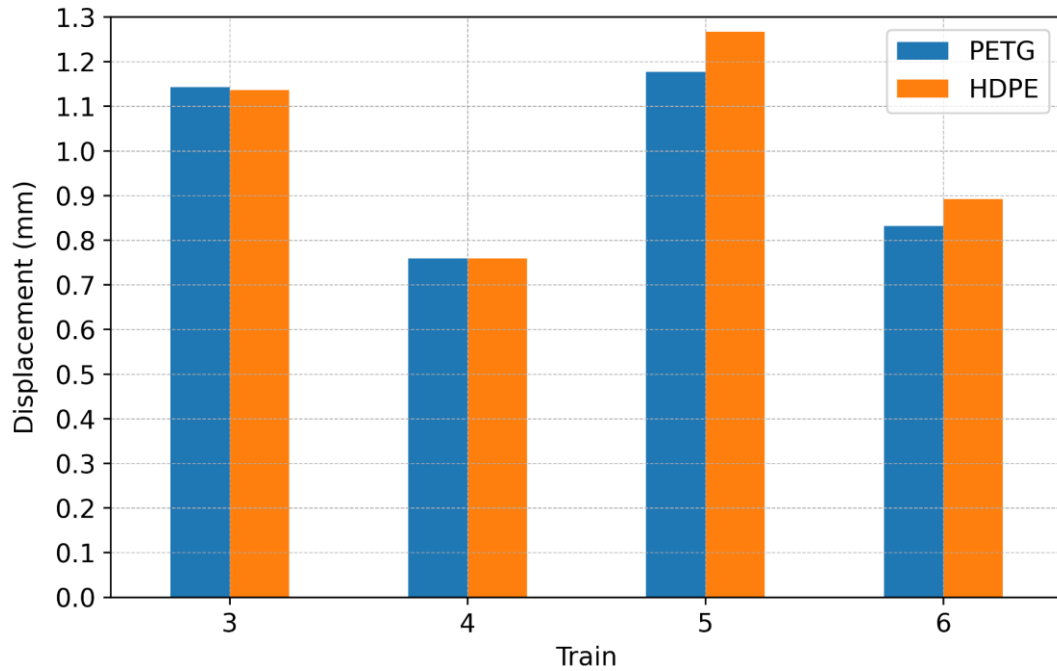


**Figure 4.24: LVDT Maximum Peak Displacement (Smart Rail Pad versus HDPE)**

# 5 CONCLUSIONS AND RECOMMENDATIONS

This chapter provides a summary of the results from the experimental work performed including the conclusions for each of the objectives outlined in Chapter 1. Recommendations based on the conclusions as well as recommendations for further research are provided.

## 5.1 CONCLUSIONS

### 5.1.1 3D Printing Material Testing

The following conclusions can be made about the material testing of 3D printing filament:

- The average tensile strength and elastic modulus of PLA (100%) were 31.3 MPa and 5.2 GPa which is similar to those found by other researchers. Similarly, the tensile strength of PETG and TPU were in good agreement with recent research on identical materials.
- The stress-strain behaviour of the PLA, PETG and TPU printing filament was as expected for rigid and non-rigid plastics.
- The compression elastic modulus of PLA and PETG was less than the tensile elastic modulus due to the different specimen shapes and rate of loading in the tests.

The following conclusions can be made with regard to investigating the effectiveness of 3D printing material as a rail pad:

- The static stiffness of the pads typically increased with each test. The three 3D printed rail pads had stiffnesses falling in a range bounded by the HDPE (higher bound) and the Hytrel (lower bound) pad stiffnesses. PETG had a stiffness in the middle of the range of the five tested pads and showed good consistency in its static stiffness.
- No signs of hysteresis when loading and unloading were present for PLA and PETG whereas TPU showed a reasonable amount of hysteresis and permanent deformation.
- The dynamic stiffness increased as the cycles increased. The 3D printed rail pads stiffened and hardened to an extent, as more loads were applied onto it. As before, the three 3D printed rail pad dynamic stiffnesses were bounded by the HDPE and the Hytrel stiffnesses.
- PETG was chosen as the best-suited material for fabricating a smart rail pad to protect instrumentation inside while still providing some elasticity to the track structure. Even though PLA was the strongest 3D printing material, it is more brittle than PETG and it can become soft when left in the sun, which is a concern for field testing.

I The PETG rail pad had smaller deflections than the HDPE rail pad in the field. This could be due to the condition and age of the HDPE rail pad. The maximum displacement of the PETG and HDPE pads were almost identical, confirming that the smart rail pad deformed and functioned in a similar way as the HDPE rail pad.

### 5.1.2 Prototype testing

The following conclusions can be made about the development of the smart rail pad using sensing technology, embedded inside a 3D printed rail pad:

I The accelerometer prototype showed poor results for frequencies below 2 Hz due to a performance limitation of the sensor, however, demonstrated good results for frequencies above 6 Hz. The pad deflection derived from the measured acceleration, underestimated the actual pad deflection across all frequencies from 6 – 25 Hz. The mean difference between the accelerometer and the LVDT deflections decreased as the frequency increased. This means that the MEMS accelerometer is more accurate with higher frequency signals.

I The maximum displacements measured by the accelerometer and the LVDT were reasonably close with small differences were noted at higher frequencies.

I The strain prototype showed good correlation between the output signal and the applied load, however, the pad exhibited an offset for the lower bound of the cyclic loading.

### 5.1.3 Smart rail pad

The following conclusions can be made with regard to the quantification of the dynamic response of a smart rail pad in both laboratory and field conditions:

I The smart rail pad was able to detect more than 60 % of the wheel defects on average as measured on an operational railway line. This is as accurate as expected because of the major limiting factor of the low sampling rate of the system when all three instruments are logging data. The strain gauge could also be used to detect wheel defects apart from the accelerometers.

I The smart rail pad showed excellent signal response to the variations in the loading of the tested trains and can be used to measure the corresponding wheel loads. The measured wheel loads were in close agreement with the control wheel loads. The smart rail pad can be used for load sensing of wheel loads and as an axle counter.

I The smart rail pad can measure the condition of the train wheels to an acceptable degree by measuring accelerations and displacements to detect wheel defects. The smart rail pad can be used to estimate the wheel loads of those train wheels. The whole system

can log the smart rail pad data automatically by detecting an oncoming train and switching the microcontroller into logging mode.

## 5.2 RECOMMENDATIONS

The following recommendations are made for further research:

- Further investigation into different ways to make the smart rail pad such as using an existing rail pad or fabricating one from existing rail pad materials;

- Investigation of the calibration of the smart rail pad on a test track to replicate field conditions;

- Further investigation into the updated version of the Razor microcontroller to increase the sampling rate of the system;

- Investigation of different instrumentation such as piezo-electric and piezo-resistive sensors;

- Further investigation into making enough smart rail pads to test along 5 sleepers to capture the whole circumference of the train wheel;

- Investigation into quantifying or measuring rail rotation from the acceleration data obtained from a smart rail pad; and

- Further investigation into long term behaviour and permanent deformation of the 3D printed rail pad and how that will influence measurements.

# 6    REFERENCES

Abdukarimov, N. (2019). *Easy DAQ System Development with Arduino® and Tri-Axis Accelerometer – Model ADXL335*. PhD Thesis. Turin Polytechnic University in Tashkent.

Adafruit LIS331 High-g 3-Axis Accelerometer. (2020). Adafruit Industries, viewed 10/05/2021, <https://learn.adafruit.com/adafruit-h3lis331-and-lis331hh-high-g-3-axis-accelerometers/overview>.

Alemi, A., Corman, F. and Lodewijks, G. (2017). Condition monitoring approaches for the detection of railway wheel defects. *Journal of Rail and Rapid Transit*, Vol. 231, No. 8, pp 961-981.

Analog Devices. (1993). *ADXL50 – monolithic accelerometer with signal conditioning*. Data sheet, Analog Devices, Norwood, MA.

Analog Devices. (2009). *ADXL335 – small, low-power, 3-axis ±3 g accelerometer*. Data sheet, Analog Devices, Norwood, MA.

ARUP. (2019). ARUP, viewed 23/06/21, <https://www.arup.com/perspectives/publications/research/section/future-of-rail-2050>.

ASTM Standard D638. (2014). *Standard Test Method for Tensile Properties of Plastics*. ASTM International, West Conshohocken, PA, 2014, DOI: 10.1520/D0638-14, <www.astm.org>.

ASTM Standard D695. (2015). *Standard Test Method for Compressive Properties of Rigid Plastics*. ASTM International, West Conshohocken, PA, 2015, DOI: 10.1520/D0695-15, <www.astm.org>.

ASTM Standard D412, 2016 (2021). *Standard Test Methods for Vulcanized Rubber and Thermoplastic Elastomers—Tension*. ASTM International, West Conshohocken, PA, 2021, DOI: 10.1520/D0412-16R21, <www.astm.org>.

Aursudkij, B., McDowell, G.R. and Collop, A. (2009). Cyclic loading of railway ballast under triaxial conditions and in a railway test facility. *Granular Matter*, Vol. 11, No. 6, pp 391-401.

Awoleye, E.O.A. (1993). *Ballast type—ballast life predictions*. Derby, British Rail Research LR CES Vol.122.

Barrett, S.F. (2013). *Arduino Microcontroller Processing for Everyone*. 3rd Edition. Morgan & Claypool Publishers, USA.

Beliveau, A., Spencer, G.T., Thomas, K.A. and Roberson, S.L. (1999). Evaluation of MEMS capacitive accelerometers. *IEEE Design & Test of Computers*, Vol. 16, No. 4, pp 48-56.

Bi, L., Zhao, P., Teng, M., Zhao, L., Liu, X. and Xing, M. (2019). Wayside testing methods for high-frequency vertical wheel-rail impact forces and its applicability. *Measurement*, Vol. 151, No. 1, article no. 107197.

Billauer, E. (2010). Peak Detection in Python. Online: https://gist.github.com/endolith/250860. Accessed 10 October 2021.

Broekman, A. (2018). *Metrology of Mesoscale Ballast Particle Dynamic using KLI-PI*. Master's Dissertation. University of Pretoria.

Cady, F.M. (2009). *Microcontrollers and Microcomputers: Principles of software and hardware engineering*. 2nd Edition. Oxford University Press, New York.

Callister, W.D. and Rethwisch, D.G. (2015). *Materials Science and Engineering*. 9th Edition. John Wiley & Sons, Asia.

Campo, E.A. (2008). *Selection of Polymeric Materials: How to Select Design Properties from Different Standards.* 1st Edition. William Andrew, New York.

Castillo-Mingorance, J.M., Sol-Sánchez, M., Moreno-Navarro, F. and Rubio-Gámez, M.C. (2020). A Critical Review of Sensors for the Continuous Monitoring of Smart and Sustainable Railway Infrastructures. *Sustainability*, Vol. 12, No. 22, article no 9428.

Cerna, M & Harvey, A.F. (2000). National Instruments Application Note 041: The Fundamentals of FFT-Based Signal Analysis and Measurement. Online: <https://www.sjsu.edu/people/burford.furman/docs/me120/FFT_tutorial_NI.pdf> (Accessed 30 September 2021)

Chen, J. and Zhou, Y. (2020). Dynamic vertical displacement for ballastless track-subgrade system under high-speed train moving loads. *Soil Dynamics and Earthquake Engineering*, Vol. 129, February, article no. 105911.

Chiang, Y., Wang, L., Liu, W., Chen, H., Hsu, C. and Yang, C. (2001). Temperature-insensitive linear strain measurement using two fiber Bragg gratings in a power detection scheme. *Optics Communication*, Vol. 197, No. 1, pp 327-330.

Du, C., Dutta, S., Kurup, P., Yu, T. and Wang, X. (2020). A review of railway infrastructure monitoring using fibre optic sensors. *Sensors and Actuators A: Physical*, Vol. 303, March, article no. 111728.

Eisenmann, J. (1972). Germans gain a better understanding of track structure. *Railway Gazette International*, Vol. 128, No. 8, pp 305-308

Esveld, C. (2001). *Modern Railway Track*. 2nd Edition. MRT-Productions, Netherlands.

Evans, B. (2012). *Practical 3D Printers*. 1st Edition. Apress, New York.

Farah, S., Anderson, D.G. and Langer, R. (2016). Physical and mechanical properties of PLA, and their functions in widespread applications — A comprehensive review. *Advanced Drug Delivery Reviews*, Vol. 107, No. 1, pp. 367-392.

Filograno, M.L., Corredera, P., Rodríguez-Plaza, M., Andrés-Alguacil, A. and González-Herráez, M. (2013). Wheel Flat Detection in High-Speed Railway Systems Using Fibre Bragg Gratings. *IEEE Sensors Journal*, Vol. 13, No. 12, December, pp. 4808-4816.

Gräbe, P.J., Clayton, C.R.I. and Shaw, F.J. (2005). Deformation measurement on a heavy haul track formation. In *Proceedings of 8th International Heavy Haul Conference.* International Heavy Haul Association, pp 287-295.

HBM. (2021). *HBM*, viewed 08/06/2021, <https://www.hbm.com/en/3443/xy-t-rosettes-with-measuring-grids-for-analyzing-biaxial-stress/#top>.

Hodgson, G. and Průša, J. (2011). *Prusa Mendel Visual Instructions*. RepRap. Instructions #5. England.

Hoffmann, K. (1989). *An Introduction to Measurements using Strain Gages*. 1st Edition. Hottinger Baldwin Messtechnik GmbH, Darmstadt.

Hong, C., Yuan, Y., Yang, Y., Zhang, Y. and Abro, Z.A. (2019). A simple FBG pressure sensor fabricated using fused deposition modelling process. *Sensors and Actuators A: Physical*, Vol. 285, No. 1, pp 269-274.

Horvath, J. (2014). *Mastering 3D Printing*. 1st Edition. Apress, New York.

Hill, K.O., Fujii, Y., Johnson, D.C. and Kawasaki, B.S. (1978). Photosensitivity in optical waveguides: Application to reflection filter fabrication. *Applied Physics Letters*, Vol. 32, No. 10, pp 647-649.

Hill, K.O. and Meltz, G. (1997). Fiber Bragg Grating Technology Fundamentals and Overview. *Journal of Lightwave Technology*, Vol. 15, No. 8, pp 1263-1276.

Iannacci, J. (2017). *RF-MEMS Technology for High-Performance Passives*. 1st Edition. IOP Publishing, United Kingdom.

Iannace, S., Sorrentino, L. and Di Maio, E. (2014). Biodegradable biomedical foam scaffolds. *Biomedical Foams for Tissue Engineering Applications*. Ed P.A. Netti. 1st Edition. Woodhead Publishing, United Kingdom, pp 163-187.

Imdad, F., Niaz, M.T. and Kim, H.S. (2015). Railway track structural health monitoring system. *15th International Conference on Control, Automation and Systems (ICCAS)*, ICCAS. Busan, South Korea.

International Transport Forum/OECD. (2011). *International Transport Forum*, viewed 22/06/2021, <http://www.internationaltransportforum.org/Pub/pdf/11Outlook.pdf>.

Jideani, T.C.U. (2018*). The Development of Suitable Cyclic Loading and Boundary Conditions for Ballast Box Tests*. Master's Dissertation. University of Pretoria.

Johnson, G.A. & French, J.J. (2018). Evaluation of Infill Effect on Mechanical Properties of Consumer 3D Printing Materials. *Advances in Technology Innovation*, Vol. 3, No. 4, pp 179-184.

Kashyap, R. (1999). *Fiber Bragg Gratings*. 1st ed. Academic Press, London.

Kempe, V. (2011). *Inertial MEMS: Principles and Practice*. 1st Edition. Cambridge University Press, United Kingdom.

Kersey, A.D., Davis, M.A., Patrick, H.J., LeBlanc, M., Koo, K.P., Askins, C.G., Putnam, M.A. and Friebele, E.J. (1997). Fiber Grating Sensors. *Journal of Lightwave Technology*, Vol. 15, No. 8, pp 1442-1463.

Kumagai, N., Ishikawa, H., Haga, K., Kigawa, T. and Nagase, K. (1991). Factors of wheel flats occurrence and preventative measures. *Wear*, Vol. 144, No. 1, pp 277-287.

Kumar, K.S., Soundararajan, R., Shanthosh, G., Saravanakumar, P. and Ratteesh, M. (2020). Augmenting effect of infill density and annealing on mechanical properties of PETG and CFPETG composites fabricated by FDM. *Materials Today: Proceedings*. Article in press https://doi.org/10.1016/j.matpr.2020.10.078

Lee, H., Eom, R. and Lee, Y. (2019). Evaluation of the Mechanical Properties of Porous Thermoplastic Polyurethane Obtained by 3D Printing for Protective Gear. *Advances in Materials Science and Engineering*, Vol. 2019, article ID 5838361.

Leis, J.W. (2011). *Digital Signal Processing Using MATLAB for Students and Researchers.* 1st Edition. Wiley, New Jersey.

Lemkin, M. and Boser, B.E. (1999). A Three-Axis Micromachined Accelerometer with a CMOS Position-Sense Interface and Digital Offset-Trim Electronics. *IEEE Journal of Solid-state Circuits*, Vol. 34, No. 4, pp 456-468.

Li, D., Hyslip, J., Sussmann, T. and Chrismer, S. (2015). Railway Geotechnics. 1st ed. CRC Press, Florida, United States.

López-Higuera, J.M. (2002). *Handbook of Optical Fibre Sensing Technology*. 1st Edition. John Wiley & Sons, England.

Mărieş, G.R.E., Bandur, G. and Rusu, G. (2008). Influence of Processing Temperature on Some Mechanical-Physical Properties of Thermoplastic Polyurethane Desmopan KA 8377 Used for Injection Moulding of Performance Sport Products. *Chem. Bull. "Politechica" Univ. (Timişoara)*, Vol. 53, No. 67, pp 131–134.

Meltz, G., Morey, W.W. and Glenn, W.H. (1989). Formation of Bragg gratings in optical fibers by a transverse holographic method. *Optical Letters*, Vol. 14, No. 15, pp 823-825.

Micro Robotics. (2021). *Micro Robotics*, viewed 03/05/2021, <https://www.robotics.org.za/GY-61?search=accelerometer>.

Milne, D., Le Pen, L., Watson, G., Thompson, D., Powrie, W., Hayward, M. and Morley, S. (2016). Proving MEMS Technologies for Smarter Railway Infrastructure. *Procedia Engineering*, Vol. 143, No. 1, pp 1077-1084.

Nathanson, H.C. and Wickstrom, R.A. (1965). A Resonant-Gate Silicon Surface Transistor with High-Q Bandpass Properties. *Applied Physics Letters*, Vol. 7, No. 4, pp 84.

Newton, S.G. and Clark, R.A. (1979). An investigation into the dynamic effects on the track of wheelflats on railway vehicles. *Journal Mechanical Engineering Science*, Vol. 21, No. 4, pp. 287-297.

Ohtani, T. (1995). Development of a wheel-flat detection system. In *Proceedings of the 11th International Wheelset Conference*, Paris, France, 18 – 22 June.

Priest, J.A., Powrie, W., Yang, L., Gräbe, P.J. and Clayton, C.R.I. (2010). Measurements of transient ground movements below a ballasted railway line. *Géotechnique*, Vol. 60, No. 9, pp 667-677.

Profillidis, V. A. (2000). *Railway Engineering*. 2nd Edition. Ashgate Publishing Limited, United Kingdom.

Ramakrishnan, M., Rajan, G., Semenova, Y. and Farrell, G. (2016). Overview of Fiber Optic Sensor Technologies for Strain/Temperature Sensing Applications in Composite Materials. *Sensors*, Vol. 16, No. 1, article no. 99.

Rhodes, D., Leeves, G.G. and Cox, S.J. (1989). Rail Pads for Concrete Sleepers in Heavy Haul Track. In *Proceedings of 4th International Heavy Haul Conference*. International Heavy Haul Association (IHHA). Brisbane.

Russel, E.J., Rose, J.G. and Clarke, D.B. (2020). In-Track Timber Crosstie-Ballast Interfacial Pressure Measurements for Revenue Freight Trains and DOTX 218/219 Test Train Operating Conditions. In *Proceedings of Railway Roadbed & Ballast Symposium*. RRB. pp 135-155.

Sahota, J.K., Gupta, N. and Dhawan, D. (2020). Fiber Bragg grating sensors for monitoring of physical parameters: a comprehensive review. *Optical Engineering*, Vol. 59, No. 6, article no. 060901.

Sainz-Aja, J.A., Carrascal, I.A., Ferreño, D., Pombo, J., Casado, J.A. and Diego, S. (2020). Influence of the operational conditions on static and dynamic stiffness of rail pads. *Mechanics and Materials*, Vol. 148, September, article no. 103505.

Sañudo, R., Markine, V. and Pombo, J. (2017). Study on different solutions to reduce the dynamic impacts in transition zones for high-speed rail. *Journal of Theoretical and Applied Vibration and Acoustics*, Vol. 3, No. 2, pp. 199-222.

Selig, E.T. and Waters, J.M. (1994). *Track geotechnology and substructure management*. 1st Edition. Thomas Telford, London.

Sensorline - Fiber Optic Rail Traffic Sensors. (2009). *Sensorline*, viewed 05/01/2021, <https://www.sensorline.de>.

Sol-Sánchez, M., Castillo-Mingorance, J.M., Moreno-Navarro, F., Mattinzioli, T. and Rubio-Gámez, M.C. (2021). Piezoelectric-sensored sustainable pads for smart railway traffic and track

state monitoring: Full-scale laboratory tests. *Construction and Building Materials*, Vol. 301, No. 1, article no. 124324.

Sol-Sánchez, M., Castillo-Mingorance, J.M., Moreno-Navarro, F. and Rubio-Gámez, M.C. (2021). Smart rail pads for the continuous monitoring of sensored railway tracks: Sensors analysis. *Automation in Construction*, Vol. 132, No. 1, article no. 103950.

SparkFun – Razor 9DoF IMU Hookup Guide. (2016). *SparkFun Electronics*, viewed 02/05/2021, <https://learn.sparkfun.com/tutorials/9dof-razor-imu-m0-hookup-guide>.

Srinivasan, R., Prathap, P., Raj, A., Kannan, S.A. and Deepak, V. (2020). Influence of fused deposition modelling process parameters on the mechanical properties of PETG parts. *Materials Today: Proceedings*, Vol. 27, No. 1, pp 1877-1883.

Stenström, C., Lindqvist, J. and Andersson, F. (2019). Condition based maintenance using MEMS accelerometers: For faster development of IoT in railways. In *Proceedings of the International Heavy Haul Association (IHHA) STS Conference.* International Heavy Haul Association (IHHA). Norway.

Tekscan (2019). *FlexiForce Sensor Manual*. Tekscan, South Boston, USA.

Thompson, D. (2009). *Railway Noise and Vibrations: Mechanisms, Modelling and means of control*. 1st Edition. Elsevier, United Kingdom.

Titterton, D. and Weston, J. (2004). *Strapdown Inertial Navigation Technology*. 2nd Edition. The Institution of Electrical Engineers, United Kingdom.

Van Niekerk, J.O. (2021). *Ballast Lateral Confinement Through Rigid Polyurethane Foam Shoulder Reinforcement*. Master's Thesis. University of Pretoria.

Wang, J., Yang, B., Lin, X., Gao, L., Liu, T., Lu, Y. and Wang, R. (2020). Research of TPU Materials for 3D Printing Aiming at Non-Pneumatic Tires by FDM Method. *Polymers*, Vol. 12, No. 1, article no. 2492.

Wheatstone, C. (1843). *An Account of several new Instruments and Processes for determining the Constants of a Voltaic Circuit*. Philosophical Transactions of the Royal Society of London, Vol. 4, pp 469-471.

Woschitz, H. (2011). Development of a rail-strain-pad using FBG sensors. *5th International Conference on Structural Health Monitoring of Intelligent Infrastructure (SHMII-5).* Cancun, Mexico, Sunday 11th to Thursday 15th December 2011.

Zhang, S.L., Koh, C.G. and Kuang, K.S.C. (2014). Fibre Optic Rail Pad Sensor Based Wheel Flat Identification. *In Proceedings of the Second International Conference on Railway Technology: Research, Development and Maintenance*. Civil-Comp Press, Stirlingshire, UK, Paper 168.

Zhang, S.L., Koh, C.G. and Kuang, K.S.C. (2018). Proposed rail pad sensor for wheel-rail contact force monitoring. *Smart Materials and Structures,* Vol. 27, No. 11, article no. 115041.

Zhou, C., Gao, L., Xiao, H. and Hou, B. (2020). Railway Wheel Flat Recognition and Precise Positioning Method Based on Multisensor Arrays. *Applied Sciences*, Vol. 10, No. 1, article no. 1297.

3Dnatives. (2021). *3Dnatives*, viewed 07/01/2021, <https://www.3dnatives.com/en/plastics-used3d-
printing110420174/#:~:text=ABS,commonly%20used%203D%20printing%20plastics>.

# APPENDIX A

# ADXL335 ACCELEROMETER

## A.1 INTRODUCTION

The ADXL335 accelerometer measures accelerations in three orthogonal axes referred to as X, Y and Z direction. The ADXL335 accelerometer can measure acceleration with a minimum range of $\pm 3$ g in each axis. The accelerometer has a sample rate range of 0.5 – 1600 Hz in the X and Y direction while the Z axis has a sample rate range of 0.5 – 550 Hz. However, the user must select the sample rate of the accelerometer with the aid of $C_X$, $C_Y$ and $C_Z$ capacitors at the $X_{OUT}$, $Y_{OUT}$ and $Z_{OUT}$ pins on the accelerometer. The capacitors were added to implement low-pass filtering of 50 Hz for noise reduction of any high-frequencies (Analog Devices, 2009). The functional block diagram of the accelerometer is displayed in Figure A.1.
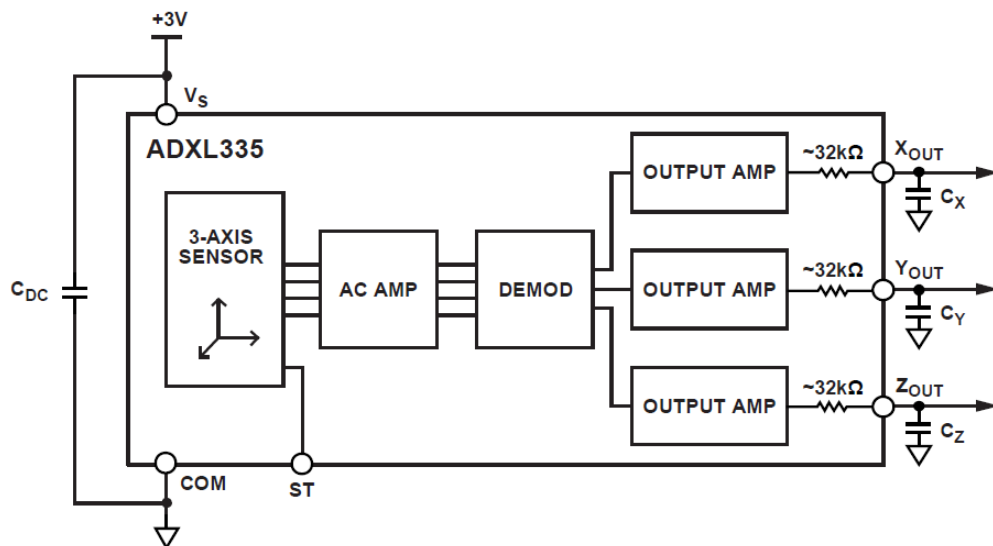


**Figure A.1: Functional block diagram of ADXL335 accelerometer (Analog Devices, 2009)**

## A.2 CALIBRATION

The calibration process starts with the wiring connections of the accelerometer to an Arduino Uno. The voltage out from the accelerometer is connected to the 3.3 volt pin on the Arduino. X, Y and Z outputs are wired to the analog pins A0, A1 and A2 on the Arduino. The wiring of the accelerometer is displayed in Figure A.2.
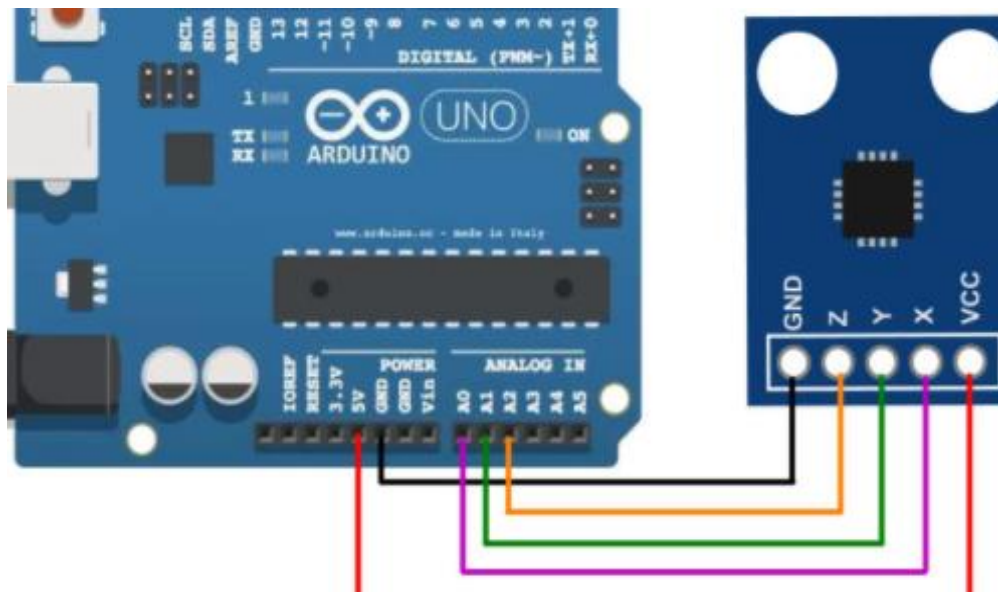
**Figure A.2: Wiring ADXL335 to Arduino Uno (Micro Robotics, 2021)**

The following code is used to determine the minimum and maximum output values for each axis from the accelerometer. The Arduino board has a 10-bit ADC, which will map the output voltages between 0 and 3.3 V into integers between 0 and 1023. Figure A.3 shows the calibration method used to level the accelerometer for each direction to determine the minimum and maximum range. An example of the output from the serial monitor is displayed in Figure A.4.

```cpp
const int xpin = A0;                  // x-axis of the
accelerometer
const int ypin = A1;             // y-axis
const int zpin = A2;             // z-axis

void setup() {
    // initialize the serial communications:
    Serial.begin(9600);
}

void loop() {
            // print the sensor values:
    Serial.print("X, Y, Z :: ");
    Serial.print(analogRead(xpin));
            // print a tab between values:
    Serial.print(",");
    Serial.print(analogRead(ypin));
            // print a tab between values:
    Serial.print(",");
    Serial.print(analogRead(zpin));
    Serial.println();
```

```
                    // delay before next reading:
        delay(100);
}
```
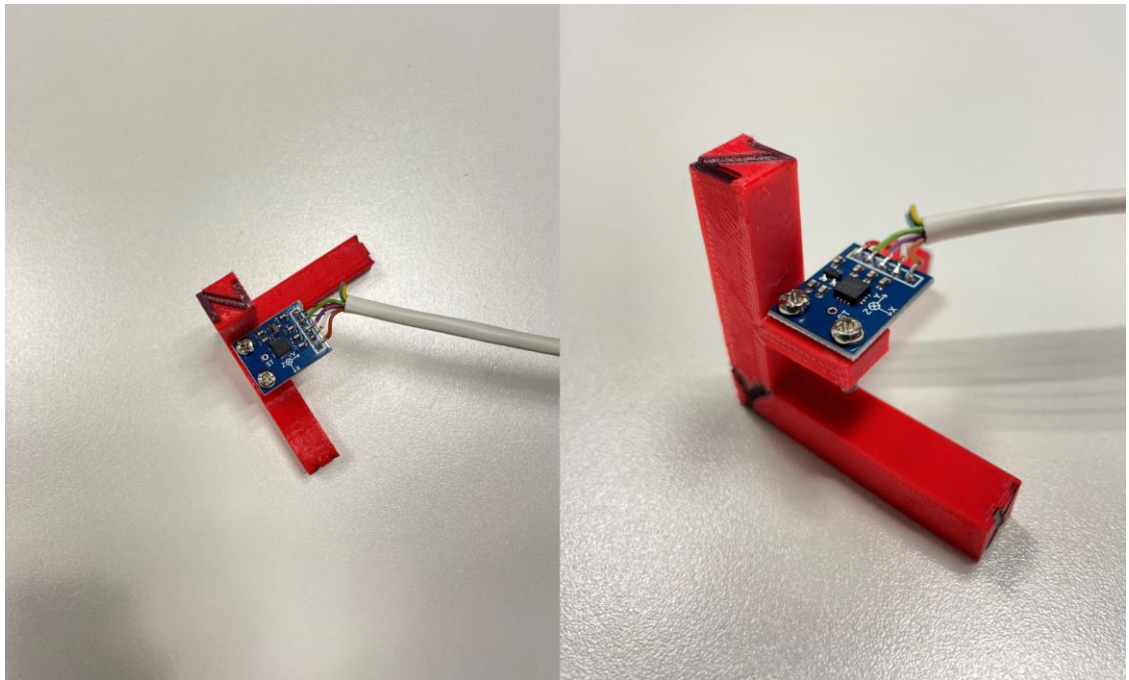


**Figure A.3: Calibration process for each axis using a 3D printed 3-axis structure**
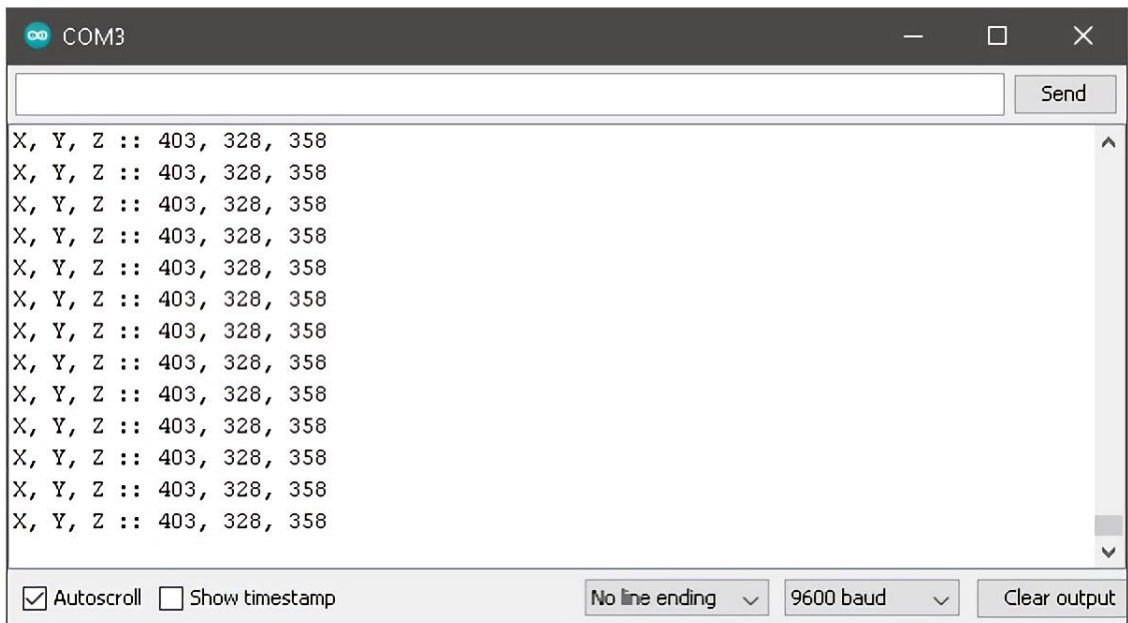


**Figure A.4: The serial monitor displaying the minimum and maximum output values for each axis with the x-axis pointing perpendicular to gravity**

The average of the minimum and maximum values for each axis and direction are given in Table A.1. These values are the minimum and maximum values for the range of -1

g to +1 g. In Figure A.4, the maximum value for +1 g in the X direction is given where the Y and Z direction are displaying the value for 0 g. The minimum and maximum values used to map the extreme analog values for better understanding of the output from the ADC.

**Table A.1: Average minimum and maximum values**

|       | X   | Y   | Z   |
|-------|-----|-----|-----|
| −1 g  | 268 | 262 | 293 |
| +1 g  | 403 | 396 | 425 |

The first mentioned code is used to determine the range of minimum and maximum values. The following code replaces the previously mentioned code. The following code utilises the minimum and maximum values to map the sensor voltages between - 1 g and +1 g for calibration purposes. The output from the serial monitor for calibration of the Z - axis in the positive direction is given in Figure A.5.

```
int xpin = A0;
int ypin = A1;
int zpin = A2;
int xvalue;
int yvalue;
int zvalue;
String Data;

void setup()
{
    Serial.begin(9600);    // initialize the serial
    communications:
}


void loop()
{
    xvalue = analogRead(xpin);
    //reads values from x-pin & measures acceleration in X
    direction
    int x = map(xvalue, 268, 403, -100, 100);
    //maps the extreme ends analog values from -100 to 100
    for our understanding
    float xg = ((float)x/(100.00))*9.81;
    //converts the mapped value into acceleration in terms of
    "m/s^2"
```

```
        Serial.print(xg); //prints value of acceleration in X
        direction
        Serial.print(" m/s^2   ");        //prints "m/s^2"

        yvalue = analogRead(ypin);
        int y = map(yvalue, 262, 396, -100, 100);
        float yg = ((float)y/(100.00))*9.81;
        Serial.print("\t");
        Serial.print(yg);
        Serial.print(" m/s^2   ");

        zvalue = analogRead(zpin);
        int z = map(zvalue, 293, 425, -100, 100);
        float zg = ((float)z/(100.00))*9.81;
        Serial.print("\t");
        Serial.print(zg);
        Serial.println(" m/s^2   ");
        delay(100);
{
```
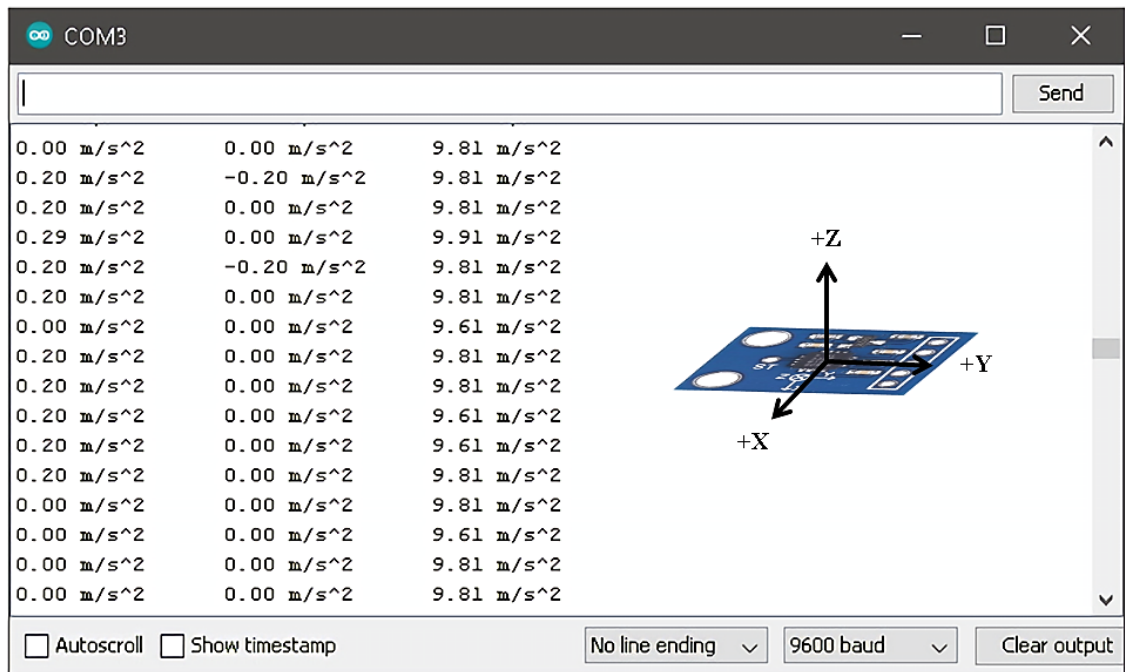


**Figure A.5: Calibration of Z - axis in the positive direction**

From Figure A.5, the Z - axis displays the positive force of 1 g or 9.81 m/s$^2$ for gravitational acceleration in the displayed orientation of the accelerometer. The positive orientation of each axis of the accelerometer is displayed in Figure A.5.